ADDITIVELY MANUFACTURED NANOCOMPOSITE SENSORS WITH LOW-DIMENSIONAL NANOFILLERS FOR MULTIPHYSICS SENSING: FROM STRUCTURAL BATTERY STATUS EVALUATION TO HEALTH MONITORING OF COMPOSITES

QINGQING WANG

PhD

The Hong Kong Polytechnic University

2026

The Hong Kong Polytechnic University

Department of Mechanical Engineering

Additively Manufactured Nanocomposite Sensors with Low-dimensional Nanofillers for Multiphysics Sensing: from structural battery status evaluation to health monitoring of composites

Qingqing Wang

A thesis submitted in partial fulfillment of the requirements

for the degree of Doctor of Philosophy

October 2025

CERTIFICATE OF ORIGINALITY

I hereby declare that this thesis is my own work and that, to the best of my knowledge and belief, it reproduces no material previously published or written, nor material that has been accepted for the award of any other degree or diploma, except where due acknowledgment has been made in the text.

_____ (Signed)

Qingqing WANG (Name of student)

ABSTRACT

The rapid development of next-generation energy systems, wearable electronics, and lightweight multifunctional composites is driving the need for intriguing sensing technologies that can operate reliably across a broad spectrum of mechanical and acoustic environments. Conventional sensors such as strain gauge, lead zirconate titanate (PZT) wafers, or brittle fibre Bragg grating (FBG), while they are effective in specific regimes, often suffer from limitations such as high rigidity, poor compatibility with host structures, or constraints on frequency bandwidth, being confined to a narrow range. In particular, scalable, flexible, and broadband sensing solutions remain underexplored, despite their critical importance for applications spanning from personalized healthcare to structural health monitoring (SHM).

In this PhD research project, a new class of nanocomposite sensors based on low-dimensional conductive fillers is developed and validated, demonstrating its capability of offering broadband sensing spanning from quasi-static strain gauging, through acoustic vibration measurement, to ultrasonic guided wave acquisition. The performance of the developed sensors is systematically evaluated across multiphysics scenarios: monitoring charge–discharge-induced strain evolution and external impacts in structural batteries, detecting acoustic signals for wearable healthcare applications such as speech recognition, and enabling ultrasonic guided wave–based SHM in fiber-reinforced polymers (FRP) composites. Additive manufacturing-driven fabrication

strategy progresses in a stepwise manner, beginning with standalone sensors produced via aerosol jet printing (AJP), advancing to hybrid systems that combine fused deposition modeling (FDM) with AJP to embed sensors within carbon fiber–reinforced polymer (CFRP) laminates, and culminating in totally additively manufactured multifunctional composites with inherent self-sensing capabilities.

To start with, an implantable graphene–polyvinyl alcohol (PVA)-coated glass fiber sensor is first developed and integrated into structural batteries using dip-coating where it achieves ultra-low strain detection limits of 0.009% in tension and stable durability over 2000 cycles. Beyond capturing charge–discharge-induced deformations, the sensor provides rapid detection of external impacts, enabling early warnings against thermal runaway and mechanical damage. This establishes the feasibility of embedding sensitive nanocomposite sensors within structural energy storage systems for real-time monitoring under both electrochemical and mechanical stimuli.

Extending this concept from energy devices to structural composites, a non-intrusive graphene nanoplatelet/epoxy sensor is then co-cured within glass fiber–reinforced polymers (GFRPs) using stencil printing. Benefiting from seamless material compatibility, the embedded sensor combines the inherent strength of GFRPs with broadband sensitivity, detecting responses from quasi-static strains to ultrasonic guided waves up to 600 kHz. This highlights the potential of structurally integrated

nanocomposite sensors for in situ SHM, while preserving the host composite's mechanical integrity.

While these efforts demonstrate feasibility, ensuring reliable and scalable fabrication becomes critical for practical applications. To accommodate this, AJP is employed to precisely formulate and deposit graphene/cellulose nanocrystal (CNC) inks with varied concentrations. Process optimization ensures uniform deposition, and the resulting sensors exhibit tunable sensitivity and stable performance across strain regimes ranging from quasi-static to ultrasonic. This advancement underscores the capability of AJP to deliver reproducible and customizable nanocomposite sensors tailored for diverse monitoring needs.

The broad frequency responsiveness of AJP-printed sensors further enables their application in both wearable healthcare and SHM. A polyurethane-encapsulated graphene/CNC acoustic sensor is developed using AJP, which demonstrates high sensitivity (9.7×10^{-6} dB^{-1}) and achieves 95.9% accuracy in digit recognition assisted by machine learning, offering an assistive platform for individuals with speech impairments. At higher frequencies, the printed sensor network embedded into glass fiber–reinforced polymer (GFRP) laminates captures impact waves, enabling accurate impact localization and advancing SHM in demanding environments. These embedded demonstrations highlight that AJP-printed sensors can be seamlessly integrated into structural composites, suggesting a natural progression toward manufacturing not only

the sensing components but also the structural host itself via additive manufacturing.

Building on this concept, this research advances the framework of “totally-additive-manufacturing” by combining FDM with AJP to fabricate multifunctional CFRP composites. Structural and sensing components are directly printed in a seamless process, producing composites with embedded nanocomposite networks that maintain mechanical integrity while offering ultrahigh sensitivity to strains and ultrasonic perturbations up to 200 kHz. This approach demonstrates a new paradigm for multifunctional structural design, where load-bearing capacity and self-sensing capabilities are integrated by design rather than retrofitted.

In conclusion, this PhD study establishes a comprehensive framework for the design, fabrication, and application of broadband nanocomposite sensors, spanning from standalone devices to fully integrated multifunctional composites, by leveraging advancements in additive manufacturing. By uniting low-dimensional conductive materials with additive manufacturing technologies, this research not only expands the fundamental understanding of scalable sensing architectures but also opens practical pathways for real-time monitoring in energy systems, wearable healthcare, and advanced structural composites. The outcomes highlight the transformative potential of additive manufacturing in creating next-generation multifunctional structures that combine mechanical robustness with intelligent self-sensing capabilities.

A LIST OF PUBLICATIONS ARISING FROM THIS THESIS

Refereed Journal Papers

1. **Wang, Q.**, Ma, M., Duongthipthewa, A., Zhang, W., Lang, Y., Luo, G., & Su, Z. (2025). "Totally-additive-manufacturing"-functionalized carbon fiber-reinforced polymer composites with an ultrasensitive self-sensing network. *Composites Part A: Applied Science and Manufacturing*, 189, 108596.
2. **Wang, Q.**, Li, P., Yuan, Q., Zhang, W., Ma, M., Luo, G., Lang, Y., Zhou, L., & Su, Z. (2025)**.** An aerosol jet-printed wearable graphene/cellulose nanocrystal acoustic sensor for speech recognition. *ACS Sensors*, 10, 8521−8530.
3. **Wang, Q.**, Duongthipthewa, A., Zhang, R., Liu, X., Zhang, J., LI, X., & Zhou, L. (2025). Implantable graphene/PVA-coated glass fiber for real-time strain monitoring in structural batteries under electrochemical cycling and external loading. *Composites Part A: Applied Science and Manufacturing*, 199, 109198.
4. **Wang, Q.**, Tian, Y., Duongthipthewa, A., Zhang, J., Liu, M., Su, Z., & Zhou, L. (2023). An embedded non-intrusive graphene/epoxy broadband nanocomposite sensor co-cured with GFRP for in situ structural health monitoring. *Composites Science and Technology*, 236, 109995.
5. Tian, Y., **Wang, Q.**, Liu, M., Zhang, J., & Zhou, L. (2023). Robust and quantitative characterization of aircraft icing with mode and frequency selective ultrasonic

guided wave. *Ultrasonics*, 127, 106846. (**Co-first Author**)

6. Liu, X., **Wang, Q.**, & Zhou, L. (2025). In-situ constructing robust interface with solid–solid bi-continuous phase electrolyte enables carbon fiber structural energy storage composites with increased multifunctional efficiency. *Composites Part A: Applied Science and Manufacturing*, 197, 109051.
7. Liu, X., Peng, Y., **Wang, Q.**, & Zhou, L. (2025). In-situ-interface-engineered mechanically robust solid polymer electrolyte for carbon fiber reinforced structural battery composites. *Composites Science and Technology*, 270, 111305.
8. Lang, Y., Yang, Z., Su, Z., **Wang, Q.**, & Chen, X. (2025). A frequency diverse array (FDA) of dispersive lamb waves for grating lobes suppression. Mechanical Systems and Signal Processing, 241, 113517.
9. Duongthipthewa, A., Zhou, H., **Wang, Q.**, & Zhou, L. (2024). Non-additive polymer matrix coated rGO/MXene inks for embedding sensors in prepreg enhancing smart FRP composites. *Composites Part B: Engineering*, 270, 111108.
10. Zhu, J., Su, Z., **Wang, Q.**, Hao, R., Lan, Z., Chan, F. S. F., & Wong, S. W. F. (2024). Process parameter effects estimation and surface quality prediction for selective laser melting empowered by Bayes optimized soft attention mechanism-enhanced transfer learning. *Computers in Industry*, 156, 104066.
11. Zhu, J., Su, Z., **Wang, Q.**, Lan, Z., Chan, F. S. F., Han, Z. & Ngan, A. C. F. (2024). Surface quality prediction and quantitative evaluation of process parameter effects for 3D printing with transfer learning-enhanced gradient-boosting decision trees. *Expert Systems with Applications*, 237, 121478.

12. Zhu, J., Su, Z., Han, Z., Lan, Z., **Wang, Q.**, & Ho, M. M. P. (2023). An ensemble approach for enhancing generalization and extendibility of deep learning facilitated by transfer learning: principle and application in curing monitoring. *Smart Materials and Structures*, 32(11), 115022.
13. Zhu, J., Su, Z., **Wang, Q.**, Yu, Y., Wen, J., & Han, Z. (2023). Curing process monitoring of polymeric composites with Gramian angular field and transfer learning-boosted convolutional neural networks. *Smart Materials and Structures*, 32(11), 115017.

Submitted Journal Papers

1. **Wang Q**, Su Z, Zhou L. A review on self-sensing fiber-reinforced polymer composites: mechanisms, fabrications, and applications. (2025). *Measurement*. (under review)
2. Duongthipthewa A, **Wang Q**, Zhang J. Multifunctional Fiber-Reinforced Composites: Embedded Reduced Graphene Oxide/Mxene Sensors for Real-Time Cure and Structural Health Monitoring. (2025). *Composites Science and Technology*. (**Co-first Author**)

ACKNOWLEDGEMENTS

First and foremost, I would like to express my heartfelt gratitude to my supervisors, Prof. Zhongqing Su and Prof. Limin Zhou. I feel truly fortunate to have had the privilege of being their PhD student. Prof. Zhou opened the door to this research journey and patiently guided me in building the foundation of my academic path. Prof. Su, with his meticulous, step-by-step guidance, not only taught me how to write scientific papers and think critically, but also inspired me to approach research with curiosity, courage, and persistence. What impressed me most was that no matter the challenges or obstacles I encountered, he always managed to find a way forward. His remarkable problem-solving ability and unwavering support gave me the confidence that no difficulty was insurmountable under his guidance. Despite his extremely busy schedule, he always made time to revise my manuscripts—sometimes even working on them while traveling.

My sincere thanks also go to Prof. Menglong Liu (Harbin Institute of Technology (Shenzhen)), Prof. Zhihui Zeng (Shandong University). Their invaluable guidance, generous help, and inspiring discussions have broadened my vision and enriched this work in ways I could never have achieved alone. I feel deeply fortunate to have crossed paths with them during this journey.

I would also like to extend my heartfelt thanks to the staff of the university research

facility in 3D printing (U3DP) laboratory, especially Mr. Tab and Mr. Frankie in U3DP, whose tireless support made so much of my experimental work possible. Whenever the equipment encountered problems, Tab was always the first to rush in and do everything he could to help resolve them.

I am equally grateful to my friends and peers, including Ms. Ming Ma, Mr. Guojie Luo, Mr. Wanglinhan Zhang, Ms. Yanfeng Lang, Mr. Qi Yuan, Mr. Pengfei Li, Dr. Yi He, Dr. Lei Fan, Mr. Xinze Guo, Ms. Xin Gong, Mr. Jie Huang, Mr. Jiaxing Tian, Mr. Jianbin Li, Dr. Jiangang Xu, Dr. Anchalee, Dr. Yiyin Su, Dr. Linlong Lv, Dr. Jianjian Zhu, Dr. Pengyu Zhou, Dr. Yaozhong Liao, Dr. Xu Liu, Ms. Jing Zhang, Ms. Xiating Li, Mr. Ruiyuan Zhang, and Mr. Zihan Hu, who have walked alongside me through both the struggles and joys of this journey. The countless hotpot dinners, barbecues, and shared meals we enjoyed together not only brought warmth and laughter to my life, but also lifted me from moments of stress and discouragement. Without their companionship and kindness, this PhD journey would not have been as colorful, fulfilling, or memorable.

Finally, my utmost acknowledgement goes to my most beloved mother, father, sister, and boyfriend Roy Wang, for their encouragement, support and unconditional love. Without their constant care and understanding, I could not have persevered through this journey.

NOMENCLATURE

Acronyms and Initialisms

FRP	Fiber-reinforced polymer
2D	Two-dimensional
AM	Additive manufacturing
LIBs	Lithium-ion batteries
AJP	Aerosol jet printing
CFRP	Carbon fiber-reinforced polymer
FDM	Fused deposition modeling
SHM	Structural health monitoring
PVA	Polyvinyl alcohol
CNC	Cellulose nanocrystal
PU	Polyurethane
DIW	Direct ink writing
PDMS	Polydimethylsiloxane
PI	Polyimide
PEN	Polyethylene naphthalate
GNP	Graphene nanoplatelet
rGO	Reduced graphene oxide
PLA	Polylactic acid
ABS	Acrylonitrile butadiene styrene copolymer

CNTs	Carbon nanotubes
TPU	Thermoplastic polyurethane
FR	Focusing ratio
GUW	Guided ultrasonic wave
SOH	State-of-health
SOC	State of charge
CMC	Carboxymethyl cellulose
EVA	Ethylene–vinyl acetate
ALS	Amyotrophic lateral sclerosis
LIG	Laser-induced graphene
PE	Polyethylene
NDT	Non-destructive testing
GP-GFS	Graphene-polyvinyl alcohol -coated glass fiber sensor
GFRP	Glass fiber-reinforced polymer
SEM	Scanning electron microscopy
Xrd	X-ray diffraction
GF	Gauge factor
Li-ion	Lithium-ion
CV	Constant voltage
CC	Constant current
BMS	Battery management systems

ER	Electrical resistance
PZT	Lead zirconate titanate
DI water	Deionized water
sccm	Standard cubic centimeter per minute
EDS	Energy dispersive spectrometer
STFT	Short-time Fourier transform
RMS	Root mean square
FFT	Fast Fourier transform
SNR	Signal-to-noise ratio
SPLs	Sound pressure levels
SVM	Support vector machine
RBF	Radial basis function
MFCCs	Mel-frequency cepstral coefficients
TDOA	Time-Delay-of-Arrival
ILSS	Interlaminar Shear Strength

Symbols

ν	Poisson's ratio
ε	Strain
ρ	Resistivity
R_c	Tunneling resistance
J	Tunneling current density
V	Potential difference

e	Electric charge
m	Electron mass
h	Planck's constant
d	Distance between nanofiller
λ	Base potential height
A	Cross-sectional area
ΔR	Change in the electrical resistance
R_0	Initial electrical resistance
$\frac{\Delta R}{R_0}$	Relative electrical resistance
ε_t	Tensile strain
GF_t	Gauge factor under tensile strain
ε_f	Flexural strain
σ_f	Flexural stress
h_0	Thickness of composites
b	Width of GFRP composites
δ	Midspan deflection
F	Applied load
GF_f	Gauge factor under flexural strain
S_0	Zeroth-order symmetric Lamb wave
P	Sound pressure
P_0	Reference sound pressure

S	Sensitivity to sound
ΔSPL	Change in sound pressure level
M	Number of percolation pathways
Γ	Tunneling probability
E	Fermi energy level
T	Temperature
k_b	Boltzmann constant
μ	Electrochemical potential
d_{vdw}	van der Waals equilibrium separation
d_{tunnel}	Tunneling distance
d_{cutoff}	Tunneling cutoff distance
P_i	Sensor i
t_i	Arrival times of the impact wave at sensor P_i
v_i	Wave propagation velocities from assumed impact point to sensor P_i
Δt_{ij}	Hyperbola with foci at P_i and P_j
$I(x, y)$	Pixel value
t	Time
E_t	Normalized signal envelope at time t
$\Delta t_i(x, y)$	Theoretical propagation delay from (x, y) to sensor P_i

TABLE OF CONTENTS

LIST OF FIGURES

LIST OF TABLES

CHAPTER 1

Introduction

1.1 Background and Research Motivation

The rapid development of fiber-reinforced polymer (FRP) composites has enabled their widespread deployment in aerospace, civil infrastructure, and renewable energy applications, owing to their outstanding strength-to-weight ratio [1-4]. The challenge of integrating sensors into FRP composites for integrity monitoring has long persisted. A dense sensor network renders rich information, but the inclusion of it into the composites unavoidably deteriorates the original structural integrity; in contrast, a sparse sensor network, which minimizes the intrusion to the host composites, may provide limited information only and accordingly fail to evaluate the structural integrity accurately. This dilemma has impeded the progress of developing functionalized composites with integrated sensing capabilities. In these domains, there is a growing demand for sensing systems that not only deliver superior sensitivity and lightweight but also nondestructive integrate real-time monitoring capabilities to ensure safety, reliability, and long-term functionality.

Low-dimensional conductive nanomaterials provide a promising route for developing lightweight and high-performance sensors for composite health monitoring. Carbon-based materials such as graphene combine excellent conductivity, flexibility, low density, and scalability, making them attractive for piezoresistive strain sensing, with graphene showing particularly strong sensitivity to external deformation [5-7]. More recently, MXenes—two-dimensional (2D) transition metal carbides and nitrides—have emerged with exceptional conductivity [8, 9], hydrophilicity, and multifunctional properties, offering new opportunities for next-generation nanocomposite sensors. Parallel to these material advances, the past decade has witnessed rapid progress in additive manufacturing (AM), which provides unprecedented opportunities for producing multifunctional materials and integrated structures. When combined with AM, these low-dimensional conductive nanomaterials can be processed into scalable, flexible, and reproducible sensing platforms, where the uniformity and consistency of sensor fabrication are well ensured. The convergence of advanced nanomaterials with AM-driven manufacturing thus opens new avenues for developing multifunctional sensors that are lightweight, integrable, and capable of broadband, high-fidelity monitoring across diverse application scenarios.

In the field of electrochemical energy systems, particularly electric vehicles and aerospace structural batteries, the safety and reliability of lithium-ion batteries (LIBs) are of paramount importance [10-12]. LIBs provide high energy density and long cycle life [13-15], yet they suffer from performance degradation, mechanical swelling, and

thermal runaway risks during charge–discharge cycling or under mechanical abuse. These issues are especially critical when batteries are structurally embedded, where electro-chemo-mechanical interactions may accelerate interfacial aging and trigger catastrophic failures such as fire [16, 17]. Conventional diagnostic tools—such as X-ray diffraction [18, 19], neutron imaging [20], and digital image correlation [21]—are powerful in laboratory studies but impractical for in situ and real-time monitoring in operating systems due to their complexity and cost [22, 23]. Existing sensor-based solutions, including force sensors and optical fiber sensors [24-30], either lack conformability or are vulnerable to mechanical damage. In contrast, nanocomposite piezoresistive sensors provide a unique opportunity: they are lightweight, flexible, highly sensitive, and minimally invasive [23, 31, 32]. By embedding such sensors into structural batteries, it becomes possible to directly probe strain evolution, detect early-stage degradation, and prevent failure, paving the way toward safer and more intelligent energy storage systems.

Beyond batteries, wearable bioelectronic sensors have emerged as transformative tools for healthcare and human–machine interaction [33-35]. Among these, wearable acoustic sensors hold unique value for individuals with speech impairments, where decoding subtle throat vibrations enables alternative communication pathways [36, 37]. Traditional fabrication techniques for wearable electronics, such as spraying or lithography, suffer from material waste, limited adaptability, and poor compatibility with soft, curved human skin. Nanocomposite sensors combine flexibility,

biocompatibility, and high piezoresistive sensitivity, making them ideal for epidermal interfaces [38-43]. Coupled with additive manufacturing techniques such as aerosol jet printing (AJP), these sensors can be precisely patterned onto soft, conformal substrates, achieving robust skin adhesion and noise suppression. Integrated with machine learning algorithms, they enable high-fidelity speech recognition, offering practical solutions for digital healthcare and rehabilitation.

On the other hand, the last decade has witnessed unprecedented prosperity in AM techniques, which have opened up numerous opportunities to develop multi-material structures and functional materials. With high precision, cost-efficiency, a high degree of automation, and flexibility in material selection, the AM techniques today have catalyzed the design and manufacturing of complex engineering structures [51, 52], functional materials [53-56], hybrid electronics [57, 58] and among many others. In particular, AJP, an emerging AM approach, has been proven capable of precisely decorating fine features on various types of substrates [59-62], offering advantages such as freeform deposition and flexible selection of a broad spectrum of materials, as a result of its good tolerance to material viscosity from 1 to 1000 cP. AJP has become a highly competent candidate AM technique for digital, integrated manufacturing of sensors, batteries, and microcontroller units [53-56]. In conjunction with continuous fiber printing [51, 52, 63-66], AJP has laid the groundwork for fabricating advanced carbon fiber-reinforced polymer (CFRP) composites with self-sensing capability, heralding a new era in intelligent and adaptive structural design and manufacturing.

Techniques such as AJP and fused deposition modeling (FDM) allow the fabrication of multifunctional composites where structural reinforcement and sensing elements are printed in a unified process. By embedding ultrathin nanocomposite sensors directly into CFRP architectures, it becomes possible to achieve wideband strain monitoring—from quasi-static loading to ultrasonic guided waves—without degrading host performance.

1.2 Research Objectives

In recognition of the critical limitations of prevailing sensing technologies—such as rigidity, fragility, poor conformability, and incompatibility with real-time embedded monitoring in operational environments, this PhD research aims to develop the breeds of nanomaterial-based multi-physics sensors using additive manufacturing techniques, to enable integrated sensing for battery health monitoring, composite structural integrity assessment, and human health via sound recognition in wearable devices. The core innovation lies in a hybrid manufacturing framework that enables the seamless integration of sensors within host structures during their fabrication process. To achieve the above aims and address the inefficiencies of existing methods as briefed above, the following specific objectives are set:

i) To design and formulate nanocomposite sensing inks based on graphene, with tailored rheology, printability, and electrical functionality for additive manufacturing;

ii) To fabricate and characterize nanocomposite sensors using advanced AM techniques (e.g., AJP, hybrid printing), achieving conformal deposition on flexible circuits and composite substrates;

iii) To tailor the microstructural features of the nanocomposite sensors for enhanced sensitivity, and to systematically evaluate the sensing performance of the fabricated devices—including quasi-static strain, vibration, acoustic response, and ultrasonic guided wave, from battery cycling to ultrasonic wave excitation;

iv) To demonstrate the application of implantable nanocomposite sensors for real-time monitoring of LIBs, enabling detection of state-of-charge, degradation, and external impact events;

v) To embed and validate nanocomposite sensing networks in FRP/CFRP composites, achieving broadband strain monitoring and acousto-ultrasonic damage detection for structural health monitoring (SHM);

vi) To develop and validate wearable graphene-based acoustic sensors fabricated by AM, for decoding subtle throat vibrations and enabling speech recognition through integration with machine learning algorithms;

vii) To explore the framework of “totally-additive-manufacturing” multifunctional composites by integrating nanocomposite sensors with continuous fiber printing, thereby paving the way toward intelligent, adaptive structures.

1.3 Scope of the Thesis

This thesis is systematically structured to explore the design, additive manufacturing, and application of nanocomposite-based sensors across multiple engineering domains, with a particular focus on SHM and multifunctional integration. The research progresses from fundamental material development to practical proof-of-concept demonstrations across several engineering applications.

Chapter 2 offers a comprehensive literature review on low-dimensional nanomaterials and their processing into nanocomposites via AM. Emphasis is placed on the connection between sensing mechanisms and their applicability in areas such as battery health monitoring, wearable acoustic sensing, and guided-wave-based SHM for composites. This chapter lays the scientific groundwork and identifies the research gaps addressed in this thesis.

Chapter 3 shifts the focus to battery health monitoring. Here, graphene/ polyvinyl alcohol (PVA)-based fiber sensors are fabricated and deployed to track strain evolution during charge–discharge cycles and to detect external mechanical impacts. This

approach allows for real-time, minimally invasive monitoring of lithium-ion battery behavior.

In Chapter 4, non-intrusive graphene/epoxy nanocomposite sensors are developed and embedded within FRP composites. Their performance is evaluated across a spectrum from quasi-static loads to ultrasonic wave detection. Crucially, this chapter also experimentally verifies that sensor integration does not compromise the host composite's mechanical properties.

Chapter 5 explores AJP of graphene/cellulose nanocrystal (CNC) nanocomposite sensors. Through systematic optimization of printing parameters and material microstructure, the sensing performance is characterized under both low-frequency dynamic strains and high-frequency ultrasonic guided waves.

Building on this, Chapter 6 extends the use of aerosol jet-printed sensors to wearable acoustic devices. A prototype wearable sensor is fabricated by encapsulating the device in a biocompatible polyurethane (PU) film, ensuring conformal skin contact and stable adhesion. The chapter evaluates the acoustic sensing performance across different microstructural configurations and demonstrates the device’s ability to distinguish speaker gender, intonation, and speech rhythm.

Chapter 7 configures aerosol jet-printed nanocomposite sensors into distributed

networks for impact monitoring in composite laminates. Embedded within FRP structures, these sensors are validated for real-time impact localization using guided ultrasonic waves.

Chapter 8 introduces a fully additive manufacturing approach for functional composites. By integrating aerosol jet-printed sensors with FDM-printed continuous carbon fiber composites, a unified structural-sensing system is realized that maintains interfacial integrity and supports both quasi-static and high-frequency ultrasonic monitoring. This chapter establishes a scalable framework for future intelligent composite systems.

Finally, Chapter 9 summarizes the key contributions of the thesis and suggests promising directions for future research in the field of AM-enabled multifunctional sensing systems.

CHAPTER 2

The State of the Art of Nanocomposites-based Sensing Techniques: A Review

2.1 Introduction

This chapter reviews the foundational elements that enable modern nanocomposite sensing. It begins by examining the material constituents, focusing on the properties of low-dimensional nanocomposites, particularly carbon-based materials like graphene and emerging MXenes. The discussion then elucidates the core sensing mechanisms that govern their piezoresistive response. The discussion then focuses on AM techniques for printing sensors, analyzing the capabilities of FDM, direct ink writing (DIW), and the highly relevant AJP method. Their respective advantages, limitations, and suitability for creating functional sensing patterns are critically evaluated. Finally, the chapter explores the diverse application scenarios, from low-frequency wearable acoustic sensing to high-frequency ultrasonic wave detection, framing the specific performance requirements that drive sensor design and material selection.

2.2 Low-dimensional Materials

Piezoresistive flexible sensors have gained increasing interest, underscoring the need for conductive materials with high stability and durability. Among them, graphene offers outstanding conductivity, mechanical strength, and strain sensitivity, while MXenes provide complementary advantages such as excellent conductivity, hydrophilicity, and multifunctionality. These low-dimensional materials thus stand out as the most promising platforms for next-generation flexible sensors.

2.2.1 Graphene-based Nanocomposite Sensors

Graphene-based piezoresistive sensors have attracted significant attention due to the exceptional electrical, mechanical, and structural characteristics of graphene and its derivatives [67-69]. As a 2D carbon nanomaterial, graphene exhibits ultrahigh conductivity, mechanical robustness, large specific surface area, and good thermal stability [70-77]. However, pristine graphene suffers from inherent challenges, including sheet restacking, limited dispersibility in solvents, and weak interfacial interactions with insulating hosts, which compromise its processability and long-term reliability [67]. To address these issues, graphene is commonly hybridized with polymers, metals, oxides, or ceramics to form nanocomposites with tailored functionalities [78-81].

The choice of matrix plays a pivotal role in flexible sensor fabrication. Elastomers such as polydimethylsiloxane (PDMS), PU, polyimide (PI), and polyethylene naphthalate

(PEN) have been widely employed to host graphene nanoplatelets (GNPs) or reduced graphene oxide (rGO) networks [82-86]. Their softness, deformability, and chemical stability enable molding into diverse geometries and integration into wearable, transparent, or acoustically responsive devices [5-7, 87, 88].

In sensing applications, graphene-based nanocomposites rely on percolated conductive networks to transduce mechanical or environmental perturbations into measurable resistance changes. Advances in dispersion control and interfacial functionalization have improved reproducibility and device stability, enabling applications ranging from strain and pressure sensing to ultrasonic monitoring for structural health evaluation. Nevertheless, issues such as filler restacking, heterogeneous dispersion, and weak interfacial bonding continue to limit the stability and repeatability of graphene-based sensors. These challenges have prompted the exploration of alternative low-dimensional nanomaterials, among which MXenes have recently emerged as highly promising candidates.

2.2.2 MXene-based Nanocomposite Sensors

MXenes, a novel family of 2D layered nanomaterials, have recently emerged as graphene analogues with distinct advantages for sensing applications. They are typically derived from MAX phase precursors ($M_{n+1}AX_n$, n = 1–3), which are layered ternary carbides, nitrides, or carbonitrides, by selectively etching away the A element (groups 13 or 14) [8, 89, 90]. More than 60 MXene compositions have been identified,

incorporating early transition metals such as Ti, V, Cr, Nb, Mo, or Ta. These materials combine metallic conductivity with ceramic-like stability, distinguishing them from both graphene and conventional nanomaterials [91-93].

MXenes offer additional advantages rooted in their surface chemistry. Their 2D layers are rich in functional groups (–OH, –O, –F), which improve dispersibility and strengthen interfacial bonding with polymer or ceramic matrices [91-95]. The combination of high conductivity, tunable interlayer spacing, and large specific surface area provides an adjustable resistance response, endowing MXene-based composites with excellent sensitivity to mechanical and environmental stimuli.

$Ti_3C_2T_x$ MXene, in particular, has become a benchmark for piezoresistive pressure and strain sensors, offering ultrahigh sensitivity, fast response, and low detection limits [90]. Its layered structure not only enhances flexibility and signal stability but also allows effective integration with elastomeric or fibrous insulating substrates. These attributes make MXenes highly suitable for applications spanning wearable electronics, pressure mapping, and ultrasonic sensing for SHM [8, 91-99].

Despite these promising features, MXene-based sensors also face challenges, including oxidation instability, surface termination variability, and difficulties in achieving uniform dispersion within insulating hosts. These unresolved issues, coupled with the limitations observed in graphene-based systems, highlight the need for advanced

fabrication routes. In this context, AM provides a promising pathway to tailor architectures, optimize filler distribution, and enable scalable production of low-dimensional nanocomposite sensors for multiphysics monitoring.

2.3 Additive Manufacturing of Nanocomposite Sensors

AM offers digital, scalable, and maskless routes for fabricating nanocomposite sensors, enabling precise material deposition and seamless integration with diverse structures. Among the widely adopted methods, FDM, DIW, inkjet printing, and AJP each provide unique advantages in resolution, material compatibility, and application scope.

2.3.1 Fused Deposition Modeling

FDM is one of the most widely used additive manufacturing processes, valued primarily for its affordability and effectiveness in rapid prototyping. The technique operates by heating, melting, and extruding a polymer filament through a heated nozzle, depositing material layer-by-layer onto a build platform to fabricate three-dimensional objects. A notable limitation of FDM, however, is its relatively low printing resolution, which stems from the use of nozzles typically ranging from 0.25 to 0.4 mm in diameter, resulting in a minimum feature size of approximately 250 μm [100]. Common feed materials include thermoplastic polymers such as polylactic acid (PLA) and acrylonitrile butadiene styrene copolymer (ABS). In addition, conductive polymer

composite filaments have been developed for printing functional electronic components. Examples include graphene/PLA, carbon fiber/PLA, and copper-based polymer composites, with volume resistivities of 0.6 Ω·cm, 30 Ω·cm, and 0.006 Ω·cm, respectively [101]. These conductive filaments are typically produced by melt-blending conductive nanomaterials—such as graphene, carbon nanotubes (CNTs), or MXenes—with thermoplastic matrices using extruders, as shown in Figure 2.1. However, due to the difficulty in achieving a homogeneous dispersion of nanomaterials within the polymer, even at low volume fractions, the electrical conductivity and sensing performance of these composites are often compromised. The resulting inhomogeneity and limited percolation networks lead to inferior and inconsistent electromechanical properties [102]. Consequently, FDM-printed sensors generally exhibit reduced accuracy and are often restricted to applications involving large strains or temperature variations, where high sensitivity is not critical. Nevertheless, these materials still hold promise for applications such as resistors [101] and electrochemical devices [103, 104], particularly when enhanced through post-processing treatments including thermal, chemical, or electrochemical methods.

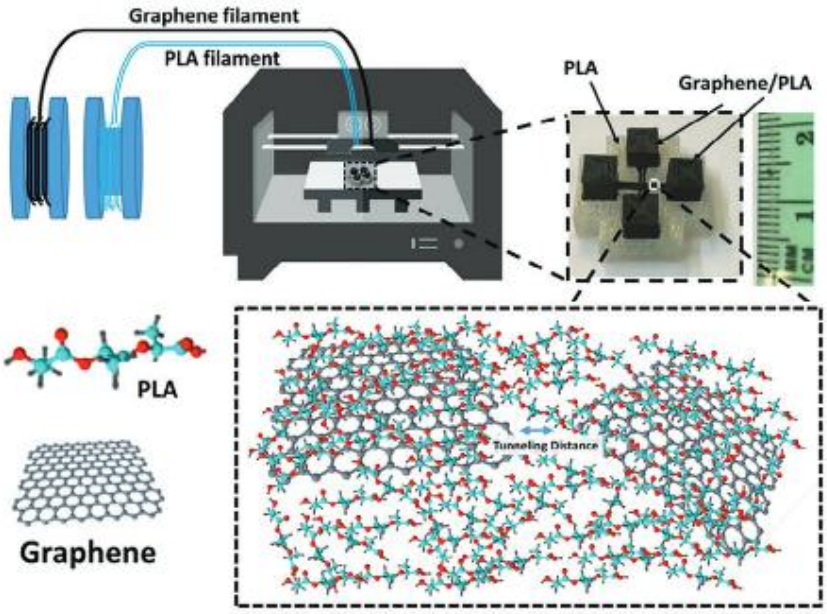

Figure 2.1 FDM technique for printing the nanocomposite sensors [105].

2.3.2 Direct Ink Writing

DIW is an extrusion-based additive manufacturing technique in which liquid-phase inks are deposited through a nozzle and subsequently solidified, either by solvent evaporation, thermal curing, or UV irradiation, to construct three-dimensional structures layer by layer (Figure 2.2). The process is highly versatile and compatible with a broad range of materials, provided that the ink satisfies specific rheological requirements, including appropriate viscosity (10^2–10^6 cP at $\approx 0.1\ s^{-1}$), shear-thinning behavior, yield stress, and viscoelasticity [106]. Typical DIW inks consist of conductive fillers, binders, additives, and solvents, where fillers such as carbon black, CNTs, graphene, MXenes, or metallic nanoparticles provide conductivity, and polymeric binders such as silicone rubber or thermoplastic polyurethane (TPU) ensure uniform dispersion and mechanical integrity [107-110]. Additives and solvents are frequently

incorporated to optimize rheological properties and printing fidelity [111].

DIW has demonstrated remarkable flexibility for fabricating functional electronic components, with feature sizes down to several micrometers [112]. Conductive inks based on metals [113], metal alloys [114], liquid metals [112], and conducting polymers [115] have been successfully printed. More advanced strategies, such as multicore–shell DIW, enable the co-extrusion of multiple inks to build multilayered architectures, extending its utility to strain sensors and other complex devices. For nanocomposite sensors, DIW offers the advantage of integrating high loadings of functional fillers into viscoelastic matrices, producing flexible structures with tunable electrical responses. However, ink formulation remains a critical challenge. Achieving stable dispersion of low-dimensional nanomaterials while maintaining the rheological balance required for printability is difficult, often resulting in trade-offs between conductivity, mechanical performance, and reproducibility. Furthermore, the relatively large nozzle diameters constrain printing resolution, limiting DIW-based sensors to applications where larger-scale strain, pressure, or temperature responses are sufficient.

These limitations have driven the exploration of alternative additive manufacturing approaches capable of higher precision and finer control over material deposition. Inkjet printing and AJP, in particular, have emerged as promising techniques for fabricating nanocomposite sensors with enhanced resolution, structural complexity, and sensing performance.

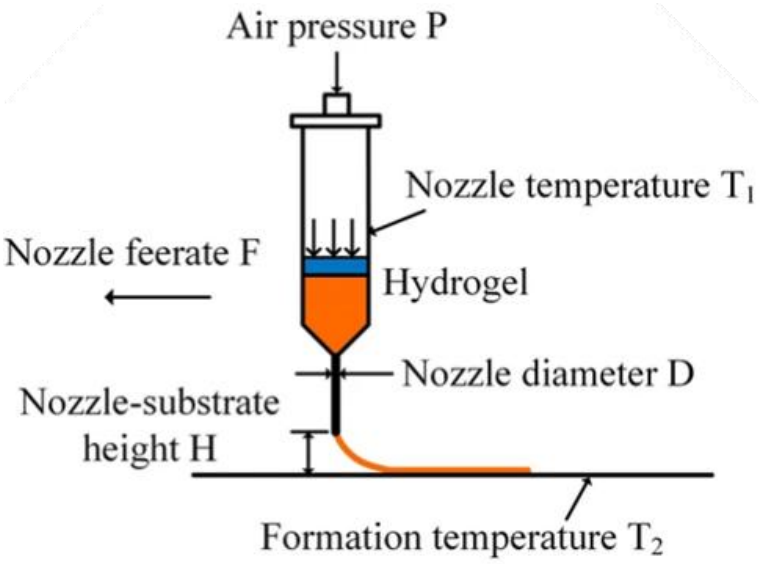

Figure 2.2 Schematic representation of DIW [116].

2.3.3 Inkjet

Inkjet printing is a non-contact additive manufacturing technique in which droplets are generated and ejected from a nozzle by pressure pulses (Figure 2.3), typically induced through thermal or piezoelectric actuation. By synchronously controlling droplet ejection and substrate positioning, materials can be deposited layer by layer to construct patterned structures [117]. The droplet volume typically lies in the picoliter range, which defines the feature resolution of inkjet printing to tens of micrometers [118]. Owing to its digital, maskless nature, inkjet printing has been widely adopted for printed electronics. Metal nanoparticle- or flake-based inks, followed by sintering, represent one of the most established approaches for fabricating highly conductive electrodes [119]. Beyond metals, carbon nanomaterials such as graphene [120] and CNTs [121], as well as conducting polymers [122], have also been formulated into printable inks for

applications in sensors, transistors, and other electronic devices. Multilayer deposition enables the construction of quasi-3D (2.5D) architectures, extending the scope of inkjet-printed functional components.

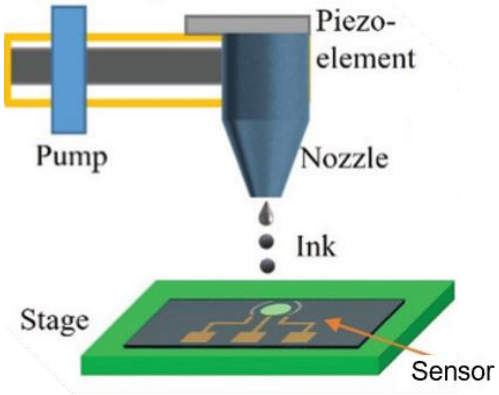

Figure 2.3 Schematic representation of inkjet [123].

Despite its advantages of high resolution and material versatility, inkjet printing also faces several limitations in sensor fabrication. The requirement for low- to medium-viscosity inks constrains filler loading, often leading to poor conductivity in nanocomposite-based sensors [105, 123, 124]. Multiple printing and sintering steps are typically necessary to build functional devices, which reduces process efficiency. Furthermore, the inability to deposit on non-planar or curved substrates significantly restricts its applicability for integrated sensors in complex geometries.

2.3.4 Aerosol Jet Printing

The inherent limitations of FDM, DIW, and inkjet printing, particularly their restricted filler loading, limited resolution, and inability to conformally print on nonplanar

surfaces—have driven interest in advanced additive manufacturing techniques. AJP has emerged as a versatile alternative, offering high precision, structural flexibility, and the unique ability to deposit functional materials directly onto complex three-dimensional or curved substrates.

In AJP, functional inks are first atomized into fine droplets using pneumatic or ultrasonic atomizers. These droplets are transported by a carrier gas (e.g., N_2 or He) toward the print head, where they are confined and accelerated by an annular sheath gas flow to form a tightly focused aerosol jet [125-127]. A key processing parameter is the focusing ratio (FR)—the ratio of sheath gas to carrier gas flow—which governs the line definition, thickness, and aspect ratio of the deposited features. If the FR is not carefully optimized, the printed lines may lose uniformity or spread uncontrollably [127, 128]. Unlike inkjet printing, which is constrained by low-viscosity inks and droplet spreading, AJP is a maskless and non-contact technique capable of producing well-defined patterns with line widths down to 6–20 μm. Its 2–5 mm standoff distance allows printing without direct contact, enabling conformal deposition on flexible or irregular substrates while avoiding the need for alignment masks or etching steps (Figure 2.4). Moreover, AJP supports a wide viscosity window (1–1000 cP) [105, 123, 124], accommodating inks formulated with nanomaterials such as graphene, CNTs, MXenes, and metallic nanoparticles [129-132]. This broad material compatibility, combined with superior film uniformity and suppression of coffee-ring artifacts, makes AJP highly suited for constructing reproducible, high-performance nanocomposite sensors.

These distinctive advantages position AJP as a key technology for next-generation multifunctional sensors, particularly in applications that demand fine structural control, integration on curved surfaces, and high sensitivity in acoustic or ultrasonic monitoring.

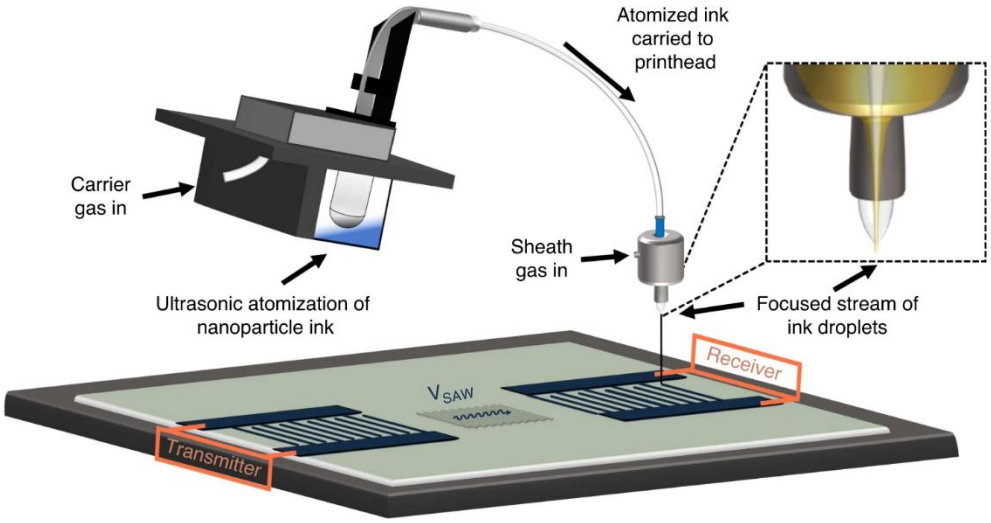

Figure 2.4 Schematic representation of AJP [133].

2.4 Sensing Mechanism of Nanocomposite Sensors

The operation of piezoresistive nanocomposite sensors fundamentally relies on how conductive networks respond to external stimuli through resistance variation. Several key mechanisms—geometric effect, piezoresistive effect, fracture effect, and tunneling effect—have been identified as the dominant pathways for transduction, each associated with specific material configurations and applicable frequency ranges.

2.4.1 Geometric Effect

The geometric effect constitutes the most straightforward mechanism in piezoresistive sensing, directly linking dimensional variations of a conductor under strain with its resistance response. As described by the classical relation $R=\rho L/A$, elongation increases the conductive path length while simultaneously reducing the cross-sectional area, resulting in higher resistance. Although this model is conceptually simple, it captures the essential electromechanical coupling in many nanocomposite-based strain sensors [67, 68, 134].

In nanomaterial systems, the contribution of the geometric effect strongly depends on structural form. For continuous thin films such as CNT or graphene coatings, resistance change is usually dominated by nanoscale mechanisms (e.g., tunneling or crack propagation), and the role of geometry is relatively minor [135, 136]. By contrast, in fibrous or yarn-based architectures, geometric deformation becomes the primary source of resistance modulation. Twisting, helical alignment, and the textile arrangement of conductive fibers alter the effective contact area during stretching, giving rise to pronounced resistance changes [134, 137]. Architected 3D structures fabricated by additive manufacturing further illustrate how geometry dictates the electrical response, with different lattice designs producing distinct strain sensitivities [138].

Experimental reports across various nanomaterial platforms consistently highlight this effect. For example, composites of elastomers with dispersed carbon nanomaterials exhibit resistance variations largely attributable to changes in path length and cross-

sectional area under tensile loading. Similarly, CNT yarns and woven fabrics show resistance changes that can be directly traced to their macroscopic deformation modes [137]. Even in graphene-based structures, where quantum and interfacial effects are significant, lattice design has been shown to impose a geometric contribution that modulates the strain–resistance relationship.

2.4.2 Piezoresistive Effect

The piezoresistive effect refers to the intrinsic change in resistivity of materials under strain, distinct from purely geometric effects. This phenomenon is especially evident in semiconductors such as Si and Ge, where deformation modifies the interatomic spacing and band structure, leading to pronounced resistance variations [139-142]. At the nanoscale, CNTs and nanowires can also exhibit significant piezoresistive responses depending on chirality and barrier height [143, 144]. However, for graphene, the high carrier mobility results in weak intrinsic piezoresistivity, and thus it is more effective when combined with polymers or semiconductors to enhance sensitivity [142, 145, 146].

This mechanism can be formally represented by the relation $\Delta R/R=(1+2\nu)\varepsilon+\Delta\rho/\rho$, where the second term captures the contribution from intrinsic resistivity changes independent of geometry.

In nanocomposite systems, the overall resistance change typically arises from both

intrinsic piezoresistivity ($\Delta\rho/\rho$) and structural effects such as tunneling modulation or filler rearrangement. This hybrid behavior enables flexible and stretchable piezoresistive sensors [147, 148], which have been widely explored for SHM, wearable electronics, and soft robotics. Despite their potential, challenges remain regarding interfacial bonding and mechanical–electrical mismatch between nanomaterials and polymer matrices, which may hinder stability and reproducibility.

2.4.3 Fracture Effect

One of the most critical mechanisms underpinning the operation of nanocomposite strain sensors is the fracture-induced disruption of conductive networks. When conductive films or percolating networks are subjected to tensile strain, nanosheets, nanotubes, or nanoparticles progressively lose electrical contact. This process manifests either as visible crack propagation in thin films or as nanoscale disconnection among dispersed fillers. In both cases, the effective number of conductive pathways decreases, leading to a marked increase in electrical resistance [149, 150]. Upon strain release, partial closure of cracks or reestablishment of filler–filler contacts can restore conductivity, yielding reversible and repeatable responses [151-153].

At the microstructural level, conductive films composed of CNTs or graphene are prone to developing microcracks that evolve with strain, effectively fragmenting the network and amplifying resistance changes. Similarly, in composite systems where nanofillers are embedded in elastomeric matrices, relative sliding or separation of adjacent fillers

reduces contact area and disrupts tunneling junctions, thereby modulating the electrical signal [154, 155]. Both processes are inherently governed by the same principle of contact loss within the conductive network, though they occur at different structural scales.

This fracture-driven sensing mechanism offers several advantages. It endows strain sensors with ultrahigh sensitivity and rapid response owing to the abrupt change in conductive pathways. Gauge factors exceeding 10^3 have been reported by exploiting controlled crack generation or engineered filler disconnections [156]. Furthermore, strategies such as pre-stretching, structural patterning, or substrate roughness modulation have been employed to tailor crack initiation and propagation, thereby optimizing sensitivity and stretchability [151, 152].

Nevertheless, the mechanism also imposes intrinsic trade-offs. Excessive crack growth or irreversible disconnection may compromise linearity, introduce hysteresis, or limit the maximum strain range [154]. Thus, while fracture-induced mechanisms are particularly suitable for applications requiring high sensitivity in moderate strain ranges—such as human motion detection, tactile interfaces, or wearable monitoring devices—they require careful material and structural design to balance sensitivity with durability.

2.4.4 Tunneling Effect

The tunneling effect represents a quantum conduction mechanism that arises when adjacent conductive nanoparticles or nanofillers are separated by nanoscale insulating barriers, typically on the order of 1–3 nm [157-159]. Within this distance, electrons can penetrate the barrier via quantum tunneling, generating a tunneling current highly sensitive to even subtle variations in interparticle spacing (Figure 2.5). As a result, when the filler content of a composite is close to the percolation threshold, ultralow strains can induce pronounced changes in resistance, conferring extremely high sensitivity to microstrain or even nanostrain levels [160, 161]. This makes tunneling-dominated nanocomposite sensors uniquely suited for applications where conventional mechanisms are insufficient, such as guided ultrasonic wave (GUW) detection in SHM, operating at frequencies up to several MHz [162-166].

The contribution of tunneling resistance relative to other conductive pathways is strongly dependent on filler dispersion and network morphology. At low strain levels, resistance variations are primarily determined by tunneling junctions, while at larger deformations, mechanisms such as crack formation and contact loss tend to dominate [160, 161, 167]. For instance, graphene and CNT-based composites often exhibit multiple concurrent mechanisms; in loosely dispersed or near-threshold networks, tunneling governs the response, whereas in denser or entangled systems, geometrical effects or fracture pathways may prevail [168, 169]. Hybrid systems that combine graphene nanosheets with CNTs further illustrate this transition, where tunneling dominates at small strains (<0.2%) and contact resistance or crack evolution takes over

at higher strain regimes [169].

The extreme sensitivity of tunneling conduction can be quantitatively described by Simmons' tunneling resistance model, which relates tunneling resistance exponentially to barrier thickness and potential height [161, 167, 170].

$$R_c = \frac{V}{AJ} = \frac{h_2 d}{Ae^2\sqrt{2m\lambda}} = \exp\left(\frac{4\pi d}{h}\sqrt{2m\lambda}\right) \tag{2.1}$$

where J represents the tunneling current density, V is the potential difference, e is the electric charge, m is the electron mass, h is Planck's constant, d is the distance between nanofiller, λ is the base potential height, and A is the cross-sectional area of the tunnel. In practice, this implies that small, reversible variations in interparticle distance under strain can induce orders-of-magnitude changes in resistance, enabling gauge factors exceeding 10^3 [171-173]. However, the strong nonlinearity and high dependence on filler dispersion also present challenges for ensuring reproducibility and stability. Overall, the tunneling effect provides a powerful mechanism for achieving ultrahigh sensitivity in nanocomposite strain sensors. Its influence is most pronounced under small deformation regimes or near percolation, where conductive pathways are primarily mediated by tunneling junctions. By tailoring filler type, dispersion state, and matrix interactions, tunneling-dominated composites have been engineered not only for conventional strain sensing but also for advanced high-frequency applications such as acousto-ultrasonic SHM and precision wearable devices [168, 169, 174, 175].

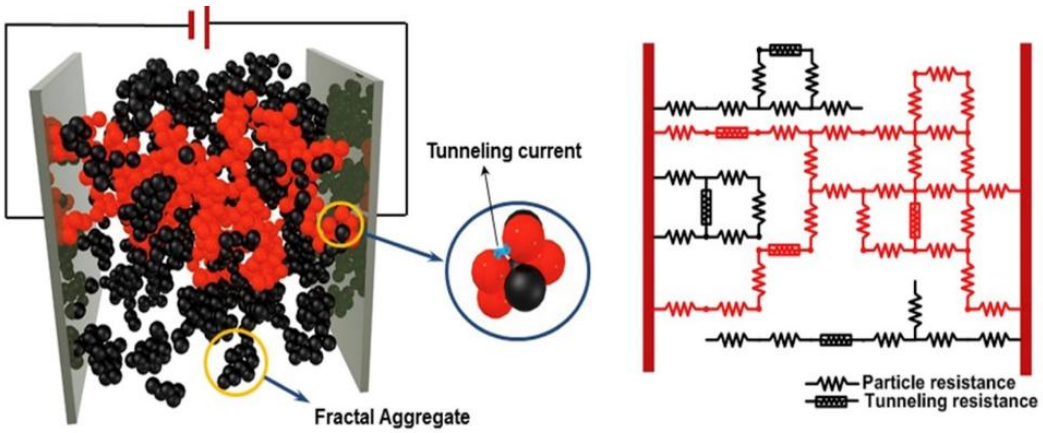

Figure 2.5 Resistor network model of carbon black aggregates [176].

2.5 Applications of Nanocomposite Sensor

2.5.1 Battery Health Monitoring

The rapid commercialization of LIBs has accelerated their deployment in electric vehicles, renewable energy storage systems, and consumer electronics. With this expansion, the service lifetime, safety, and reliability of LIBs have become critical concerns. Mechanical degradation, parasitic side reactions, and electrode–electrolyte instability can lead to irreversible swelling, capacity fade, and safety risks during prolonged cycling [16, 17, 22]. Therefore, embedding sensors that can faithfully monitor the electromechanical response of working batteries offers a powerful strategy for state-of-health (SOH) evaluation and early fault detection. In particular, nanostructured piezoresistive sensors, owing to their high sensitivity, mechanical compliance, and facile integration, have shown strong potential for tracking stress and strain evolution within battery systems.

During charge–discharge cycling, the asynchronous volume changes of the cathode and anode generate stress and strain at the electrode–separator and electrode–current collector interfaces. These mechanical parameters have been demonstrated to correlate strongly with the state of charge (SOC) and SOH of LIBs [177-182]. To capture these signals, two primary sensing strategies have been developed: (i) surface-mounted sensors that measure in-plane stress and strain, and (ii) through-thickness sensors that directly monitor dimensional changes in the z-direction.

Surface-mounted nanostructured sensors are typically laminated or spray-coated onto the exterior of battery cells, enabling real-time tracking of swelling, interfacial stress accumulation, or abnormal mechanical perturbations. For example, CNT-based thin-film strain sensors spray-deposited on PDMS substrates form percolated conductive networks with excellent compliance. When affixed onto the battery surface, the resistance of the CNT/PDMS film increases proportionally with the volumetric swelling of the cell, enabling continuous monitoring of charge–discharge dynamics and abnormal expansions indicative of degradation or thermal runaway risks [183]. Nanocomposite-based sensors have recently been applied to real-time monitoring of lithium-ion batteries [184], addressing both thermal and mechanical safety concerns. MXene composites combined with PEDOT:PSS and PVA have shown high sensitivity and flexibility for temperature detection, enabling continuous thermal tracking during battery operation. Meanwhile, carboxymethyl cellulose (CMC) reinforced with graphene or CNTs and dispersed in PDMS provides strain- and pressure-sensitive

networks, capable of detecting battery swelling and stress evolution. These advances demonstrate the potential of nanocomposite sensors as lightweight, flexible, and multifunctional platforms for improving battery safety and reliability (Figure 2.6).

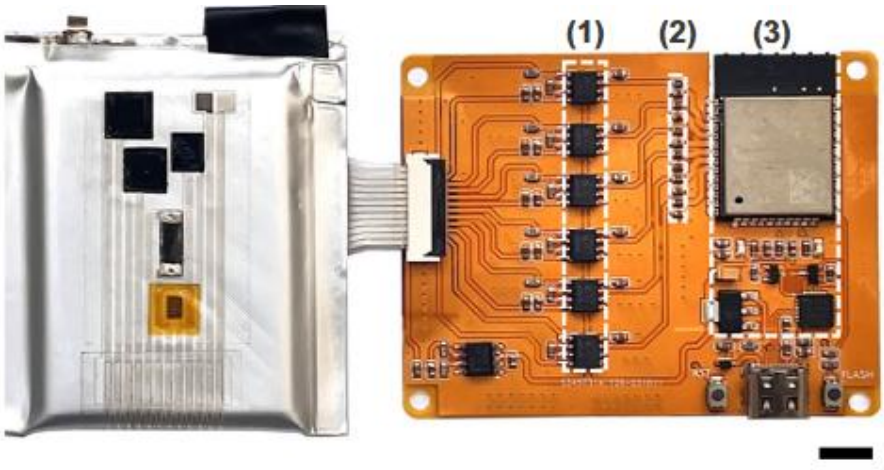

Figure 2.6 Photograph of integrated intelligent lithium-ion battery with nanocomposite sensors and d custom designed printed circuit board [184].

In parallel, thickness-direction monitoring provides a more direct approach to capturing the volumetric breathing of batteries. By measuring dimensional variations along the z-axis, these sensors are capable of resolving nanoscale to microscale changes in electrode thickness during lithiation and delithiation. One representative study employed silver-coated glass microspheres as conductive fillers embedded in an ethylene–vinyl acetate (EVA) copolymer matrix, processed into freestanding conductive microfibers via wet-spinning. Seven such microfibers, each with an active sensing length of ~7.3 mm, were vertically integrated along three sides of a pouch cell to monitor thickness evolution in real time. The two-probe resistance of each microfiber

was simultaneously recorded, revealing sensitive and reversible responses to charge–discharge-induced dimensional variations [23]. As shown in Figure 2.7, this microfiber-based configuration exemplifies how nanostructured sensors can be engineered for scalable, flexible, and high-resolution monitoring of through-thickness battery behavior.

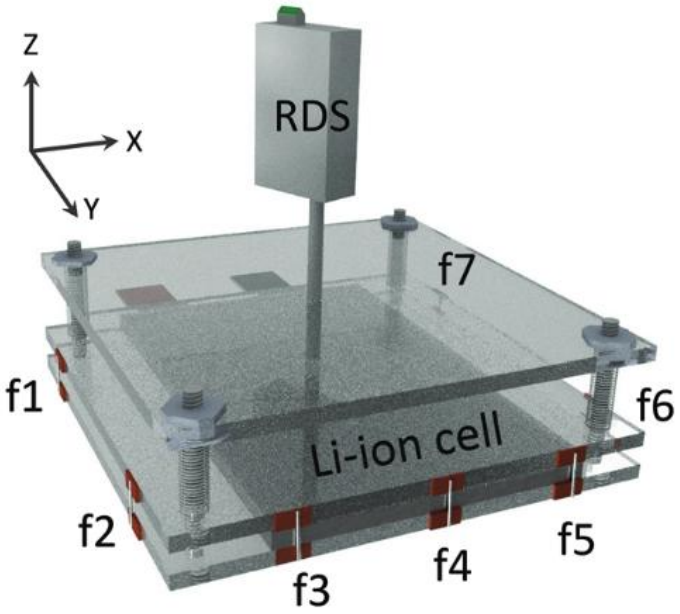

Figure 2.7 Schematic of the setup for battery thickness monitoring of microfiber strain sensors [23].

Overall, nanocomposite sensors offer versatile platforms for battery health monitoring by exploiting their tunable electromechanical transduction mechanisms. Surface-mounted devices excel in detecting in-plane strain and swelling-related anomalies, while through-thickness architectures provide quantitative insights into volumetric expansion. Together, these approaches highlight the promise of nanocomposite-based sensors for real-time, non-invasive monitoring of SOC and SOH, offering new opportunities to enhance the safety, reliability, and lifespan of next-generation lithium-ion batteries.

2.5.2 Wearable Acoustic Sensing

The dynamic performance of nanostructured sensors has been extensively explored in various contexts, with acoustic signal detection being one of the most representative applications. Wearable acoustic sensors have attracted growing interest across a broad range of applications, including voice recognition [42, 185-189], human–machine interfaces [33, 34, 190], and biomedical monitoring [191-196]. Unlike conventional microphones, which rely on air pressure fluctuations, wearable devices can directly capture subtle vibrations on the skin or throat surface. This unique capability provides non-invasive and user-friendly solutions for individuals with speech impairments, offering alternative communication pathways without conventional vocalization. For patients suffering from vocal fold disorders [197], amyotrophic lateral sclerosis (ALS) [198], or laryngeal cancer, such sensors are particularly valuable, as they can decode mechanical vibrations of the throat and convert them into electrical signals for subsequent speech synthesis [36, 37]. In this way, wearable acoustic sensors not only restore the ability of patients to communicate, but also enable access to emergency services and social interaction, thereby significantly improving quality of life.

Driven by this motivation, researchers have developed a variety of material platforms and structural designs to improve the sensitivity, biocompatibility, and wearability of acoustic sensors [42, 185]. Among diverse candidate materials, graphene nanoplates have emerged as a benchmark due to their high conductivity, mechanical compliance,

and intrinsic piezoresistive effect. By directly converting throat-vibration-induced strains into resistance changes, graphene-based wearable sensors provide a straightforward transduction pathway [199-201]. For instance, a laser-induced graphene (LIG) artificial throat was fabricated in a one-step process by converting PI into porous graphene using a 450 nm laser. The device exhibited responsiveness to diverse audio inputs, including environmental sounds such as firecrackers, piano notes, and bird calls [200].

Building on the foundation laid by graphene, MXenes have recently emerged as a new class of 2D transition metal carbides and nitrides for acoustic sensing applications [202-204]. Their high electrical conductivity, tunable surface chemistry, and layered morphology make them attractive for constructing sensitive piezoresistive networks. For example, a MXene/rGO aerogel-based piezoresistive sensor demonstrated the capability to distinguish spoken words when attached to the human throat [203]. Nevertheless, challenges remain, as human voice sensing requires both wide frequency response (0.3–3.4 kHz) and high sensitivity to weak acoustic pressures (<1 Pa) [205]. To address these limitations, an ultrasensitive MXene-based artificial eardrum was designed by integrating double-layer MXene–PDMS–Polyethylene (PE) films (Figure 2.8), in which MXene nanoflakes were uniformly distributed within PDMS micropyramid arrays [196]. This architecture enabled two-stage amplification of acoustic signals: interlayer distance modulation in the MXene sensing film and local pressure enhancement from micropyramid geometry. As a result, the device achieved a

sensitivity of 62 kPa^{-1}, a detection limit as low as 0.1 Pa, and an operational bandwidth of 0.15–3 kHz. These performances not only approach the requirements for human voice detection, but also establish MXene-based systems as promising candidates for next-generation wearable human–machine interaction platforms.

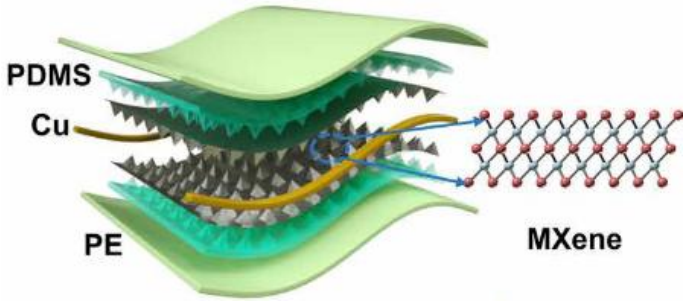

Figure 2.8 Schematic illustration of the MXene eardrum device [196].

2.5.3 High-frequency Ultrasonic Waves Sensing for Structural Health Monitoring

SHM has evolved from traditional non-destructive testing (NDT) into a more advanced paradigm that emphasizes continuous, in situ, and automated surveillance of engineering structures throughout their entire service life. By enabling real-time assessment of structural integrity without the need for disassembly or operational downtime, SHM provides significant benefits, including reduced design redundancy, enhanced in-service safety, extended service life, and decreased maintenance costs across critical fields such as aerospace, civil, and mechanical engineering [166, 206, 207].

Within this context, nanocomposite-based sensors have emerged as an important enabler for advancing SHM technologies. Conventional sensing approaches often suffer from intrinsic limitations, such as insufficient responsiveness to high-frequency vibrations, narrow operational bandwidth, and complex deployment requirements, which restrict their applicability in demanding structural environments. In contrast, nanocomposites overcome these barriers through their unique electromechanical transduction mechanisms. Specifically, their sensing behavior arises from a hybrid mechanism that combines the quantum tunneling effect with the progressive disruption of conductive networks under deformation [208]. At the nanoscale, even minute variations in interparticle distance or network connectivity can induce significant resistance changes, endowing these sensors with exceptional sensitivity (gauge factors in the tens) and ultrawide bandwidth responses that extend from direct current to several megahertz [165].

Such performance characteristics dramatically broaden the functional range of nanocomposite sensors beyond conventional quasi-static loading scenarios (e.g., tensile and bending tests [209]) or low-frequency dynamic measurements (e.g., fatigue monitoring [210]). Importantly, their capability to detect high-frequency, low-magnitude signals allows seamless integration into acousto-ultrasonic SHM approaches [162-164, 211]. In particular, nanocomposite sensors can exploit tunneling effect (Figure 2.10) triggered by guided ultrasonic waves (Figure 2.9), whereby the dynamic strain fields induce nanoscale variations in filler spacing and exponential resistance

changes. This mechanism provides the sensitivity required to identify subtle defects, facilitate early-stage crack detection, and enable reliable long-term monitoring of structural integrity. By leveraging these nanoscale mechanisms, nanocomposite sensors provide a powerful and versatile platform for next-generation SHM, bridging the gap between laboratory-scale sensing demonstrations and practical, in-field structural diagnostics.

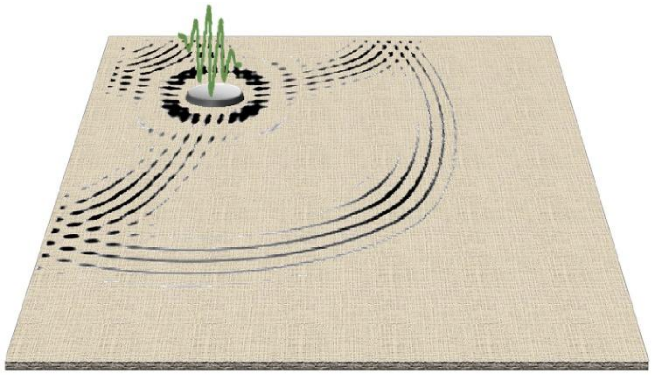

Figure 2.9 GUW excitation and propagation in a composite plate [212].

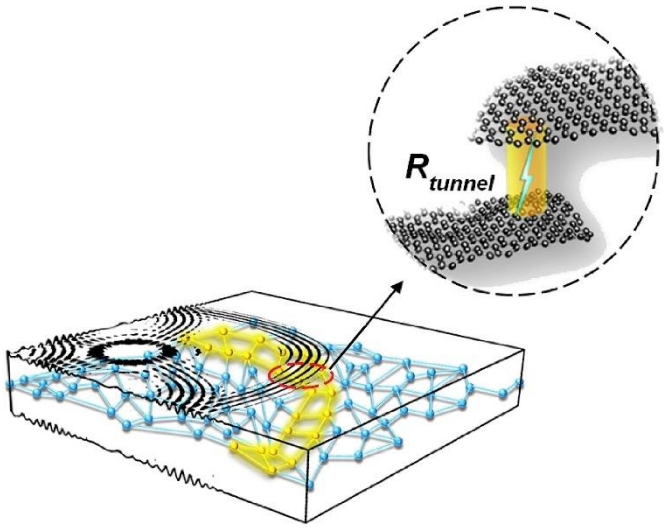

Figure 2.10 GUW-triggered tunneling effect in the nanoparticle-formed percolating

network, leading to change in local electrical resistance [212].

2.6 Summary

In summary, this chapter has outlined the development of nanocomposite sensors from low-dimensional conductive fillers to advanced additive manufacturing techniques that enable precise, scalable fabrication. The sensing mechanisms—ranging from geometric and piezoresistive effects GNP to crack propagation and tunneling—collectively provide broad sensitivity across strain scales, with tunneling-based responses particularly suited for high-frequency acousto-ultrasonic monitoring. Applications in battery health monitoring, wearable devices, and ultrasonic wave sensing demonstrate the versatility of these systems, highlighting their potential to overcome the brittleness and conformability limitations of conventional sensors and to enable reliable SHM in demanding engineering environments.

CHAPTER 3

Dip-coated GNP/PVA Fiber Sensor for Battery Status Evaluation

3.1 Introduction

Highly sensitive sensors integrated into structural batteries enable real-time monitoring of the strain state in the operation period, providing early warnings against thermal runaway and fire hazards in commercial energy storage devices. This study presents an implantable graphene-PVA-coated glass fiber sensor (GP-GFS) fabricated via dip-coating, to detect the internal strains induced by battery cycling and external strains raised by impacts. The sensing performance of the GP-GFS demonstrates an extremely low strain detection limit of 0.009% and 0.028% under tensile and bending strain, and excellent durability of 2000 cycles under tensile strain. Percolation threshold analysis via microstructural and electrical characterization identifies 50 wt% graphene as the critical concentration for optimal conductive network formation. In addition, the GP-GFS is specifically designed for integrating with structural batteries, enabling real-time monitoring of the SOC of batteries, as well as rapid detection of external forces such as impacts. This work establishes a new benchmark for structural battery health monitoring, offering a scalable, cost-effective, and reliable solution for next-generation

energy storage.

3.2 Fabrication of GP-GFS and Functional Structural Battery

Twill-woven glass fiber fabric (Easycomposites® GF-22-200-100) is first separated into individual fiber bundles (diameter: 300 μm, length: 100 mm) that serve as the substrate of the GP-GFS. A graphene ink (10 mg/mL) is prepared by dispersing conductive graphene nanoplatelets (TIME NAN® TNERGO-50) (50 μm in diameter, < 3 layers, and > 95% purity) in ethanol with 1 mg/mL sodium dodecyl sulfate (MACKLIN® SDS) surfactant to enhance dispersion stability. This graphene ink is then mixed with a 10 wt% PVA aqueous solution (ALS New Materials® 205-10%), followed by 2-hour mechanical stirring at 300 rpm and 30-minute ultrasonic homogenization to form an evenly graphene/PVA sensing ink.

Prior to coating, the glass fiber bundles undergo surface modification via 30-minute immersion in 1 wt% γ-aminopropyltriethoxysilane (MACKLIN® KH-550) solution to improve interfacial adhesion [213]. The silanized fibers are dip-coated in the graphene/PVA sensing ink for 3 minutes to ensure uniform coating penetration throughout the fiber bundle, followed by vacuum drying at 50°C for 30 minutes [214], forming the GP-GFS. This fabrication process (Figure 3.1a) enables the production of flexible GP-GFS with a diameter of ~500 μm that demonstrates piezoresistive behavior

while maintaining the inherent flexibility of the pristine fiber.

The GP-GFS is integrated into a four-layer glass fiber-reinforced polymer (GFRP) composites during hand lay-up process for evaluating the sensing performance in the composite structure, as shown in Figure 3.1a. Beginning with twill-woven glass fabric pre-impregnated with epoxy resin (Easycomposites® EP-L2-F-05, 100:30 mass ratio), the GP-GFS is positioned on the second layer of resin-impregnated glass fiber ply. Copper foil electrodes are bonded to both GP-GFS ends using conductive silver epoxy, with copper wires routed to the outside GFRP composites for signal acquisition via a multimeter (Keithley® DMM 7510). Then, GP-GFS is encapsulated with two additional resin-impregnated glass fiber plies, consolidated under vacuum bagging (-30 inHg) to eliminate air voids, and cured at 25°C for 24 hours. Figure 3.1b schematically illustrates the cross-sectional architecture of the hand-lay-up process, depicting the sequential stacking of resin-impregnated glass fiber plies and GP-GFS placement within a vacuum bagging system. The breather layer (Easycomposites® BR180) ensures complete air evacuation from within the vacuum bag and also absorbs excess resin from the laminate during curing. The release film (Easycomposites® R120-P3) facilitates easy demolding of the finished composite structure. Additionally, the sealant tape bonds the vacuum bag to the mold, forming a sealed vacuum chamber that is essential for producing high-quality composite materials with consistent fiber-to-resin ratios and minimal void content. Figure 3.1c shows the final cured GFRP composites with fully integrated GP-GFS after vacuum consolidation and ambient-temperature curing.

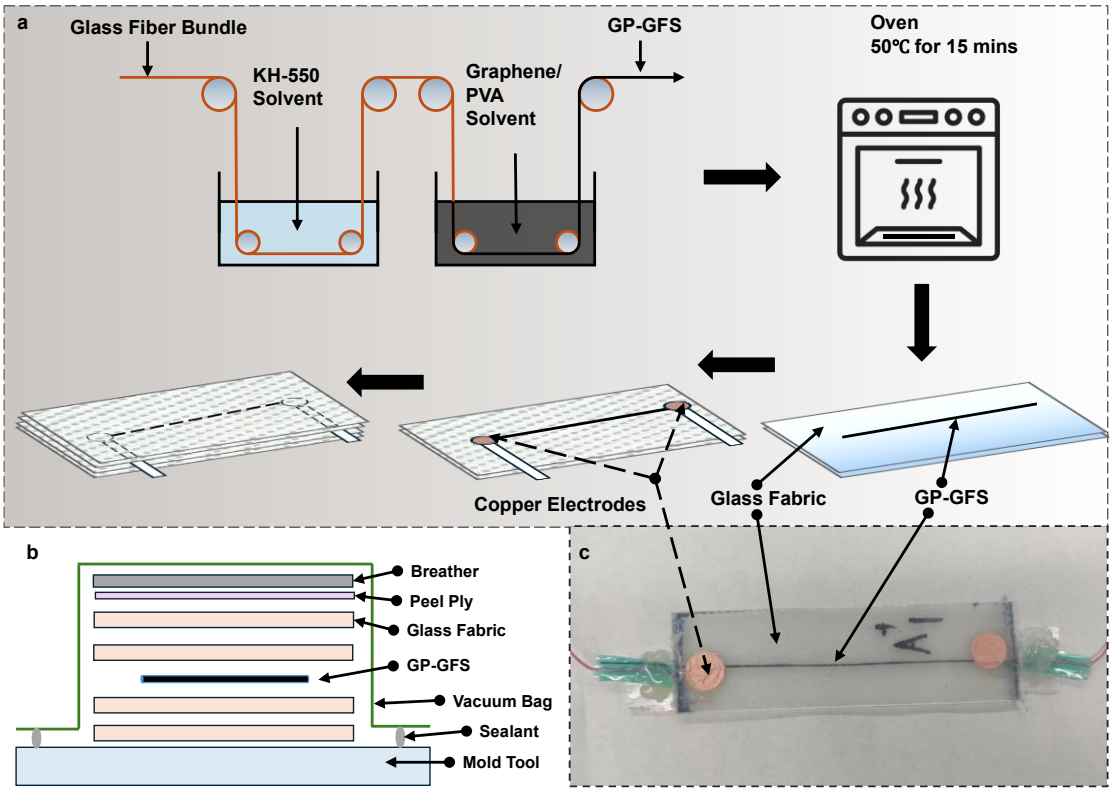

Figure 3.1 a Schematic of sensor dip-coating and embedded into CFRP composites; b the cross-sectional schematic of hand-lay-up; c the picture of final cured GFRP composites with an implantable GP-GFS.

3.3 Characteristics of GP-GFS

To optimize the graphene/PVA ratio for sensing performance, GP-GFS with graphene concentration of 10 wt%, 30 wt%, and 50 wt% are systematically characterized through microstructural, electrical, and crystallographic analyses.

Scanning electron microscopy (SEM, HITACHI® TM4000Plus) reveals distinct microstructural evolution across formulations through both low (Figure 3.2a-c) and high magnification imaging (Figure 3.2d-f) for providing detailed insights into the

graphene distribution and graphene/PVA-glass fiber interfacial characteristics. The GP-GFS with 10 wt% graphene exhibits sparse GNP coverage on glass fiber (Figure 3.2a), with high-magnification imaging revealing that the low graphene content results in GNP being sparsely dispersed within the PVA matrix and only intermittently adhering to the glass fiber (Figure 3.2d). This sparse distribution forms isolated conductive islands that result in near-insulating behavior (conductivity: 4.72×10^5 S/m, see Figure 3.2g). At 30 wt% graphene concentration, localized conductive pathways emerge through GNP overlap (Figure 3.2b), and high-resolution examination shows that graphene and PVA form continuous, gap-free adhesion with the glass fiber, indicating improved interfacial bonding (Figure 3.2e). This microstructure contributes to increased conductivity to 9.42×10^5 S/m, as demonstrated in the relationship between conductivity and graphene concentration (Figure 3.2g). The 50 wt% formulation achieves a percolation threshold transition, characterized by continuous conductive networks with densely interlocked GNPs (Figure 3.2c), which yields a conductivity of 6.37×10^6 S/m (Figure 3.2g). Notably, high-magnification SEM (Figure 3.2f) reveals that the GNPs appear to integrate seamlessly with the glass fiber, showing no distinct interfacial boundaries and achieving nearly complete fiber coverage. Beyond 50 wt%, conductivity plateaus with minimal gains, confirming saturation of the conductive network. This abrupt transition at 50 wt% graphene loading aligns with classical percolation theory, where the critical filler concentration marks the onset of bulk conductivity through interconnected pathways.

The X-ray diffraction (Xrd, Bruker® D8 Venture, Cu Kα) patterns of the graphene/PVA nanocomposites reveal two distinct diffraction features (in Figure 3.2h), confirming the coexistence and structural interplay of both components. A sharp, high-intensity peak at ~26.0° corresponds to the (002) crystallographic plane of graphene, indicating well-ordered stacking of GNPs with an interlayer spacing of 0.34 nm, a critical factor for maintaining electrical conductivity. A broad amorphous halo centered at 19.5° arises from the PVA, characteristic of its disordered polymer chains. As the PVA-to-graphene ratio decreases (e.g., from 10 wt% to 50 wt% graphene), the intensity of the 19.5° peak diminishes progressively, reflecting the reduced volumetric contribution of the polymer phase. This inverse correlation validates the compositional controllability of the graphene/PVA nanocomposites.

The mechanical properties of the GP-GFS are studied by an external uniaxial tensile strain, and the results of the GP-GFS compared with the pristine fiber are shown in Figure 3.2i. The GP-GFS achieves a 73.7% increase in tensile strength (989.0 ± 184.8 MPa *vs.* 569.5 ± 14.9 MPa for pristine glass fiber) alongside a 9.6% increase in Young's modulus (25.1 ± 5.3 GPa *vs.* 22.9 ± 0.3 GPa for pristine glass fiber). This simultaneous strengthening and stiffening effect originate from the synergistic interaction between the PVA/graphene and glass fiber. The PVA/graphene infiltrates interfacial gaps between individual fiber, promoting robust interfacial bonding and consolidating the fiber bundle into a unified load-bearing network [215-218]. Under external loading, the composite matrix acts as a stress-redistribution bridge,

homogenizing applied forces across the fiber bundle, thereby elevating both strength and stiffness.

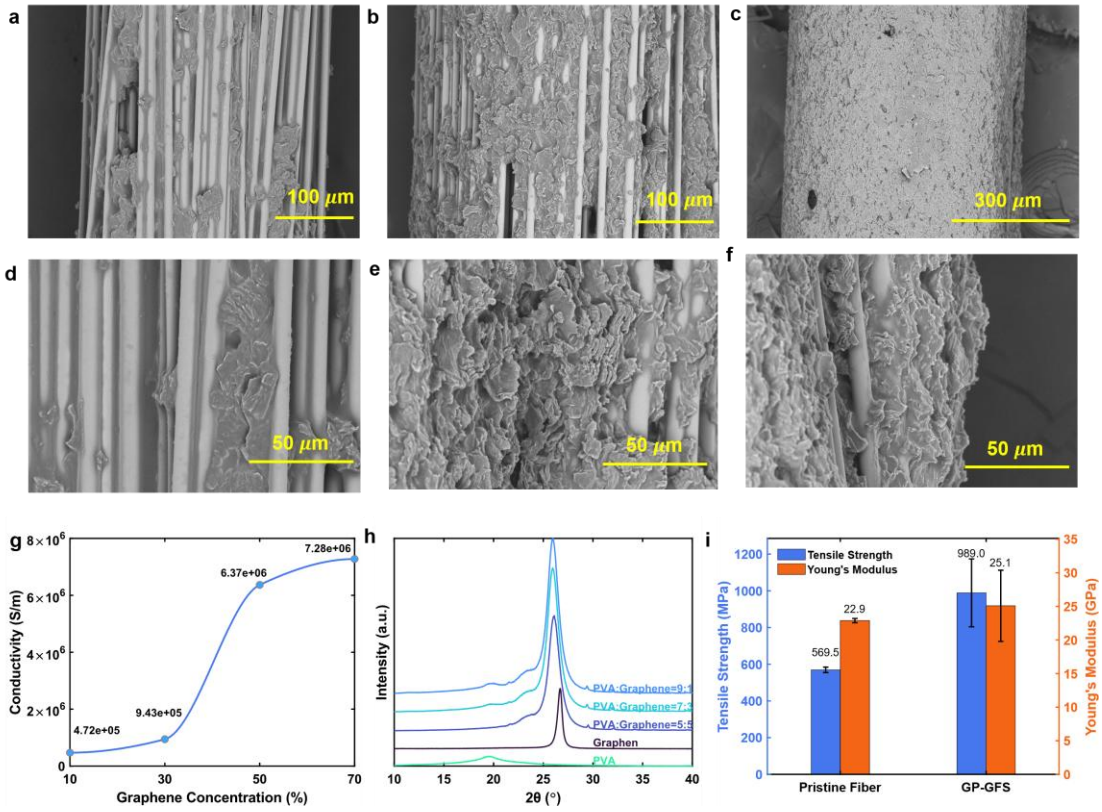

Figure 3.2 Characterizations of GP-GFS. a-c Low-magnification SEM images of GP-GFS with different graphene concentrations of 10% (a), 30% (b), and 50% (c); d-f High-magnification SEM images of GP-GFS with graphene concentrations of 10% (d), 30% (e), and 50% (f); g conductivity of GP-GFS at concentration range from 10% to 70%; h Xrd of GP-GFS with different graphene concentration of 10%, 30%, and 50%; i mechanical properties of pristine fiber and GP-GFS with graphene concentration of 50%.

3.4 Sensing Performances

3.4.1 Sensing Performance under Tensile Strain

The sensing performance of the GP-GFS is first evaluated under tensile loading to

establish the fundamental sensing mechanism and baseline electromechanical properties, which serve as the foundation for understanding the sensing behavior of GP-GFS under more complex loading conditions such as bending and impact scenarios. A 100 mm-long GP-GFS is embedded in the second ply of a four-layer GFRP composites (250×25 mm) and subjected to uniaxial tensile via a universal testing machine (ZwickRoell® Z250), as illustrated in Figure 3.3a. Resistance changes are recorded in real-time using a two-probe digital multimeter synchronized with mechanical loading.

Under quasi-static tensile loading at 2 mm/min, the GP-GFS exhibits a near-linear correlation between applied tensile strain and relative resistance change, as shown in Figure 3.3b. The strain sensitivity under tensile strain is quantified by the gauge factor (GF_t):

$$GF_t = \frac{\frac{\Delta R}{R_0}}{\varepsilon_t} \tag{3.1}$$

where ΔR is the change in the electrical resistance, R_0 is the initial electrical resistance, $\frac{\Delta R}{R_0}$ is the relative electrical resistance, and ε_t is the tensile strain. The sensitivity at tensile load reaches ~8.6 across the strain range from 0.01 to 0.025. This piezoresistive behavior arises from strain-induced separation of adjacent GNPs, which disrupts the percolative conductive network, thereby elevating the relative resistance.

The GP-GFS exhibits remarkable strain discrimination capability even at low strain levels. As illustrated in Figure 3.3c, the GP-GFS demonstrates real-time response to

three distinct tensile strain levels (0.070%, 0.183%, and 0.304%). The results clearly indicate that the GP-GFS can precise track not only the loading and unloading cycles at 0.304% strain but also at the minimal strain level of 0.070%, while resolving the incremental strain variations as small as 0.113% (from 0.070% to 0.183%), highlighting its capability for high-fidelity strain monitoring. Furthermore, investigation of the detection limit of GP-GFS reveals an impressive minimum detectable tensile strain of 0.009%, while maintaining excellent stability and reproducibility under multiple loading-unloading cycles (Figure 3.3d). This high sensitivity to fine tensile strains is particularly valuable when the GP-GFS is integrated into structural batteries or multifunctional composites, where it enables real-time monitoring of tensile stress variations in aerospace composite structures [219, 220] or automotive body panels [221, 222] during normal operation, mechanical loading, or dynamic conditions such as inertial tensile forces during vehicle acceleration.

Complementing its exceptional sensitivity and rapid response characteristics, the GP-GFS demonstrates validated through 2,000 cycles under strain of 0.067% at a frequency of 1 Hz. Figure 3.3e depicts that GP-GFS maintains 98.5% initial sensitivity after 100 cycles and shows no further degradation up to 2,000 cycles. This stability stems from the elastic recovery of the graphene-PVA nanocomposite, which prevents permanent conductive network damage under cyclic loading.

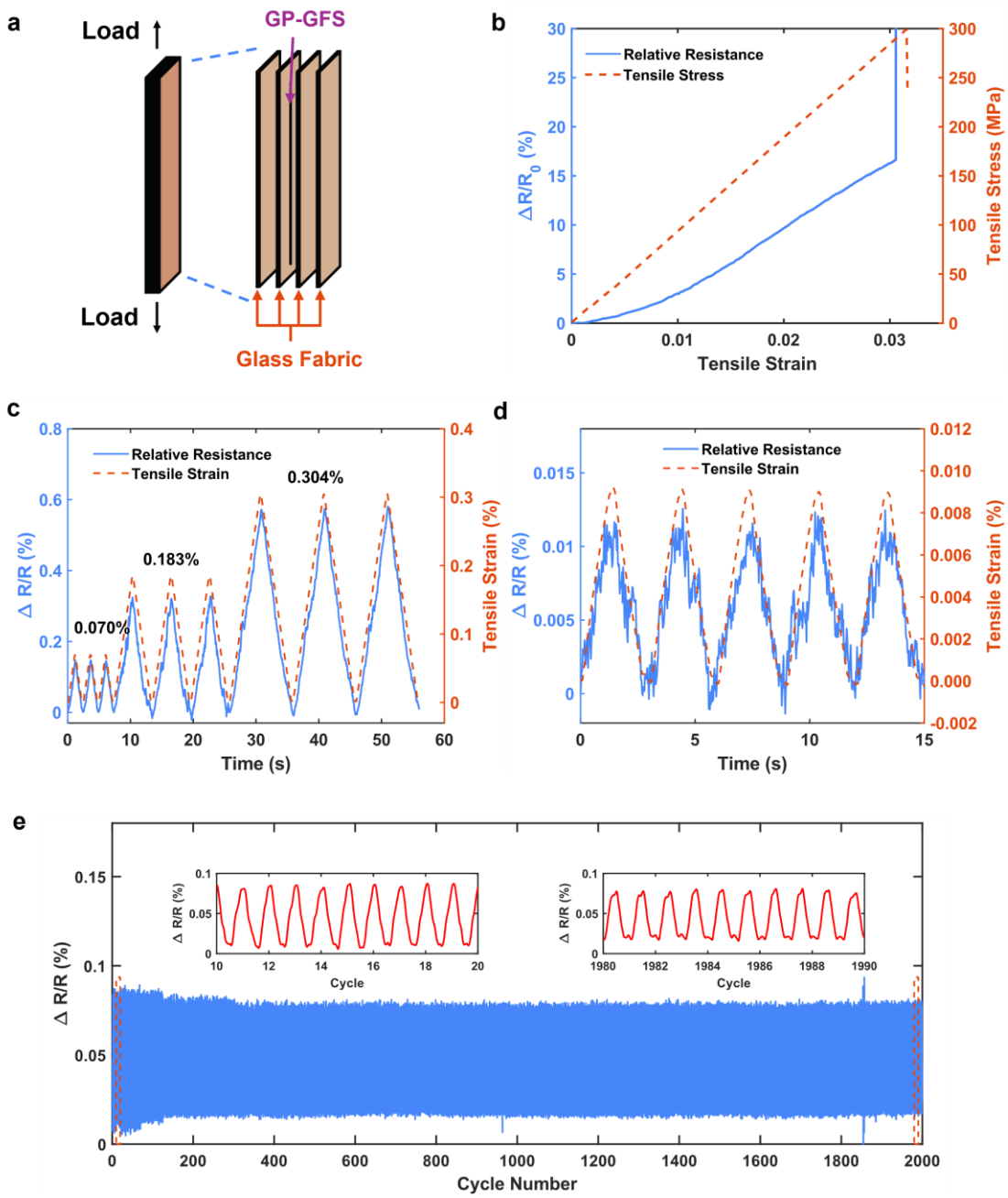

Figure 3.3 Sensing performance of the GFRP composites with GP-GFS under tensile strains. a Schematic diagram of testing the sensing performance of the GFRP composites with GP-GFS under tensile; b Stress/relative resistance change *vs.* tensile strain; c the relative resistance change under cyclic tensile test with the maximum strain of 0.070%, 0.183%, 0.304%; d relative resistance change under a cyclic tensile strain of 0.009% showing the minimum detection limit of the GP-GFS; e durability of the GP-GFS response 2000 cyclic tensile strain of 0.067%, and insets show the enlarged GP-GFS responses at two temporal windows of 10 to 20th cycles (left), and 1980 to 1990th

cycles (right).

3.4.2 Sensing Performance under Three-point Bending

Having established the high sensitivity and durability of GP-GFS under uniaxial tensile loading, structural batteries in practical applications frequently experience complex loading conditions including bending deformations. To comprehensively evaluate the versatility of the GP-GFS under bending strain states, we further investigated its electromechanical response under three-point bending conditions, which introduce more complex strain distributions combining both tensile and compressive components through the composite thickness.

GP-GFS is embedded centrally within the second ply of a four-layer GFRP composites (35 mm×100 mm, sensor length: 80 mm) to evaluate its electromechanical response under three-point bending (Figure 3.4a). Quasi-static three-point bending tests are performed using a universal testing machine (ZwickRoell® Z5.0) at a crosshead speed of 1 mm/min, with a span length L=25.4mm (ASTM D7264/D7264M-21). The flexural strain (ε_f) and stress (σ_f) are calculated as:

$$\varepsilon_b = \frac{6h_0\delta}{L^2} \tag{3.2}$$

$$\sigma_f = \frac{3FL}{2bh_0} \tag{3.3}$$

where h_0 =0.8 mm (thickness of GFRP composites), b =35 (width of GFRP composites), δ (midspan deflection), and F is applied load. The gauge factor under

flexural strain (GF_f) is defined as:

$$GF_f = \frac{\frac{\Delta R}{R_0}}{\varepsilon_f} \tag{3.4}$$

where ΔR is the change in the electrical resistance, R_0 is the initial electrical resistance, $\frac{\Delta R}{R_0}$ is the relative electrical resistance, and ε_f is the flexural strain.

As shown in Figure 3.4b, the three-point bending test subjects the sample to progressively increasing load until catastrophic failure occurs. As flexural stress increases, the embedded GP-GFS exhibits a corresponding rise in relative resistance change that follows a consistent trend. A sharp surge in relative resistance occurs at the critical fracture point of the GFRP composites, due to the rupture of the percolative graphene network under fracture strain, which irreversibly destroys the electron transport. When the flexural strain is below 0.01, the GP-GFS shows a near-linear response with a gauge factor (GF_f) of 0.2, significantly lower than observed under tensile loading. This reduced sensitivity in flexural strain originates from the neutral plane effect in bending deformation: as the GP-GFS is embedded in the midplane of GFRP composites, it experiences minimal strain during small deflections, where bending-induced compressive and tensile strains on opposing surfaces largely cancel at the neutral axis.

The underlying sensing mechanism is governed by the conductive network built by

graphene flakes within the PVA matrix. Under bending deformation, the GP-GFS experiences asymmetric strain distribution—compression on one side and tension on the opposite. In regions subjected to compressive forces, graphene flakes undergo enhanced aggregation and tighter overlapping, locally intensifying conductive paths. Conversely, areas experiencing tensile deformation exhibit increased separation between adjacent graphene flakes, disrupting electron transport networks, as illustration in the Figure 3.4c. This reconfiguration of the conductive paths modulates the overall electrical resistance of the GP-GFS, enabling precise detection of flexural strain variations through corresponding electrical signal modulations.

To further evaluate the real-time flexural strain discrimination capability, cyclic bending tests are conducted at a strain rate of 0.005% s^{-1} with strain amplitudes of 0.085%, 0.134%, and 0.260% (in Figure 3.4d). Similar to tensile performance, the relative resistance changes exhibit high-fidelity tracking of the applied flexural strains, accurately replicating both the magnitude and phase of each deformation cycle. Notably, the GP-GFS resolved distinct strain levels with a precision of 0.049%, demonstrating clear differentiation between the three tested flexural strain amplitudes. Further investigation of the detection limit of GP-GFS reveals a minimum detectable dynamic flexural strain of 0.028% (in Figure 3.4e), demonstrating ultrahigh sensitivity to microscale deformations.

The GP-GFS exhibits exceptional sensitivity under both tensile and bending loading

modes, with particular proficiency in detecting minute strain variations. This exceptional ability to monitor microstrains enables precise tracking of subtle deformations induced by lithium-ion (Li-ion) intercalation/deintercalation dynamics during electrochemical cycling. Furthermore, the superior dynamic response characteristics and remarkable durability of GP-GFS facilitate rapid detection of transient external mechanical stimuli while maintaining consistent performance over extended operational periods.

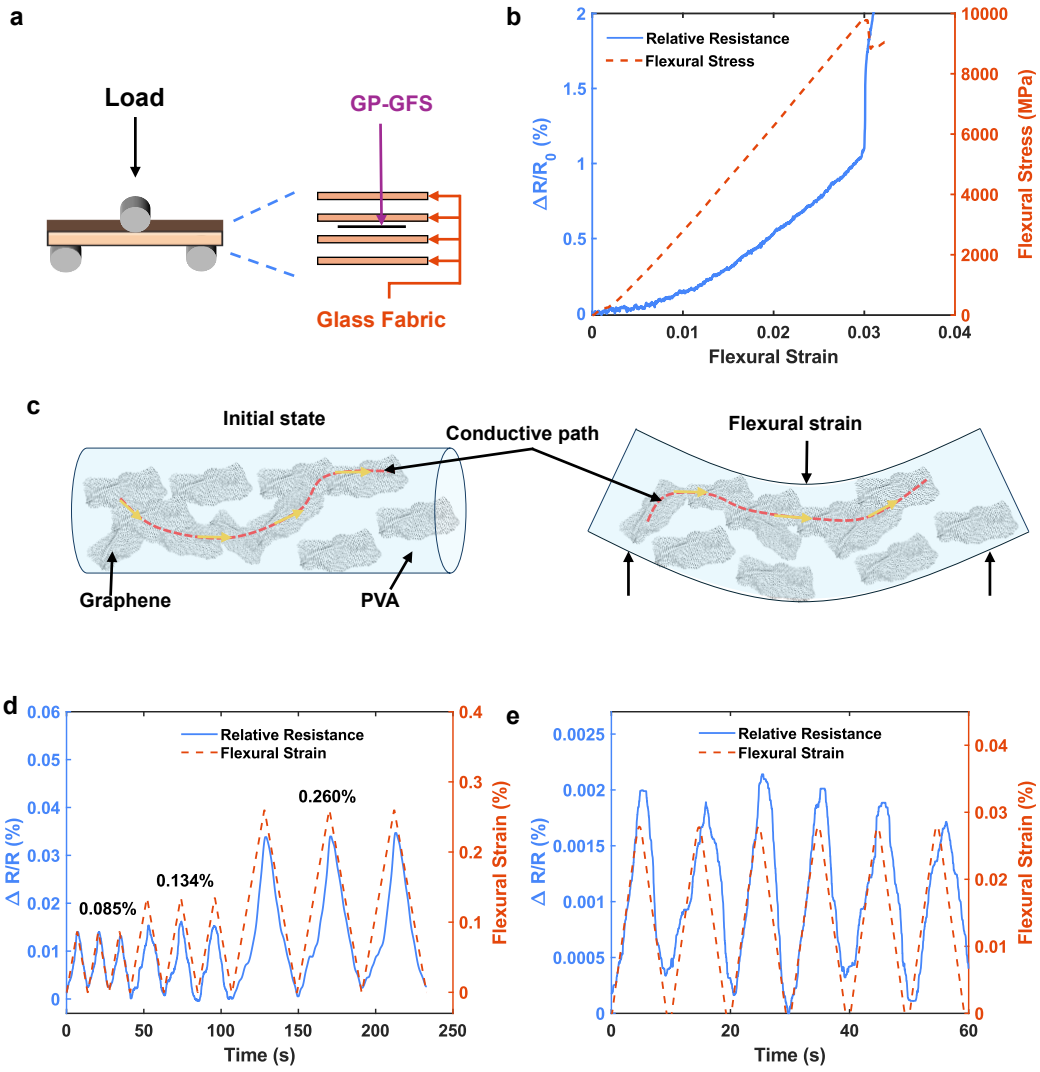

Figure 3.4 Sensing performance of the GFRP composites with GP-GFS under three-point bending. a Schematic diagram of testing the sensing performance of the GFRP composites with GP-GFS under three-point bending; b stress/relative resistance change

vs. flexural strain; c schematic illustration of the conductive path of GP-GFS at initial state and flexural strain; d the relative resistance change under cyclic flexural strain with the maximum strain of 0.085%, 0.134%, 0.260%; e relative resistance change under a cyclic flexural strain of 0.028% showing the minimum detection limit of the GP-GFS.

3.5 Monitoring the Status of Structural Battery

3.5.1 Monitoring Internal Strain of Structural Battery

Leveraging these advantageous properties, we have successfully integrated the GP-GFS with structural battery components to develop an intelligent structural battery capable of simultaneously monitoring both internal electrochemical-induced strains and external mechanical deformations in real time, thereby enhancing both safety and reliability.

The fabrication process of intelligent structural battery integration is illustrated in Figure 3.5a. The commercial Li-ion pouch cell (Yidian Tech® YD 042255, capacity: 24 mAh, dimension: 55.5 mm×22.5 mm×0.45 mm) is first embedded between the second and third glass fiber plies, and the GP-GFS is then aligned on the third glass fiber ply using the same electrode bonding and wiring protocol, separated by a resin-coated glass fabric isolation layer to prevent pouch cell electrode from contacting the GP-GFS. The final glass fiber ply encapsulates the GP-GFS, followed by vacuum consolidation and ambient curing. Figure 3.5b depicts a schematic of the multilayer intelligent structural batteries, detailing the hierarchical integration of the Li-ion pouch

cell, glass fabric, and embedded GP-GFS, with Figure 3.5c providing a photographic representation of the fully encapsulated prototype.

During Li-ion pouch cell operation, the charging and discharging processes are accompanied by reversible swelling behavior in the direction perpendicular to the pouch surface which is due to Li-ion intercalation/deintercalation [223, 224]. The pouch cell is operated using established protocols for constant current and constant voltage (CC-CV) charging and constant current (CC) discharging processe in a battery test equipment (NEWARE® CT/CE-4000) with a constant temperature charmer (25°C). Figure 3.5d depicts four representative charge-discharge cycles of the voltage of the pouch cell (0.5 C rate) and the corresponding relative resistance change of the GP-GFS. During CC charging from 3.1 V to 4.2 V, rapid Li-ion intercalation into the anode induces progressive battery swelling [31], generating increasing internal strain. The GP-GFS effectively captures this rising internal strain, manifested as an increase in relative resistance. During the subsequent constant-voltage (CV) charging phase at 4.2V, Li-ion undergoes gradual redistribution and complete intercalation throughout the electrode structure [225, 226]. At this time, the strain increases very slowly and gradually stabilizes, yielding minimal relative resistance change. The CC discharge from 4.2 V to 3.1 V triggers Li-ion progressively deintercalation and anode contraction, followed by accelerated voltage drop, strain recovery, and the relative resistance of the GP-GFS decreases accordingly. The results demonstrate that GP-GFS enables real-time assessment of SOC in structural batteries by correlating Li-ion intercalation dynamics

with mechanical strain evolution.

Further, the GP-GFS shows the capability for monitoring SOC across varied C-rates (0.5 C, 1 C, 1.5 C), as evidenced by its proportional relative resistance changes in Figure 3.5e. At 0.5 C, the relative resistance changes manifest a characteristic transient plateau during the mid-charge/discharge regime, directly corresponding to the minimal volumetric fluctuation associated with the phase transition of the graphite anode from LiC_{18} to LiC_{12} [31, 227-229]. During this transitional stage, the cell voltage progressively increases while mechanical strain remains consistent, reflecting the uniform Li-ion intercalation process. When subjected to elevated charge/discharge rates (1 C and 1.5 C), the plateau region exhibits significant attenuation, indicating the acceleration of side reactions [31, 229].

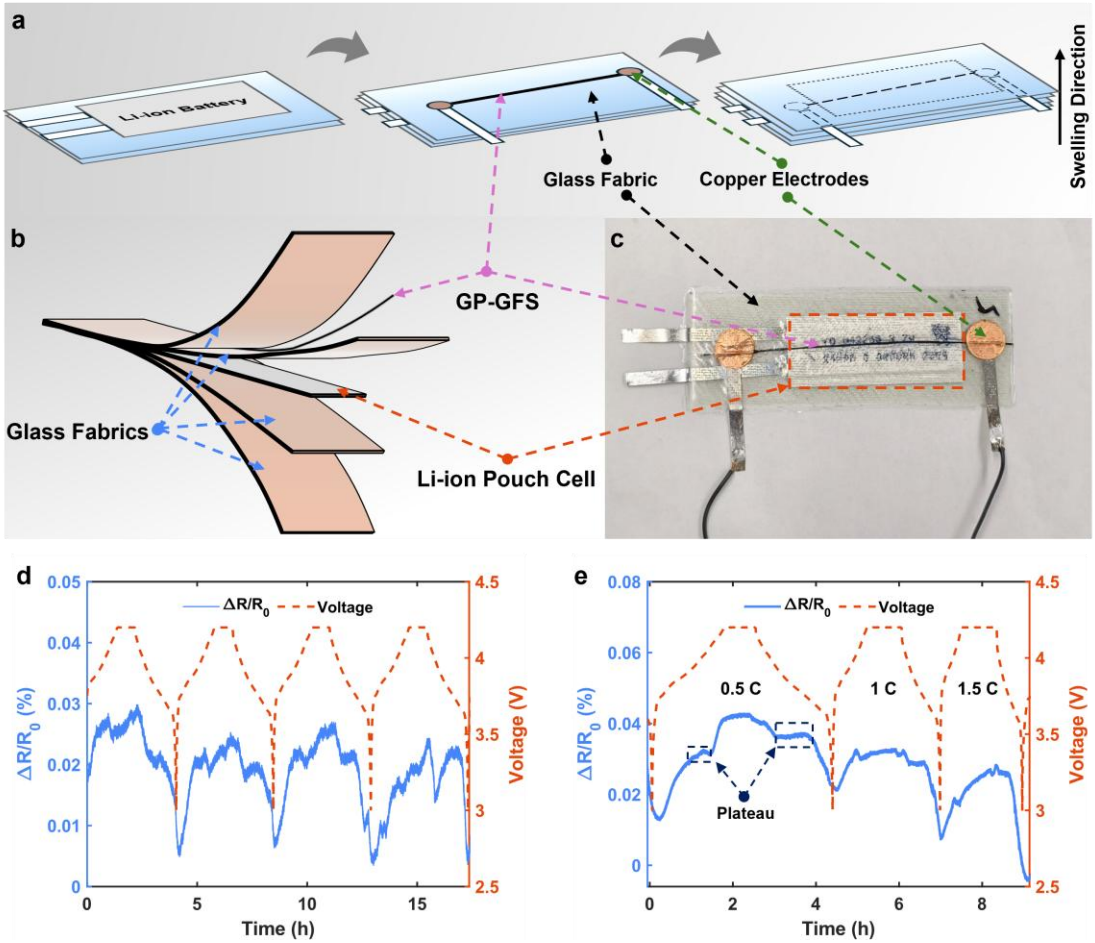

Figure 3.5 The intelligent structural battery for monitoring internal strain. a Preparation flowchart of the intelligent structure battery; b schematic of the multilayer intelligent structural batteries; c photographic of the prototype; d relative resistance response of the GP-GFS during four successive charge–discharge cycles, and the cell voltage-versus-time plot during the same cycles; e relative resistance response of the GP-GFS under different cell C-rates.

3.5.2 Monitoring External Impact of Structural Battery

The GP-GFS exhibits versatility beyond monitoring internal electrochemical-induced strain, demonstrating capability for rapid detection of external mechanical impacts—a critical safety feature for structural batteries deployed in dynamic operational environments. To simulate realistic collision scenarios, a custom-built impact platform

is employed to deliver controlled strikes with an energy of approximately 0.06 J to the intelligent structural battery during seven consecutive charge-discharge cycles at 0.5 C (Figure 3.6a). Owing to the limitations of the available data acquisition system (Keithley® DMM 7510, Sampling rate of 40 Hz), it is technically challenging to maintain both high sampling rates and continuous long-duration data logging simultaneously; consequently, priority is given to monitoring the electrochemical cycling of the battery. Despite the sampling rate limitation, which prevents full reconstruction of the high-frequency impact waveform, the GP-GFS still reliably signals external impact events through sudden resistance spikes, providing an effective early-warning capability. In the initial cycles, the baseline resistance remained stable; however, from cycle 3 onward, a slight upward drift emerged due to cumulative damage to the conductive network under repeated mechanical compression from battery expansion. Importantly, even with this minor drift, the GP-GFS produced clear, instantaneous spikes at each impact (applied during cycles 1, 5, and 7; Figure 3.6b–d), precisely indicating the timing of mechanical impacts. This advanced performance stands in stark contrast to conventional battery management systems (BMS), which are fundamentally insensitive to non-electrochemical perturbations and thus unable to detect such mechanical perturbations. The applied hammer strikes generate localized strains that temporarily disrupt the graphene-PVA conductive network, resulting in significant resistance surges. By providing real-time alerts to collision-induced structural compromises such as composite microcracks or interfacial delamination, the intelligent structural batteries effectively prevent the progression of latent failure that

could potentially escalate into catastrophic thermal runaway events.

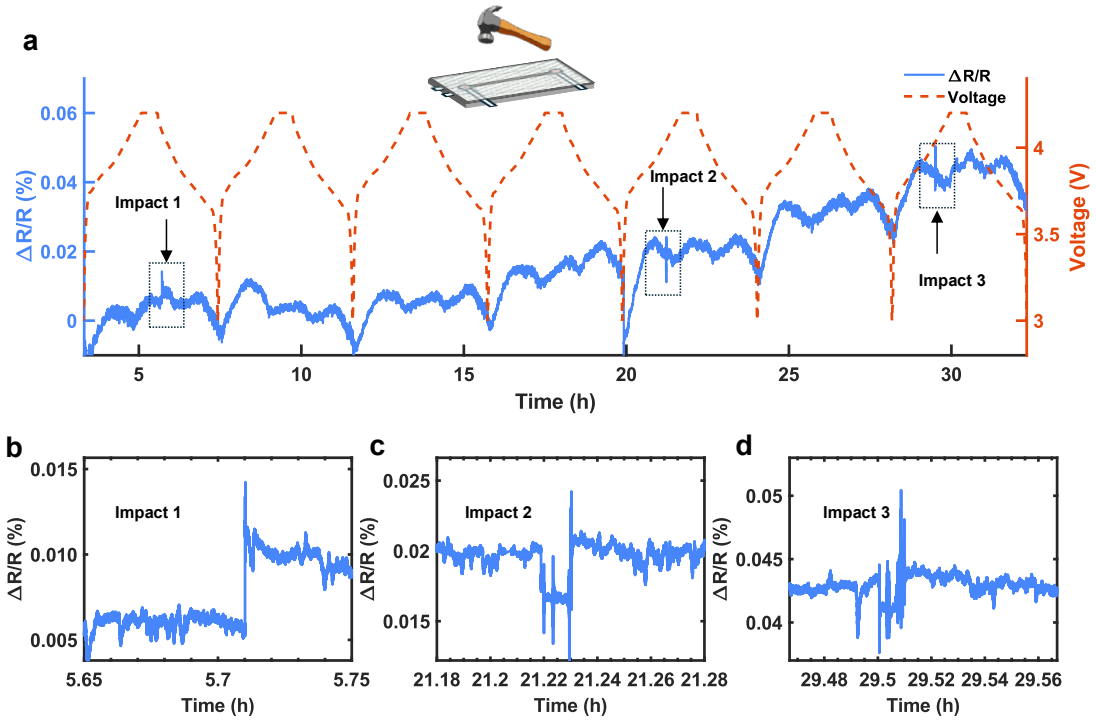

Figure 3.6 The intelligent structural battery for monitoring external strain. a Response of an intelligent structural battery with embedded GP-GFS to external impacts during operation; b-d enlarged image of the relative resistance change of the GP-GFS under three different impacts.

3.6 Summary

This study presents an implantable, ultrasensitive GP-GFS fabricated via dip-coating for monitoring the state of structural batteries. The GP-GFS achieves exceptional sensing performances, including a minimum detectable tensile and flexural strain of 0.009% and 0.028%, while maintaining 98.5% sensitivity retention over 2,000 mechanical cycles. At 50 wt% graphene concentration, the GP-GFS reaches its

percolation threshold, marked by the formation of continuous conductive networks and conductivity of 6.37×10^6 S/m. By embedding the GP-GFS within a GFRP composites-encapsulated Li-ion pouch cell, GP-GFS effectively monitors internal strains generated during charge-discharge processes even in multiple C-rates (0.5 C-1.5 C), facilitating accurate SOC estimation based on mechanical deformation. During external impact simulations, the GP-GFS captures transient mechanical perturbations undetectable by voltage-based BMS, demonstrating its unique capacity to identify collision-induced risks such as microcracks or delamination. Although current data acquisition system limitations prevent simultaneous high-frequency sampling and long-duration monitoring, making complete restoration of external impact signals challenging, the timing of impacts can still be reliably determined through sudden resistance variations. The GP-GFS provides critical early warning indicators for potential failure modes ranging from abnormal lithiation processes to impact-induced structural damage in demanding environments. This limitation can be addressed in future work through a dual acquisition approach: implementing a low-sampling-rate system for continuous battery cycling monitoring alongside a high-sampling-rate system for transient impact detection, with synchronized timing to enable correlation of impact events with specific electrochemical states.

CHAPTER 4

Stencil Printed Non-intrusive Graphene/epoxy Sensor for Structural Health Monitoring

4.1 Introduction

GFRP composites degrade continuously through service, entailing effective health monitoring to ensure structural integrity. In this chapter, a new type of GFRP structure, with the embedded non-intrusive sensors for *in situ* SHM, is developed. Piezoresistive nanocomposite sensors – a pre-cured hybrid of GNP and epoxy, are printed in the second lamina of GFRP prepreg with epoxy matrix during lay-up to laminate process and then co-cured with GFRP composite, keeping the continuity at the interface between the composite. The GNP/epoxy sensor successfully captures the structural response from static strain to a high frequency ultrasonic wave up to 600 kHz with a gauge factor up to 26, which is the first ever nonintrusive GNP/epoxy piezoresistive sensor with an ultra-wide frequency response to mechanical deformation. Furthermore, the mechanical properties of host composite show negligible signs of intrusion testified with tensile and bending tests. GFRP with embedded sensor features merits of high strength from GFRP as well as high-sensitivity sensing capability from the nanocomposite sensors, opening up a new avenue to *in situ* health monitoring of

composites.

4.2 Preparation of GNP/epoxy Sensor

A sensor material preparation procedure is proposed to minimize nanofiller agglomeration and suppress the generation of void. Graphene (diameter: 50 μm, layers: < 3, and purity: > 95%) was supplied by TIME NANO Chengdu. Epoxy resin (Buehler® EpoKwick FC) is provided by BUEHLER USA. The fabrication procedure of GFRP composites with the embedded GNP/epoxy sensor is shown in Figure 4.1. A total of 0.06 g of graphene nanofiller is dispersed in 4 g epoxy and then added to 4 ml acetone (purity: > 99.9%) to form a homogeneous dispersion using a magnetic stirrer at 25°C with 400 rpm for 20 hours. Then, the mixture is sonicated in an ultrasonic bath for 30 mins, followed by acetone evaporation in a vacuum oven under -25 inHg at 80°C for 3 hours. After the acetone is completely evaporated, the hardener is added into graphene/epoxy using mechanical stirring for 5 mins, and then placed in the oven at a pressure of -25 inHg at 25°C for 30 mins for degassing.

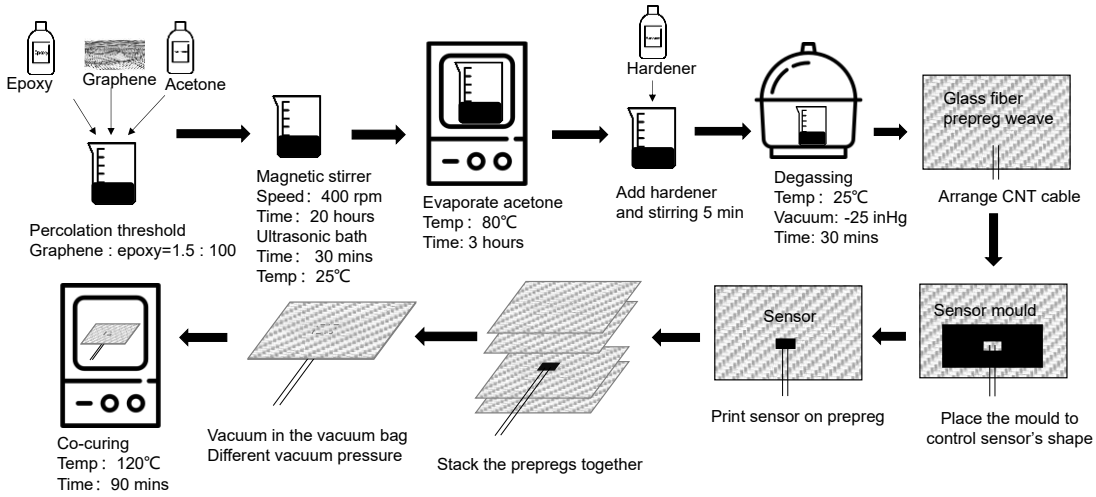

Figure 4.1 Flowchart of GNP/epoxy sensor and composite with sensor fabrication.

4.3 Fabrication of Sensors and GFRP Composites

Plain weave glass fiber prepregs with 38 wt% epoxy resin for GFRP composite are supplied by the Easycomposites UK. An electrical connection made of a CNT fiber is purchased from TIME NANO. The glass plate is used as the baseplate, on all sides of which the release agent is coated and the sealant tape was pasted. The GFRP laminate consists of 4 layers of glass plain weave prepreg which is cut to the shape of the sample by a prepreg cutting machine (AOL® AOL-1313), and stacked on the baseplate. Then two CNT fibers as the connection wire are arranged in precise locations on the second glass fiber prepreg ply and the electrode distance between the two CNT fibers of each sensor was controlled at 1 mm. After that, the sensors with 1.5 wt% (closing to the percolation threshold [9]) of graphene in the nanocomposite solution are printed at a specific position where the CNT fibers were fixed, and the initial thickness and shape of the sensor are controlled with a mold. After the sensor fills the mold, the mold is peeled off, followed by the stack of the remaining two prepreg plies. At last, the pill film, breather, and vacuum bag are placed in sequence on the top of the prepreg plies, as shown in Figure 4.2.

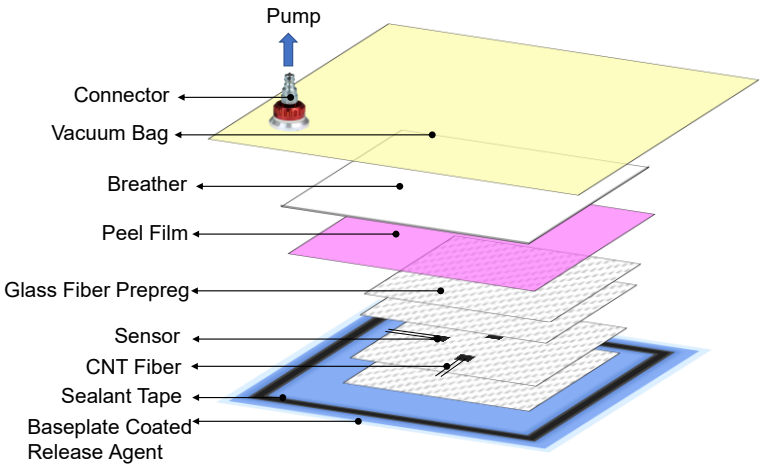

Figure 4.2 The fabrication schematic of GFRP with embedded GNP/epoxy sensor.

After the above steps, sensors and prepregs were co-cured at 120°C for 90 mins. To study the effect of co-curing fabrication pressure on the sensitivity of the sensor, GFRP composites with graphene/epoxy sensor and CNT fibers were fabricated at -15 inHg, -20 inHg, -25 inHg, and -30 inHg, namely GEP-15, GEP-20, GEP-25, and GEP-30, respectively. Note that -30 inHg equals the standard atmospheric pressure, which is the maximum pressure that can be reached with the vacuum bag. The GFRPs with the embedded GNP/epoxy sensor fabricated at these four pressures are displayed in Figure 4.3, showing different final shapes of this sensor. The spread of the embedded sensor to the nearby area increases as the pressure increases. Further, the fabrication pressure also influences the initial resistance and thickness of the embedded GNP/epoxy sensor. The average resistance of the embedded GNP/epoxy sensor fabricated at -15, -20, -25 and -30 inHg are approximately 800 KΩ, 1 MΩ, 3 MΩ and out of the measurement range of the multimeter (> 1 GΩ), respectively. And the thicknesses of the sensors are 105 μm, 76 μm, 62 μm, and 40 μm at -15, -20, -25 and -30 inHg, respectively, making

the thickness of GEP-15, GEP-20, GEP-25 and GEP-30 0.9 mm, 0.89mm, 0.89 mm and 0.88 mm, respectively.

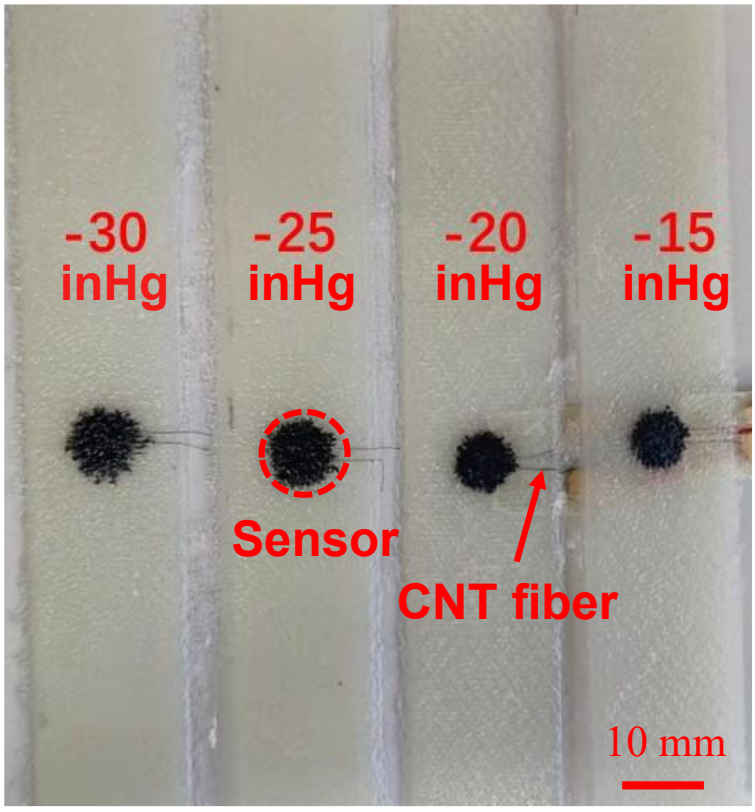

Figure 4.3 The embedded sensor profile at different fabrication pressures.

4.4 Morphological Characterization

In order to explore the morphology of GFRP with GNP/epoxy sensors, two key factors need to be precisely observed, one is the graphene dispersion which determines whether the sensor has a strong sensing capability, and the other is the bonding condition that affects the mechanical performance of the composite.

Before observing on a SEM platform (FEI® Nova NanoSem450), the cross-section of

the sample was first polished by a semi-automatic grinder polisher (Buehler® EcoMet 30) to gain a perfect surface, then a sputter coating was applied to each sample cross-section with a thin layer of gold, with some representative SEM images displayed in Figure 4.4. Figure 4.4a shows the cross-section of the GFRP with an embedded GNP/epoxy sensor. The sensor was integrated into the bonding interface located in the middle of GFRP. It is observed in Figure 4.4c that GNPs are dispersed randomly and evenly in an epoxy matrix. Because of the uniform dispersion, it is conducive to creating a stable conductive percolating network in the nanocomposite. And in Figure 4.4d at a smaller scale, a substantial number of conductive paths built in the graphene network can be clearly observed, which is the precondition to trigger the tunneling current when subjected to external straining from quasi-static tensile, vibration, and GUWs, etc.

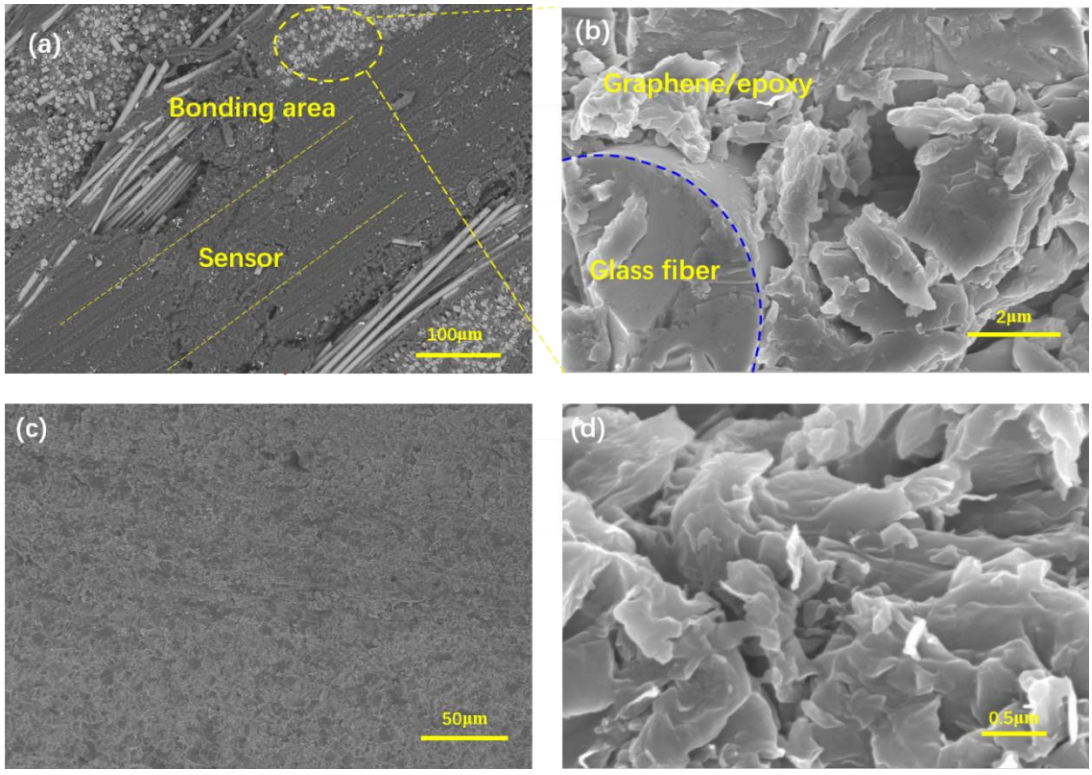

Figure 4.4 SEM images of (a) the cross-sectional GFRP laminate with an embedded

sensor, (b) the interface between composite and embedded sensor, and (c, d) graphene/epoxy nanocomposite sensor at two different scales.

As seen in Figure 4.4a, the sensor and glass fiber bundle are tightly bonded together to form a continuous whole in the area where the sensor is in contact with the glass fiber. And there is no visible interface between the GNP/epoxy sensor and composite matrix, the two are fused as a whole. A zoom-in of the GFRP where the embedded sensor is placed (see Figure 4.4b) further validates the tight sticking of the sensor material around the glass fiber, attributed to the identical matrix used for the nanocomposite sensor and the GFRP. Thus, the developed nanocomposite shows the potential of being truly non-intrusive to the host structure, while fulfilling the sensing capability, which are both validated in the following study.

4.5 Broadband Sensing Capabilities of GNP/epoxy Sensor

To examine the sensing capabilities of the developed GNP/epoxy sensor to strains in a wide range of magnitude and frequency, the quasi-static tensile load, dynamic cycling load, vibration, and GUW tests are all conducted as follows.

4.5.1 Quasi-static Test

The quasi-static tensile test of GFRP with sensor integration (250 mm × 25 mm) was performed to investigate the sensitivity of the sensor at different fabrication pressures. The changes in electrical resistance (ER) of the sensor were measured and recorded with a digital multimeter (Keithley® DMM7510) by the two point method as shown in

Figure 4.5. The normal strain of the composites was measured with the extensometer. Gauge factor (K) can be defined by the relative change in ER due to mechanical strain. This definition is shown in Formula 3.1

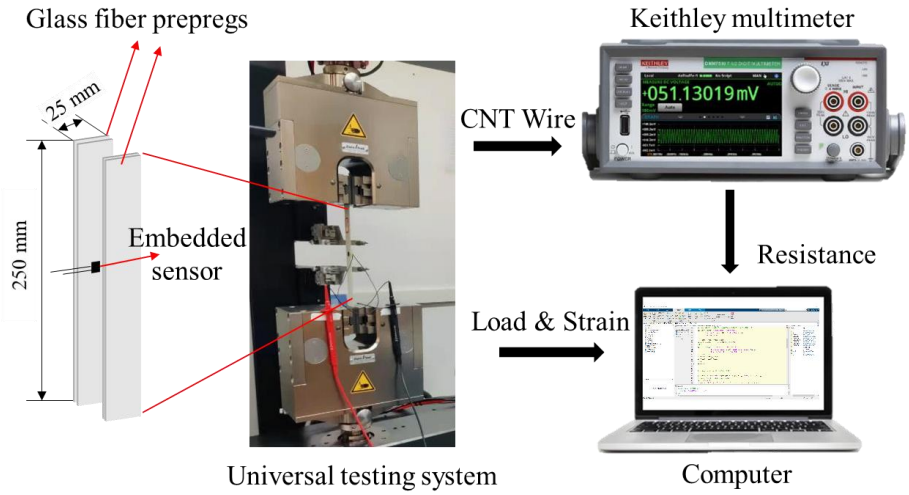

Figure 4.5 Experimental set-up of quasi-static test under tensile load.

The variation of gauge factor at different fabrication pressures is shown in Figure 4.6. Within the elastic domain (ε_t < 0.3%), the fitted gauge factors of GEP-15, GEP-20, GEP-25 and GEP-30 are 20, 22, 26 and 0, respectively. In consequence of the nanocomposite sensor material being in an uncured state when evacuated in a vacuum bag, it is pressed to a certain thickness at specified pressure. The embedded sensor fabricated at lower pressures with larger thickness builds more conductive paths through the thickness than thin sensor. However, more conductive paths impair the sensitivity of strain, because the gap variation between adjacent GNPs is not sufficient to cause significant global resistance changes [230]. In addition, the embedded sensor fabricated at -30 inHg pressure does not exhibit any sensing capability. It is because that the embedded sensor is over-pressed and the GNPs are separated at -30 inHg pressure, which cannot be connected to form a complete conduction path. As a result,

at -25 inHg fabrication pressure, the gauge factor of the sensor is larger than those that of sensors at lower fabrication pressures, and 12 times larger than commercial strain gauges ($K = 2$).

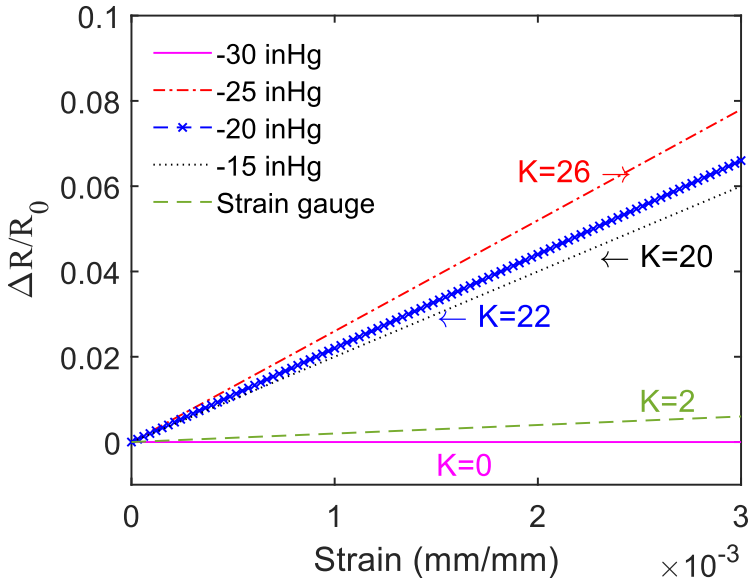

Figure 4.6 The fitted gauge factor of the sensor at different fabrication pressures with quasi-static tensile load.

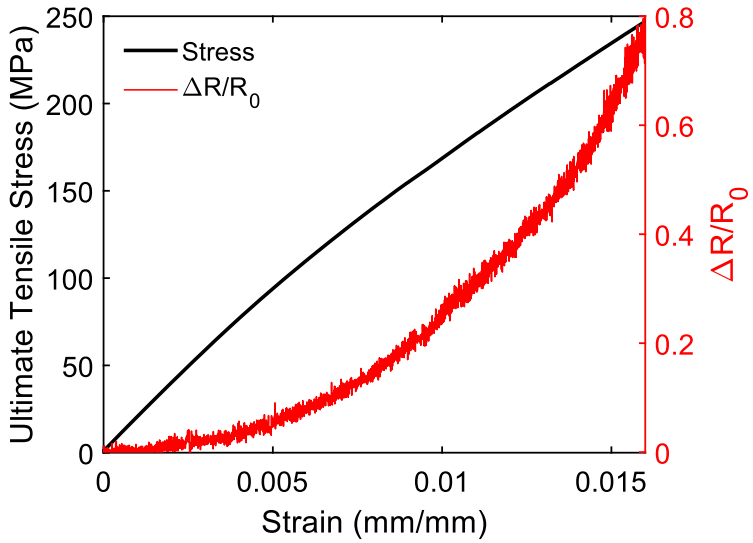

Figure 4.7 Stress-strain curve and ER change of GEP-25.

Figure 4.7 shows the relationship between ER and strain of GFRP with embedded

GNP/epoxy sensor in the larger strain domain. The result shows that the tensile load induces strain resulting in positive increment in ER. And particularly the ER of GEP-25 presents a marked exponential growth. This exponential increase can be attributed to changes induced by tunnel resistance, which increases exponentially with distance from adjacent graphene nanoparticles, as confirmed by Moriche et al [231]. Disruption of some conductive paths in the sensor at large strains can quickly lead to a large increase of ER in the sensor, resulting in a high sensitivity at large strains [230]. Therefore, different gauge factors of embedded sensor can be observed at different ranges of strain from Figure 4.7, which are around 26 (0-0.5%), 41 (0.5%-1%), 58 (1%-1.3%,), and 83 (1.3%-1.6%) for GEP-25, respectively. Hence, with the excellent mechanical properties and strain sensitivity, GEP-25 is adopted for further dynamic testing.

4.5.2 Dynamic Cycling Test

The long-term sensing stability of the embedded GNP/epoxy sensor in GFRP was examined with cyclic tensile test. All the specimens were cycled at a constant strain range from 0 to 0.3% (within the elastic domain) at a frequency of 0.1 Hz using LTM electrodynamic testing machine (ZwickRoell® linear testing system 10 kN).

As displayed in Figure 4.8, using a high-pass filter to filter out ambient noise, the ER change remains stable after 10000 cycles, indicating the good integrity of the conducting pathways in the developed sensor at quasi-static fatigue load. In order to observe the change of sensor resistance under a fatigue loading cycle, a few cycles (from 30 to 36 and 9970 to 9976) were selected to zoom in. The ER change presents a

slight decrease with the number of cycles increasing, which is corroborated in the reported works investigating fatigue in nanocomposites[232, 233]. That decrease could be associated to the relaxation of the polymer chains during a nanocomposite being cycled, thereby reducing the confinement of graphene nanofillers, causing the re-orientation of the nanofillers and the presence of stacked conductive particles or agglomerates.

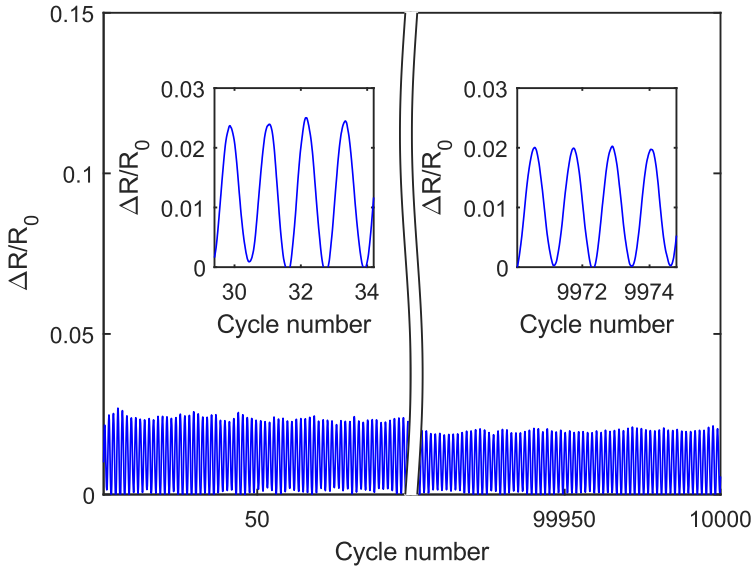

Figure 4.8 Filtered change ratio of ER of GNP/epoxy sensor at 0.1 Hz cyclic fatigue load.

The ER change is also interrogated. As displayed in Figure 4.9, in the initial 1000 cycles, there is an increase of 3.3% in the ER of embedded sensor, after the remaining 9000 cycles, the ER slowly increases by 2%. This phenomenon is very common for composites loaded for the first time, i.e., the first 1000 cycles are to eliminate the prestress introduced by the preparation process. After the sensor was unloaded and stored statically for 30 days, the resistance of the sensor remains at the same value at the end of the fatigue experiment. It demonstrates that the microstructure of the

embedded sensor slightly changes resulted from an irreversible change during cyclic loading. Because it is difficult to completely remove the fine air bubbles in the sensor during the preparation process, which leads to crack propagation as the nanocomposite sensor undergoes cyclic tensile loading. Ultimately, this internal cracking leads to the destruction of part of the conductive network at the crack. With cycles from 875 to 880 (see inset in Figure 4.9), the ER change exactly correlates with the applied load with no phase delay. The indicated quick response ability provides a potential for the sensor application to strains of higher frequency such as vibration and GUWs, which are tested as follows.

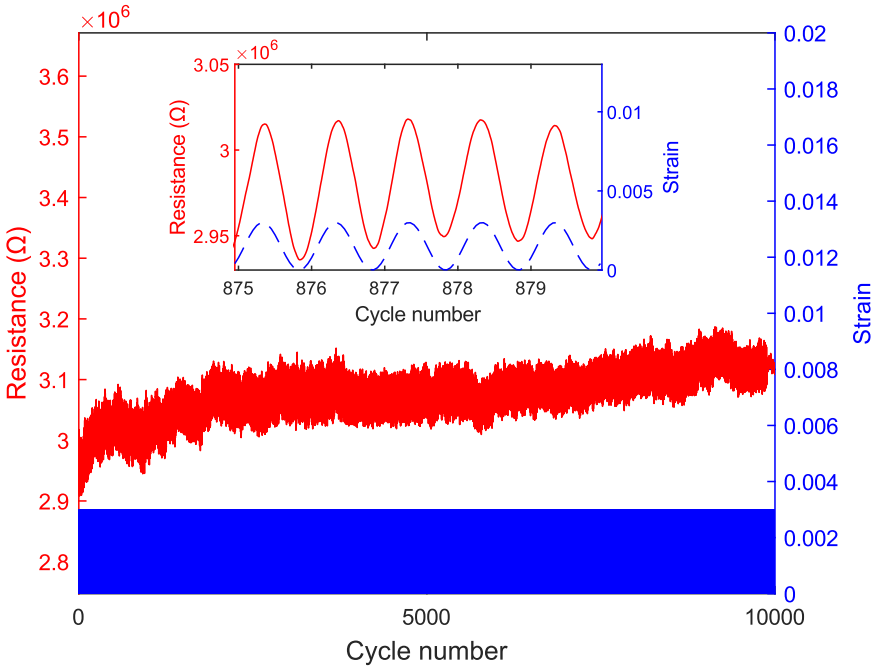

Figure 4.9 ER change of the embedded sensor at the cyclic strain of 0.3%.

4.5.3 Vibration Test (300 Hz to 2 kHz)

After the quasi-static testing, the dynamic electromechanical response of the GFRP laminate (300 mm × 80 mm × 0.87 mm) with an embedded sensor was tested. The experimental platform is shown in Figure 4.10. One end of the laminate was clamped

by a plain vice fixed on the bracket as a cantilever beam, while the other end was excited by the vibration machine. The excitations (from 300 Hz to 2 kHz) were generated by a waveform generator (Tektronix® AFG31051) through an electromechanical shaker system (SKC® YE-10) at 40 mm from the free end of a laminate. To calibrate the sensor performance, a strain gauge (350 Ω) was attached to the surface of the laminate at the same position as the sensor, which was 60 mm from the fixed end. The dynamic responses of the sensor and strain gauge were measured with a self-developed adjustable and commercial acquisition system, respectively. The self-developed adjustable system integrates a Wheatstone bridge with adjustable resistors compatible with the ER of the developed sensor, which is powered by a power supply (ITECH® IT6302), and the commercial acquisition system (KYOWA® DPM-911B) was composed of a Wheatstone bridge and a signal conditioner. Then, both signals were input into an oscilloscope (Keysight® Infiniium MXR058A).

With a low magnitude of elastic disturbance from the vibration test, signals are prone to disturbance from the ambient noise and power radiation. Thus a band pass filter from 100 Hz to 5 kHz was applied to the raw signals. A sinusoidal vibration signal sweeping frequency test from 300 Hz to 2 kHz was performed, and the response signals are shown in Figure 4.11. By observing the response signal, it is found that the sensor has a very good capability of dynamic stability, repeatability, and response reversibility, and the filtered signals show no waveform distortion or hysteresis. After that, a random frequency of 800 Hz is selected from the frequency sweeping to compare the response signal of the sensor and the strain gauge at this frequency as displayed in Figure 4.12. Since the two sensors are installed at different thicknesses of GFRP, the collected signals exhibit the differences in terms of both the magnitude and phase, but show the

same frequency as the vibration excitation.

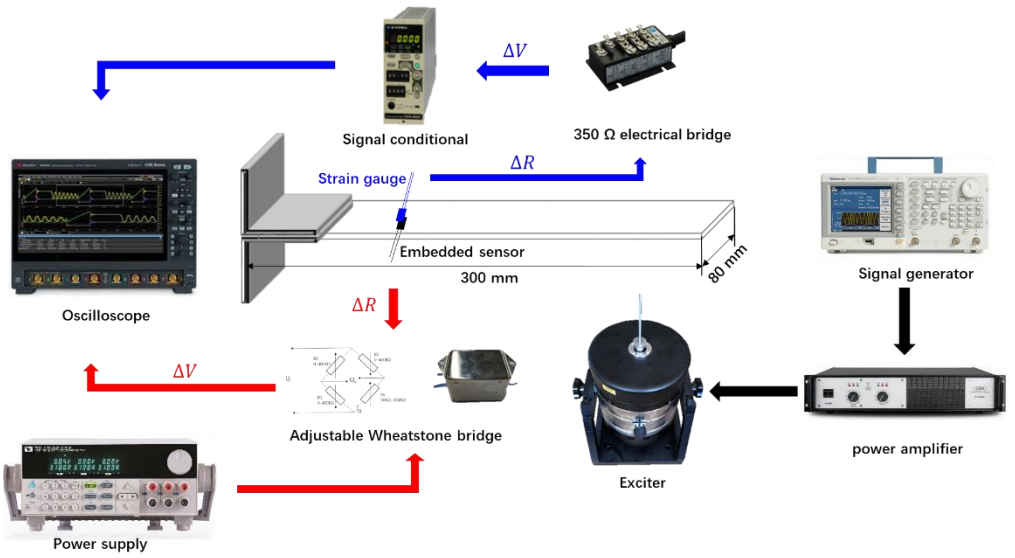

Figure 4.10 Experimental set-up of dynamic vibration test.

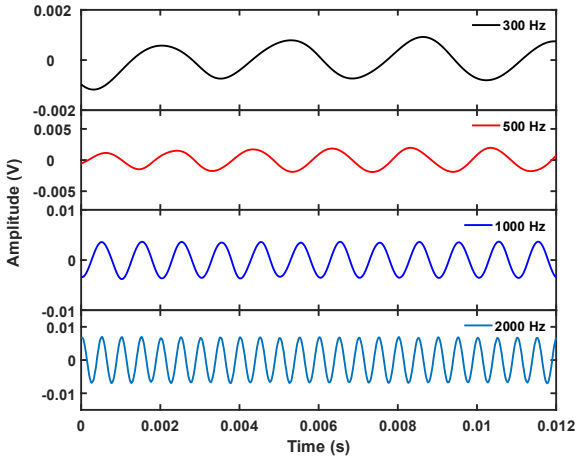

Figure 4.11 Vibration response of GNP/epoxy sensor at different frequencies from 300 Hz to 2 kHz.

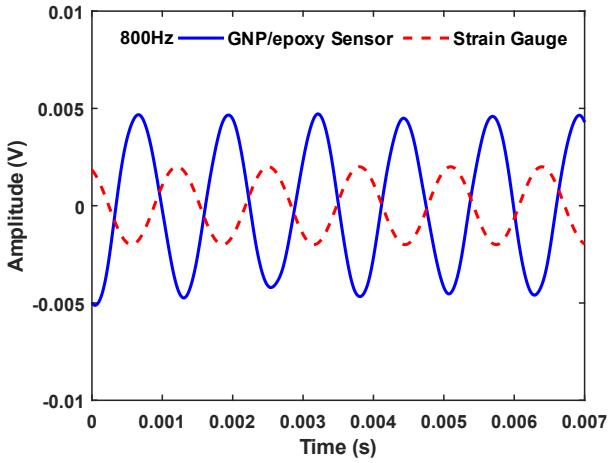

Figure 4.12 Response of GNP/epoxy sensor and strain gauge at 800 Hz.

4.5.4 Guided Ultrasonic Wave Testing (150 kHz to 600 kHz)

Following the same fabrication process as detailed in Section 8.3, a GFRP (200 x 300 x 0.87 mm^3) with the embedded sensor was prepared, on which a lead zirconate titanate (PZT) wafer (PSN-33, Ø10 mm, 1 mm thick) was surface mounted. A 3-cycle Hanning-window-modulated sinusoidal tone burst with the central frequency varying from 150 kHz to 600 kHz was generated by a waveform generator (Tektronix® AFG31051), and then amplified using a power amplifier (Falco systems® WMA-300) to a Vpp of 300 V to excite the PZT wafer. Another receiving PZT wafer was mounted on the surface where the GNP/epoxy sensor had been embedded, which is 150 mm from the excited PZT, to calibrate and compare the signal acquired with both sensors, as shown in Figure 4.13. For the developed nanocomposite sensor, the elastic disturbance-induced ER change was captured with a signal acquisition system, which consists of a self-developed adjustable amplification module and an oscilloscope. To suppress ambient noise and measurement uncertainties, the adjustable amplification module powered by a power supply (ITECH® IT6302) was developed, which is composed of a resistance-voltage transformation module converting piezoresistive variation to electrical signals, a bandpass filter, and a high-gain amplification module.

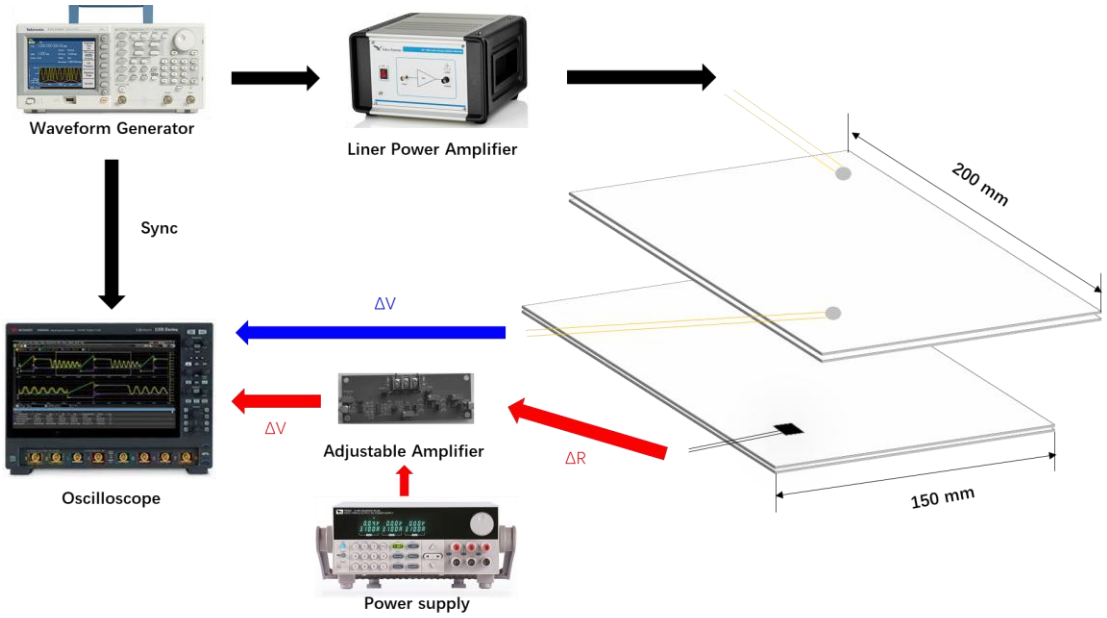

Figure 4.13 Experimental set-up of GUW test.

Figure 4.14 shows filtered ultrasonic signals acquired with GNP/epoxy sensor and PZT wafer between 150 kHz and 600 kHz. The qualitative coincidence in the time-of-flight of the first arrival zeroth-order symmetric Lamb wave (denoted by S_0) acquired with PZT and an embedded GNP/epoxy sensor for the wave modes is observed. Discrepancies in signal magnitude captured with the two types of sensors can be attributed to the distinct sensing mechanisms. The PZT wafer measures the changes in piezoelectricity, whereas the nanocomposite sensor measures the variation in piezoresistive properties based on the tunneling effect. To further investigate the sensing performances between 150 to 600 kHz (with a step of 30 kHz), the spectra of signals perceived with the GNP/epoxy sensor (see Figure 4.15a) and PZT wafer (see Figure 4.15b) are displayed over the time-frequency domain. Results show that the GNP/epoxy sensor exhibits a comparable sensing capability to a commercial PZT wafer.

Thus, the embedded GNP/epoxy can be used to monitor the health condition of composite structures.

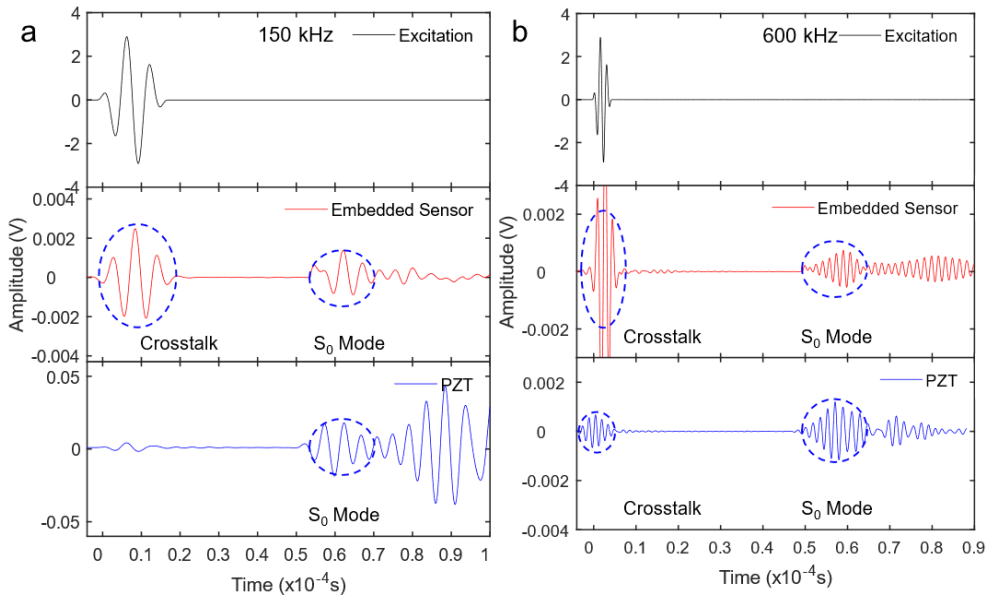

Figure 4.14 GUW signals acquired with the embedded GNP/epoxy sensor and surface-mounted PZT wafer at (a) 150 kHz, and (b) 600 kHz.

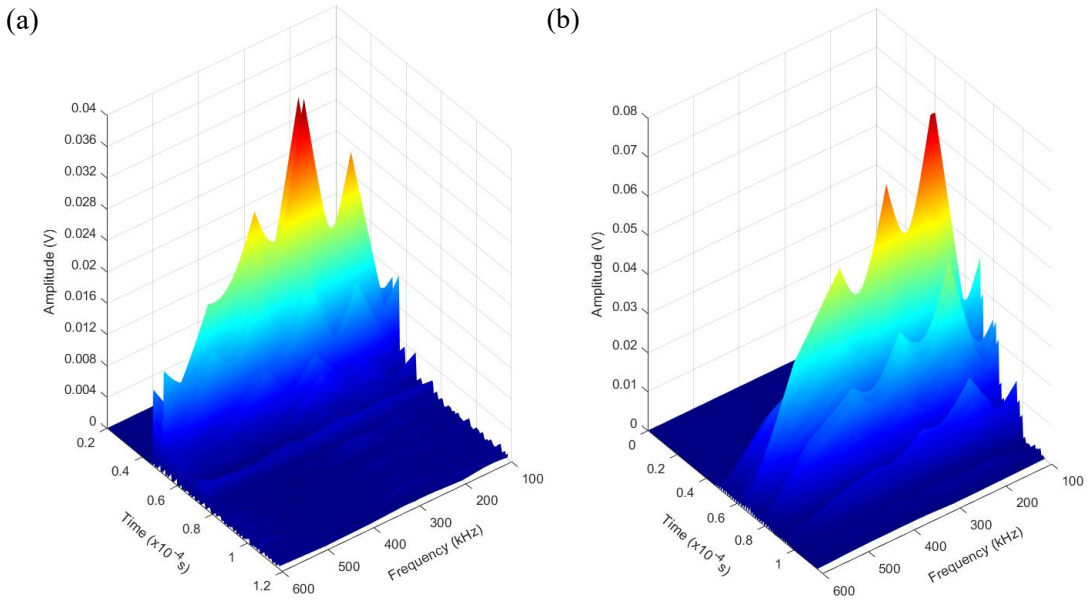

Figure 4.15 Time-frequency domain responses of (a) embedded GNP/epoxy sensor and (b) PZT wafer.

4.6 Mechanical Properties

To study whether the developed GNP/epoxy sensor with a gauge factor up to 26 is mechanically compatible with composite structures, GFRP composites with embedded sensor fabricated at -25 inHg were tested with the tensile and three-point bending tests to investigate the effect of an embedded sensor on the mechanical properties of composites. Five samples were tested for each GFRP configuration.

4.6.1 Tensile Test

The tensile test was performed according to ASTM D3039 using a universal testing system (ZwickRoell® 20 kN Allround tabletop), as shown in Figure 4.16a. The GFRP composites with and without an embedded sensor at the center of the composite are 250 mm × 25 mm × 0.89 mm in the in-plane dimension. To suppress the random errors, five samples were tested for each test. The raw dimension of the sensor before pressing is 4 mm × 4 mm. Glass fiber tabs were attached at two ends of the specimen with epoxy glue (3M® DP460) as reinforcing sheets to avoid breakage in the gripping area. The test was performed at a constant cross-head speed of 2 mm/min.

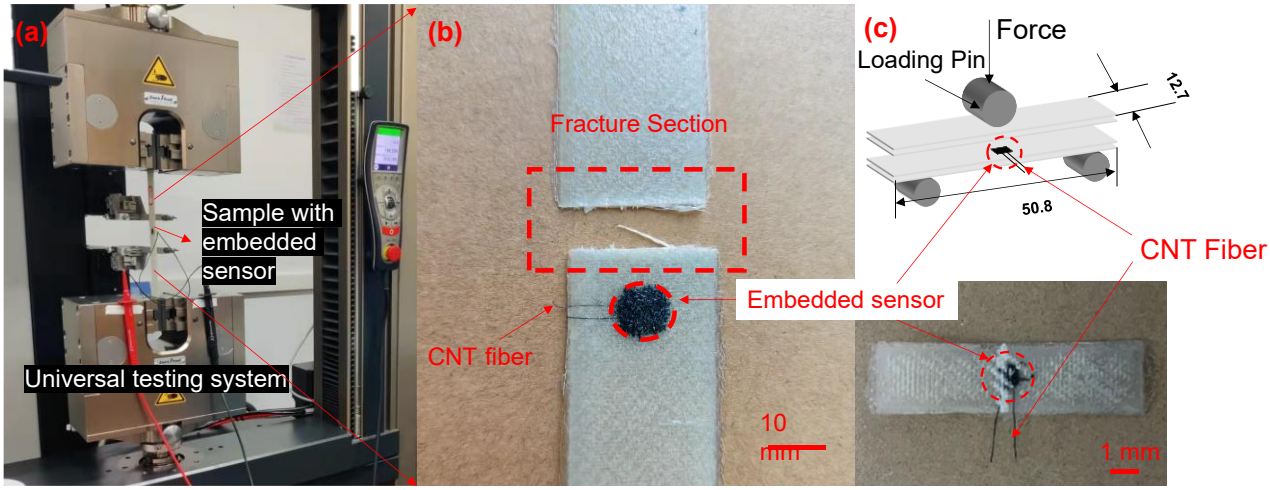

Figure 4.16 (a) Experimental setup of tensile test, (b) fracture of laminates with an embedded sensor, and (c) schematic diagram of three-point bending experiment.

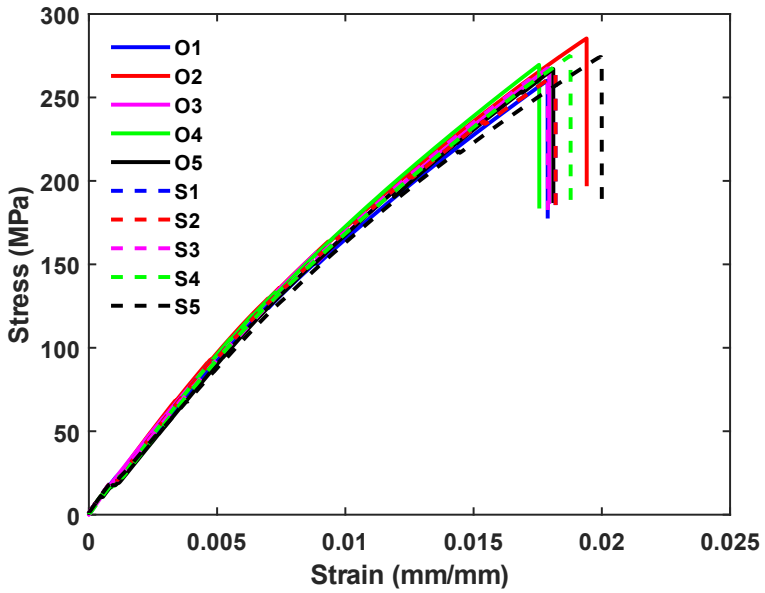

Figure 4.17 Characteristic stress-strain curves (O1-O5: without embedded sensor; S1-S5: with embedded sensor).

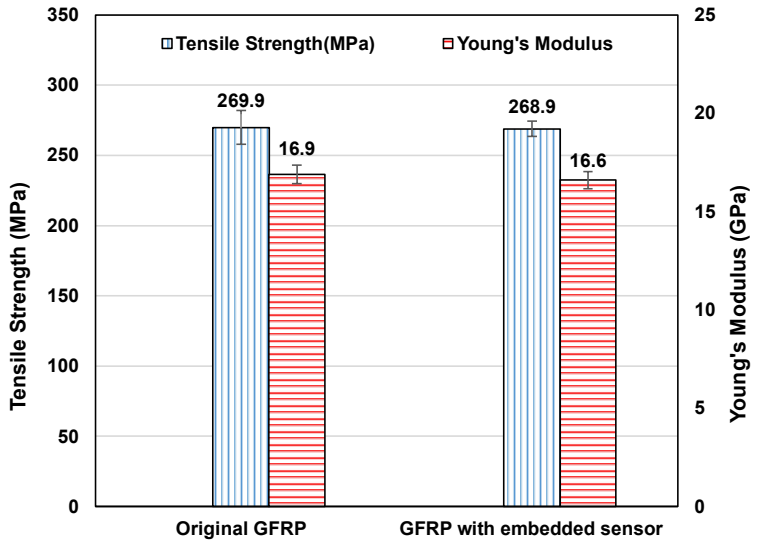

Figure 4.18 Tensile modulus and strength of GFRP with and without sensor.

Figure 4.17 shows the result of GFRP with and without embedded sensor under tensile load. The stress-strain curve (in Figure 4.17) for the GFRP composites with and without embedded sensor displays stress increasing gradually with applied tensile strain before reaching a brittle fracture. As displayed in Figure 4.16b, for all the five samples, the fracture occurs away from where the sensor was placed, which indicates the strong bonding between sensor and prepreg that withstands the tensile load.

Similarly, Figure 4.18 shows the comparison of tensile properties of composite with and without sensor. The tensile strength and Young's modulus of composite with embedded sensor are -0.3% and -1% less than the original GFRP, respectively, and this subtle difference comes from discrepancy in sample manufacturing and testing. Thus, the integration of the sensor, made of the same polymer as the host structure, shows almost the same mechanical property as the original host GFRP.

4.6.2 Three-point Bending Test

Following the above tensile test, the bending performance between the GFRP with and without the embedded sensor was further tested with the three-point bending test, which was performed using the universal test platform (WANCE TEST® TSE503A) with the speed of crosshead of 1 mm/min. Five respective GFRP samples (50.8 mm × 12.7 mm × 0.89 mm) with and without an embedded sensor (2 mm × 2 mm) were prepared according to ASTM D790. To validate the influence of the embedded sensor on the bending performance, the cross section where the sensor is embedded is placed in the middle point of the test platform which withstands the largest bending moment, as shown in Figure 4.16.

The stress-strain curves under three-point bending of the GFRP with and without embedded sensor is shown in Figure 4.19. As displayed in Figure 4.20, compared with the original GFRP with the flexural strength and modulus of 412 MPa and 13.1 GPa, respectively, the GFRP with embedded sensor shows a slightly increase by 2.7% and 5.3%, respectively, attributed to the slight increase of thickness in the interply layer from the embedded GNP/epoxy sensor.

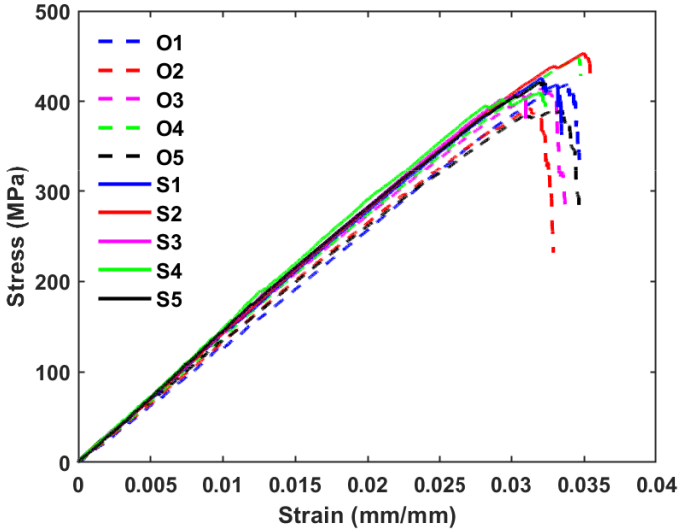

Figure 4.19 Characteristic stress-strain curves under three-point bending (O1-O5: without embedded sensor; S1-S5: with embedded sensor).

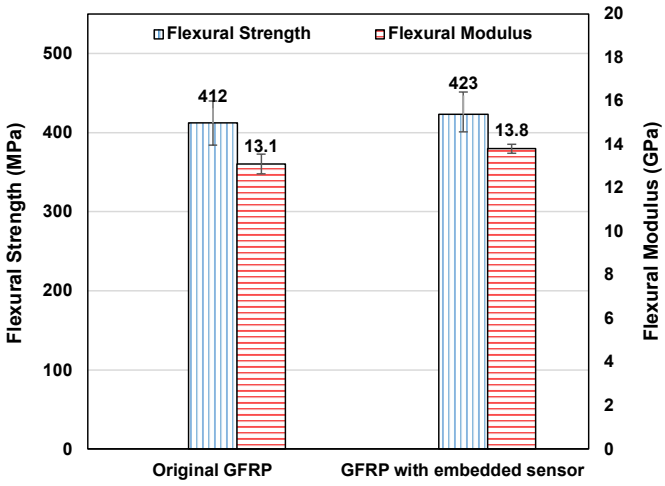

Figure 4.20 Flexural modulus and strength of GFRP with and without sensor.

4.7 Summary

A nonintrusive GNP/epoxy nanocomposite sensor embedded into GFRP was developed. In an uncured state, the sensor is embedded in the specific prepreg layer during lay-up to laminate and then co-cured with GFRP composite. As observed from nanoscale morphological characterization, a remarkably reduced intrusion to the composites

compared with conventionally embedded sensors is that this sensor with identical matrix of epoxy blends with prepreg's epoxy during curing process. Different pressures are applied to the co-curing process of GFRP with embedded sensors, whose gauge factors and mechanical performances at quasi-static tensile loading are found to reach a great balance at -25 inHg pressure. With the tested gauge factor up to 26 at -25 inHg pressure, the excellent sensing capabilities of the developed sensor at cycling loading, vibration, and GUW up to 600 kHz are proved, exhibiting high stability, reversibility, and repeatability in responding to dynamic strains without phenomenal hysteresis and deviation. In addition, a series of tensile and bending tests prove that the GFRP composite's structural stiffness and strength are not adversely affected by the embedded sensor. Hence, GFRP composites with embedded sensor have both the inherent high mechanical properties from GFRP and the strain-sensing capabilities from sensor, which endows fiber-reinforced composites with potential for *in situ* health monitoring.

CHAPTER 5

Aerosol Jet Printed Graphene/CNC Sensors

5.1 Introduction

Conventional sensor fabrication methods are often costly, complex, and limited in scalability, while other printing techniques suffer from narrow ink compatibility or poor conformability. In contrast, AJP offers high-resolution, maskless deposition on diverse substrates, accommodating a broad range of ink viscosities and particle loadings. These advantages make AJP particularly attractive for flexible electronics and nanocomposite sensor fabrication.

In this chapter, graphene/CNC nanocomposite inks with eight different graphene concentrations are formulated and processed via AJP to fabricate flexible sensors. The printing parameters are systematically optimized to ensure uniform deposition and high-quality feature definition. The resulting sensors are first examined in terms of their microstructural morphology, highlighting the influence of graphene concentration on film formation. Their sensing performance is then evaluated across a broad frequency spectrum, from quasi-static strains to high-frequency ultrasonic excitations, to elucidate the relationship between filler content, microstructure, and frequency-dependent

sensitivity.

5.2 Preparation of Nanocomposite Sensor

The fabrication of the sensor begins with the preparation of a precursor solution containing an insulating spacer suspension (CNCs in deionized water (DI water)) and a conductive suspension (graphene in ethanol). Sensor inks, prepared by homogeneously mixing graphene and CNCs suspensions at varying weight ratios, are used to fabricate a series of specific sensors with customized patterns through aerosol jet printing. The synthesis process of the sensor ink is illustrated in Figure 5.1. Graphene (50 μm in diameter, < 3 layers, and > 95% purity, TIME NAN® TNERGO-50) and CNCs (~10 nm wide and ~200 nm long, ScienceK® CNCs) are respectively dispersed in alcohol and DI water using an ultrasonic crusher for 30 minutes, whereby to produce graphene ink with the concentration of 5.5 mg/ml in alcohol and CNCs with the concentration of 5.8 mg/ml in the DI water. Subsequently, the graphene and CNCs are mixed at a mass ratio of 1:9 to 8:2, to create a sensor ink readily available for AJP. Printed sensors with inks of different mass ratios between graphene and CNCs are denoted as GC-x (x = 10, 20, ..., 80), where x corresponds to the weight percentage of graphene in the nanocomposite. For example, GC-10 refers to a sensor fabricated with 10 wt.% graphene in the graphene/CNC nanocomposite. These inks exhibit viscosities in the range of 2.8–4.3 cP (RheoSense® microVISO), which lie well within the printable window of AJP and ensure the formation of continuous, uniform tracks. The electrodes

of each sensor are prepared using commercially available silver ink (NOVACENTRIX® JS-A221AE).

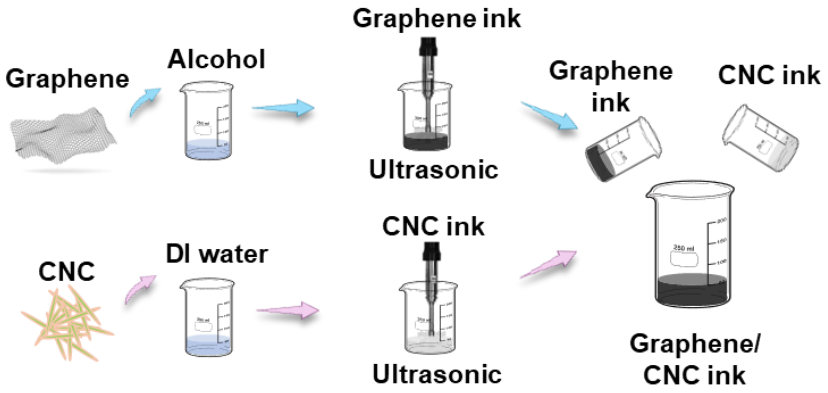

Figure 5.1 Fabrication flow of sensor ink.

5.3 Printing Process

The sensor and silver conductive circuits are printed on an aerosol jet 3D printing platform (Optomec® AJP300). To preserve the layered structure of graphene, pneumatic atomization is employed for the nanocomposite ink, while ultrasonic atomization is used for the silver ink, eliminating the need to clean pathways during the process. The nanocomposite ink is continuously stirred at 500 rpm to prevent graphene aggregation, and the build platform is maintained at 80°C to accelerate solvent evaporation. Printing parameters such as atomizer flow rate, sheath flow rate, and stage speed, which influence the geometry and quality of the sensing unit, are discussed in the following Section 5.4. To prevent nozzle clogging, sheath gas is introduced to accelerate the atomized ink stream, ensuring precise deposition onto the GFRP laminate

in the desired pattern (Figure 5.2).

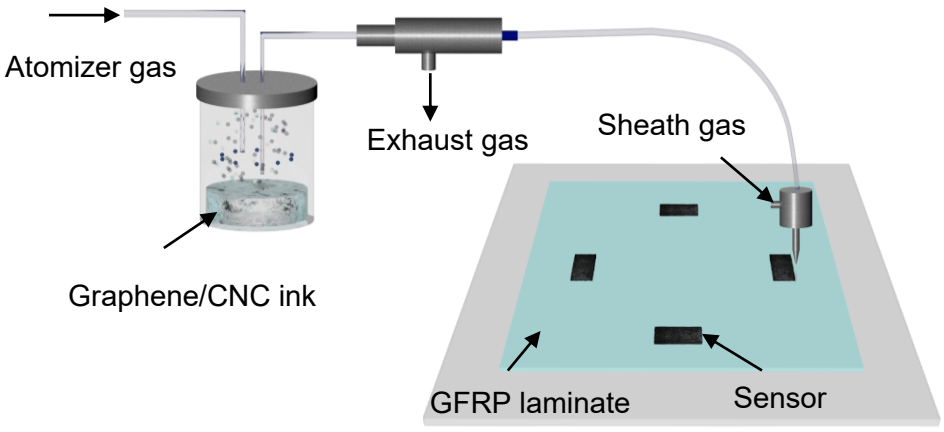

Figure 5.2 AJP for sensor printing.

This printing process facilitates microscale self-assembly of graphene/CNCs layered structure, involving three distinct stages: deposition, evaporation, and formation (Figure 5.3a, b, c). In the deposition stage, atomized droplets of the sensor ink land on the substrate, with graphene and CNCs uniformly suspended in the solvent (DI water and ethanol), and each particle is surrounded by solvent molecules, keeping the particles independent of each other (Figure 5.3a). In the evaporation stage, driven by the heated building platform, the solvent evaporates and van der Waals forces between graphene sheets increase, promoting the stacking tendency of graphene (Figure 5.3b). In the formation stage, CNCs act as the mediator, effectively retarding graphene stacking process. Upon full solvent evaporation, a stable layered structure composed of alternating graphene and CNCs layers is established (Figure 5.3c), with hydrogen bonding between CNCs and graphene further enhancing structural stability.

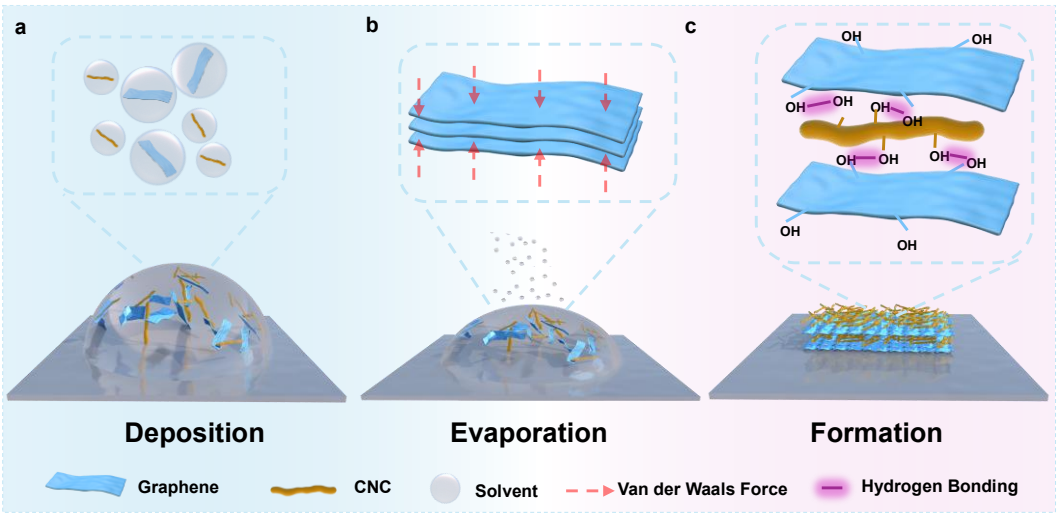

Figure 5.3 The self-assembly process of graphene/CNCs sensor via aerosol jet printing

5.4 Selection of Printing Parameters

Selecting the optimal printing parameters is crucial in the AJP process. Among various parameters, the focusing ratio – the ratio of the sheath gas flow rate to the atomizer gas flow rate, and the stage speed are pivotal, as they remarkably affect the printing quality [60, 234, 235].

Considering the viscosity and composition of the prepared graphene/CNC nanocomposite ink, the atomizer gas flow rate is set at 600 standard cubic centimeter per minute (sccm) to form a stable and even distribution of aerosol droplets, and the sheath gas flow rate is regulated in a range from 400 to 1000 sccm. A greater sheath flow rate can improve the focusing of the aerosol droplets, which, however, commits a higher risk to blow away the unevaporated ink droplets, causing undesirable sputtering of the ink. On the contrary, a lower sheath flow rate may not provide sufficient focusing of ink. In the meantime, different printing stage speeds are tested from 4 to 12 mm/s

with an increment of 2 mm/s.

Figure 5.4 shows the microscopic morphology of the printed graphene/CNC sample as observed with an optical microscope (KEYENCE® VK-X200), under three representative sheath gas flow rates and four representative stage speeds. As seen in Figure 5.4, different sheath gas flow rates and stage speeds lead to different degrees of focusing of the graphene/CNC ink on the lower nylon insulation layer, as well as different areas of the overspray region out of the printing region. Preferably, the width of the overspray region shall be smaller than half width of the printing region [59].

As noted in Figure 5.4, increasing the sheath gas flow rate from 400 to 1000 sccm at a constant stage speed can enlarge the width of the overspray region and decrease the width of the printing region. A higher sheath flow rate creates a greater air pressure difference between the sheath flow and the atomizer flow, exerting a higher compressional load on the atomizer flow at the nozzle, thereby narrowing the printing region [235]. However, part of the accelerated aerosol stream under the higher speed of sheath flow is observed to rebound into the overspray region, as observed in other studies elsewhere [127, 236]. In contrast, an excessively lower sheath flow rate, say 400 sccm, fails to focus the aerosol droplets, resulting in scattered ink droplets over the printing region. Together, a superior printing quality – showing a minimized overspray region and focused ink droplets in the printing region, can be obtained when the sheath flow is set at 600 sccm.

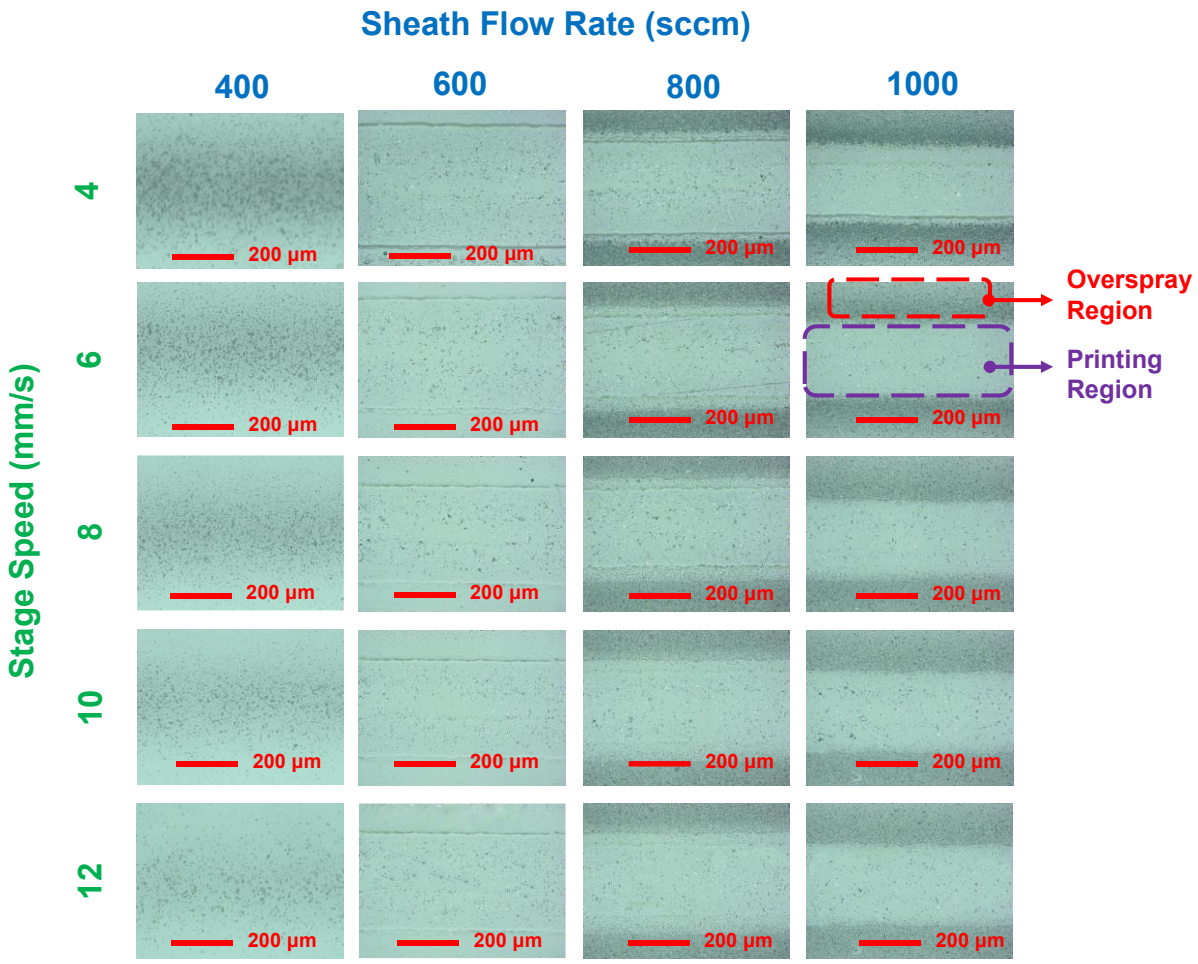

Figure 5.4 Microscopic images of the printed areas under different AJP settings of sheath flow rate and stage speed.

Given a fixed sheath flow, different printing stage speeds, varying from 4 to 12 mm/s, are observed to lead to different widths of the printing region, Figure 5.4. In general, the faster the stage speed the narrower the printing region it will be. However, when the stage speed is above 10 mm/s, the width of the printing region no longer changes remarkably. These experimental findings corroborate earlier discoveries in other studies[60, 127, 234].

Considering the above observations, a sheath flow rate of 600 sccm and a stage speed of 10 mm/s are considered to be the most optimal printing parameters of AJP in the

hybrid printing. With this, the most optimal AJP parameters in this study are listed in Table 5.1.

Table 5.1 Optimal AJP parameters used for printing the graphene/CNC ink and silver ink.

Printing parameters for graphene/CNC ink		Printing parameters for silver ink	
Atomization Method	Pneumatic	Atomization Method	Ultrasonic
Sheath Flow rate (sccm)	600	Sheath Flow rate (sccm)	50
Atomizer Flow rate (sccm)	600	Atomizer power (mA)	500
Platform Speed (mm/s)	10	Platform Speed (mm/s)	10
Nozzle Size (μm)	300	Nozzle Size (μm)	150
Platform Temperature (°C)	80	Platform Temperature (°C)	25

5.5 Characterization

The microscale morphology of the graphene/CNC sensor is examined using SEM (TESCAN® MIRA LMS), complemented by energy dispersive spectrometer (EDS) elemental analysis at different graphene concentrations (in Figure 5.5). As summarized in Table 5.2, the progressive decrease in oxygen content with lower CNC fractions aligns with the reduced cellulose presence, faithfully reflecting the designed graphene/CNC ratios. Both the SEM images and elemental mapping in Figure 5.5 reveal the distribution of graphene and CNC: at lower graphene loadings (10–30 wt.%), both components are uniformly dispersed, while at higher loadings (60–80 wt.%), graphene becomes dominant and tends to coat the CNC surface. These microstructural

characteristics govern the formation of the conductive network, which in turn underscores the sensing performance of the sensor, as discussed in detail in the following section.

Table 5.2 EDS quantitative analysis of C and O content for graphene/CNC composites at different graphene loadings.

GRAPHENE (WT%)	C (WT%)	O (WT%)
10%	66.41%	33.59%
30%	69.69%	31.31%
60%	96.8%	3.2%
80%	97.34%	2.66%

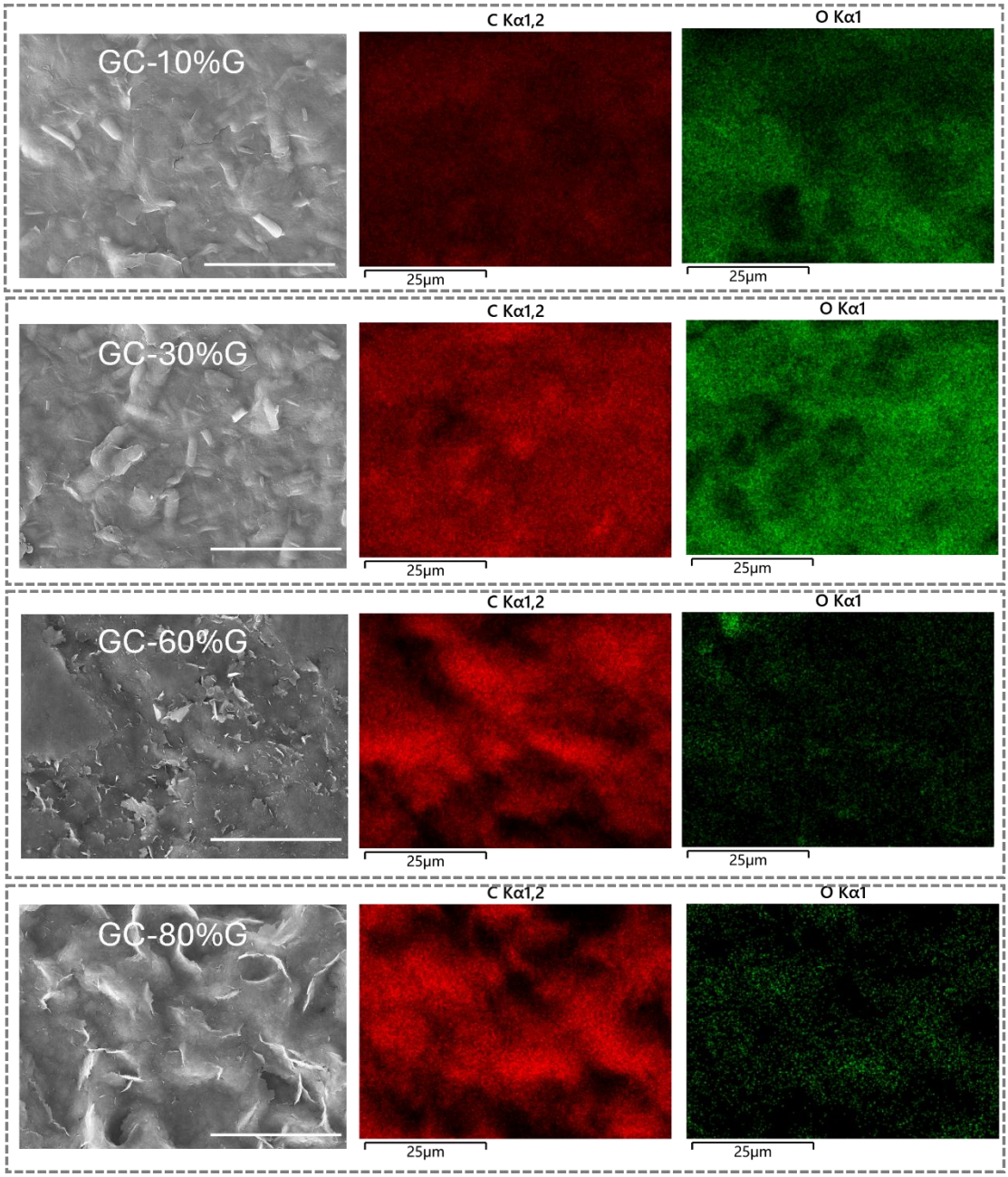

Figure 5.5 SEM images and corresponding EDS elemental mapping (C and O) of graphene/CNC composites at varying graphene loadings.

5.6 Sensing Performance in Low-frequency

A series of sensors (dimension of 20 mm×10 mm) with different graphene/CNCs ratios, are measured their response at different tensile strain levels, varying both amplitude

and frequency. The tensile measurement set-up includes a universal testing system (INSTRON® 5982) equipped with a 1 kN load cell for applying tensile load on the sample, a digital multimeter (Keithley® DMM7510) for recording the relative resistance changes of the sensing unit through the two-point method, and a computer for recording and analyzing data.

The relative resistance changes of sensors, prepared with varying graphene to CNCs weight ratios (GC-10 to GC-80), is measured under uniaxial quasi-static tensile loads across strain ranges of 0% to 0.4% and 0% to 0.1%, respectively (Figure 5.6 and Figure 5.7). In the strain range from 0% to 0.2% (Figure 5.6), all sensors exhibited a positive correlation between strain and relative resistance change, and with familiar sensitivity of ~0.7. In Figure 5.6, the performance of these sensors under ranges from 0% to 0.1% is not readily discernible. An enlarged view for clearer observation is shown in Figure 5.7, demonstrating that the sensor with 40% graphene content (GC-40) displayed the highest sensitivity (~0.9) in this range. Within the strain range of 0.2%–0.4% (Figure 5.6), a nonlinear increase in resistance is observed. The sensor with higher graphene content (GC-80) exhibits a gauge factor of up to 10 and shows a more pronounced relative resistance change, indicating enhanced sensitivity at higher strain levels.

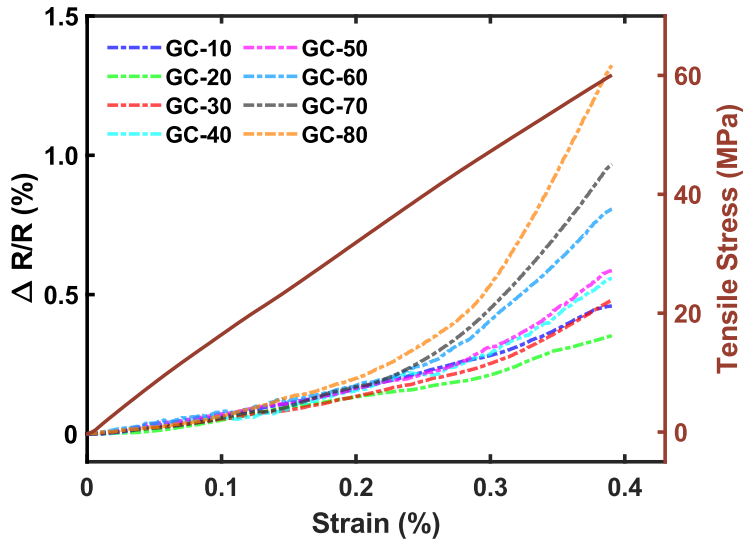

Figure 5.6 Relative resistance changes of the Graphene/CNCs sensor at the strain ranges from 0 to 0.4%.

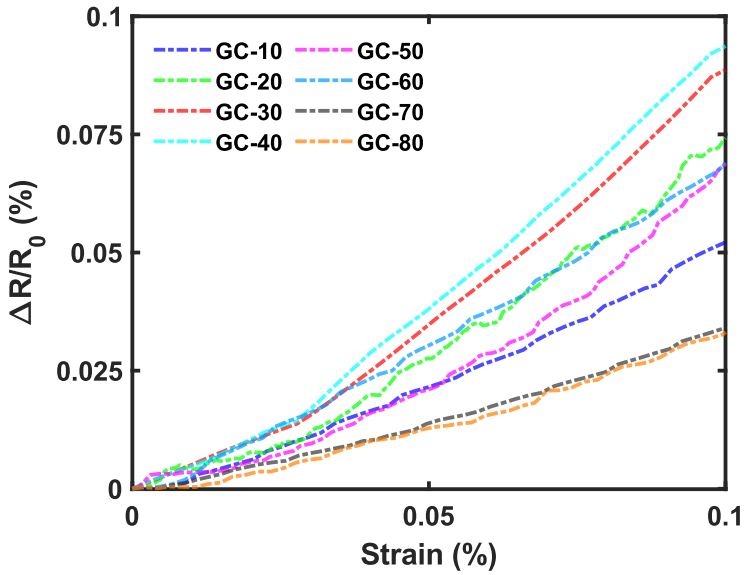

Figure 5.7 Relative resistance changes of the Graphene/CNCs sensor at the strain ranges from 0 to 0.1%.

This phenomenon occurs not only in quasi-static tests, but also in tensile cyclic tests at the frequency of 1 Hz. Figure 5.8 presents the relative resistance changes of eight

sensors, subjected to three dynamic strain levels of 0.12%, 0.19%, and 0.23% at a constant frequency of 1 Hz. The GC-40 sensor demonstrates higher sensitivity at the strain level of 0.12%, while GC-80 performs optimally under higher dynamic strain of 0.19% and 0.23%. By way of illustration, the relative resistance changes from GC-10 to GC-80 under a representative strain of 0.23% at a frequency of 1 Hz are shown in Figure 5.9. These are because at higher graphene concentrations (GC-80), the stacked graphene layers create an inert conductive network that can only be reconstructed under the application of larger strain. In contrast, the GC-40 sensor with optimized interlayer spacing enhances its sensitivity to smaller strains by facilitating tunneling currents and allowing even minimal strain to alter the internal conductive network.

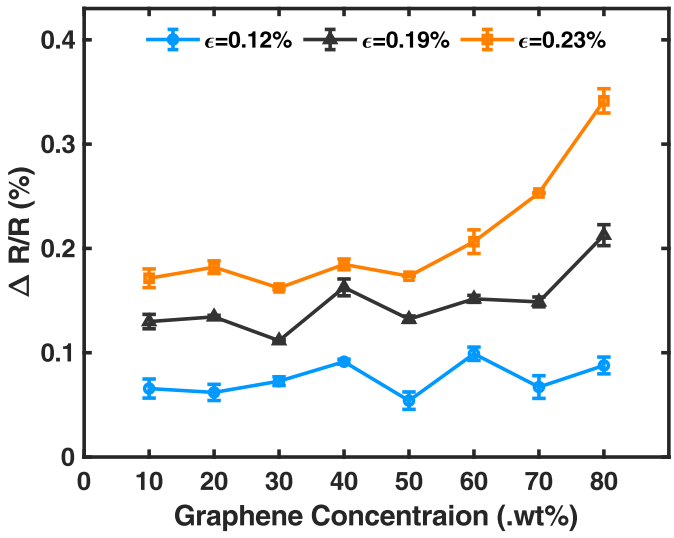

Figure 5.8 Resistance response of different sensors (GC-10 to GC-80) under periodic tensile strain of 0.12%, 0.19% and 0.23%, respectively, at the frequency of 1 Hz.

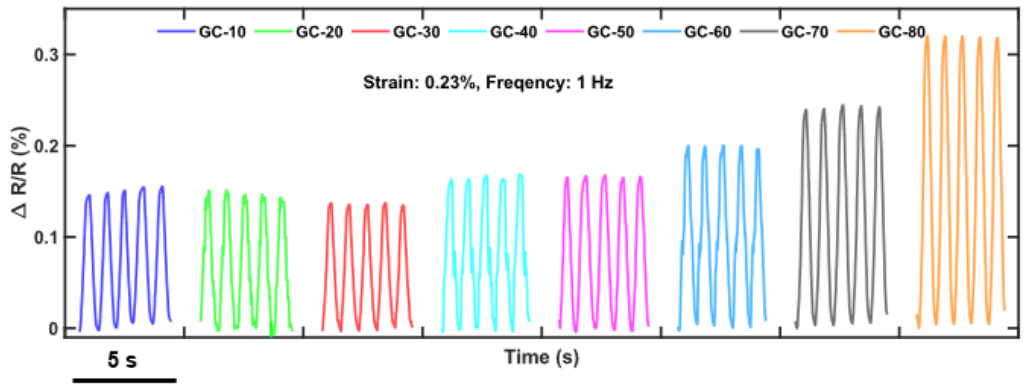

Figure 5.9 Relative resistance changes of different sensors under a representative strain of 0.23% at the frequency of 1 Hz.

The sensor exhibited a highly repeatable response when subjected to cyclic tensile strain of 0.23% at the frequency of 1 Hz (Figure 5.10). In addition to the merits of sensitivity and repeatability, the frequency resolution is another important advantage of the sensor, which accurately detects frequency changes at 0.4 Hz, 0.6 Hz, and 0.8 Hz (Figure 5.11), consistent with the frequency of applied load, as shown in Figure 5.12. The sensor also demonstrates excellent performance in reliably distinguishing and responding to different levels of cyclic tensile strain of 0.12%, 0.19%, 0.23% (Figure 5.13).

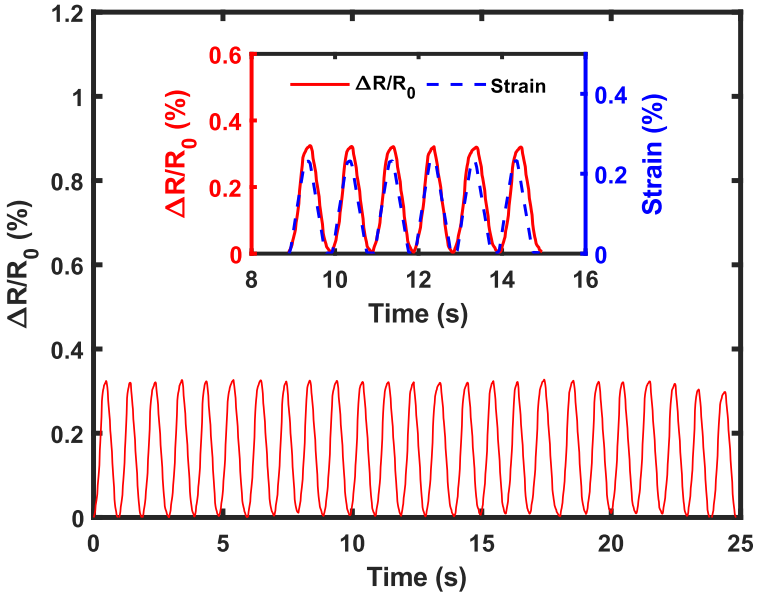

Figure 5.10 Repeatability of GC-80 under periodic strain of 0.23% at frequency of 1 Hz.

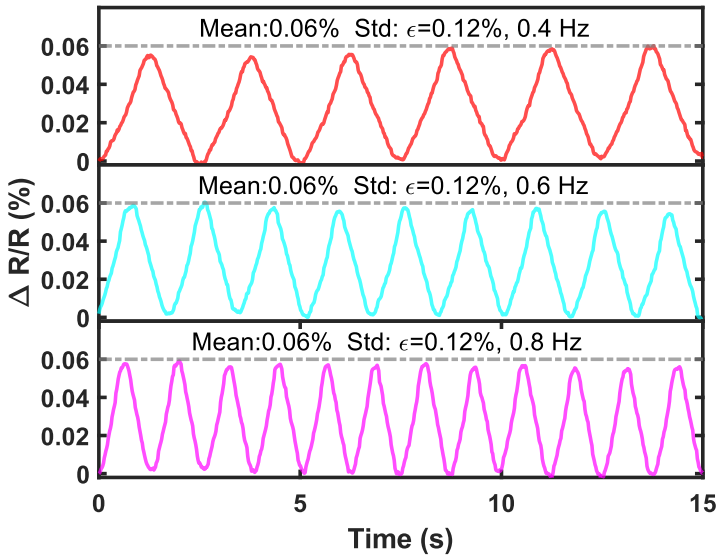

Figure 5.11 Relative resistance changes at different frequencies for a representative sensor GC-80 under a constant strain of 0.12%.

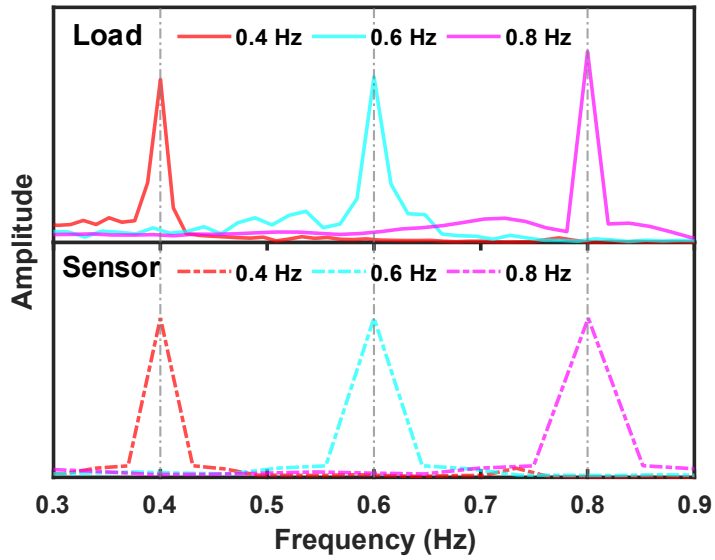

Figure 5.12 The frequency spectra of applied load and sensor under three representative frequency of 0.4 Hz, 0.6 Hz, and 0.8 Hz.

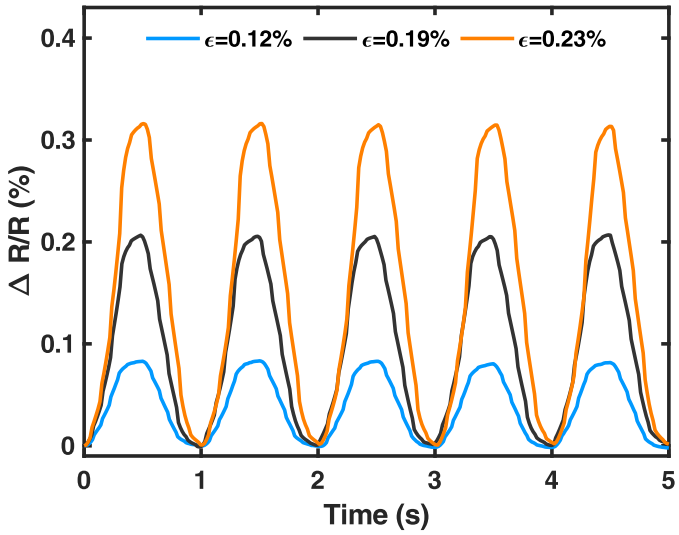

Figure 5.13 Relative resistance changes of the representative sensor GC-80 under different strain cycle at frequency of 1 Hz.

The sensor's high sensitivity, repeatability, and frequency resolution in detecting subtle dynamic strains make it well-suited for potential applications in wearable medical physiological signal monitoring and information transmission technologies (including

encrypted communications and voice recognition). Figure 5.14 presents the real-time pulse signal recorded by the sensor attached to a human wrist, with enlarged images of two pulse waves inserted, clearly displaying three typical main waves—percussion-wave, tidal-wave, and diastolic-wave, referred to as P, T, and D in the insert figure, demonstrating the sensor's capability to precisely distinguish key physiological signals.

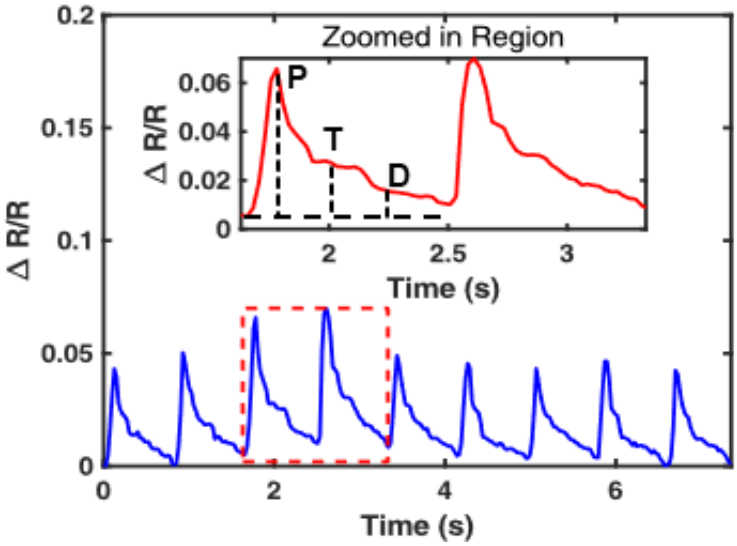

Figure 5.14 Real-time monitoring of human pulsation, and the inset shows enlarged pulse wave, consisting of three characteristic peaks

The sensor transmits Morse code by tapping (Figure 5.15). Letters are represented in Morse code as a series of dots and dashes, where a dot corresponds to a tap and a dash corresponds to pause. Each spike corresponds to a tap detected by the sensor, while the flat area represents a pause, matching the Morse code pattern for each letter of "POLYU". This demonstrates the sensor's ability to accurately distinguish between brief and sustained mechanical inputs, showcasing its high precision in detecting and

interpreting dynamic signals.

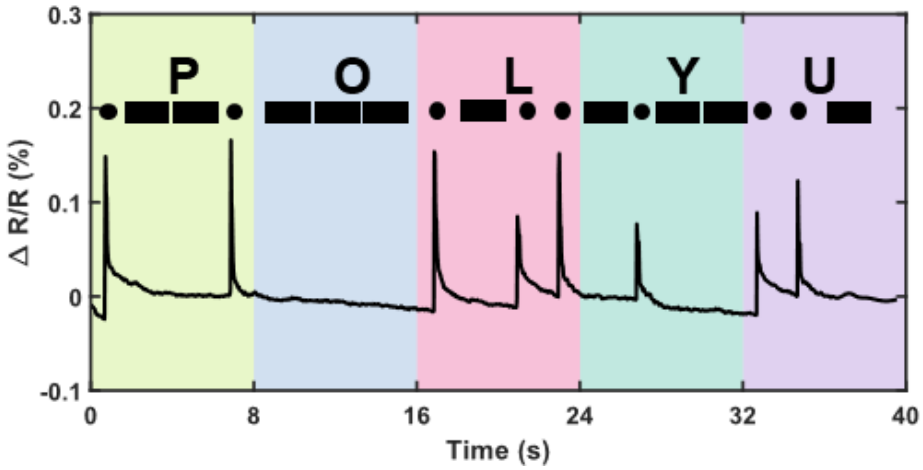

Figure 5.15 Relative resistance changes for Morse code of "POLYU" by tap sample (tap represents dot and pause represents dash)

Figure 5.16 presents the waveform signals of a drumbeat recorded simultaneously by the phone and the sensor. The time-domain signals of both recordings are found to be nearly identical. Additionally, short-time Fourier transform (STFT) analysis of the sensor's signal verifies that it accurately captures the corresponding time-domain waveform and successfully detects audio frequencies up to 1500 Hz. This demonstrates the sensor's capability to reliably record audio information with high fidelity in both the time and frequency domains.

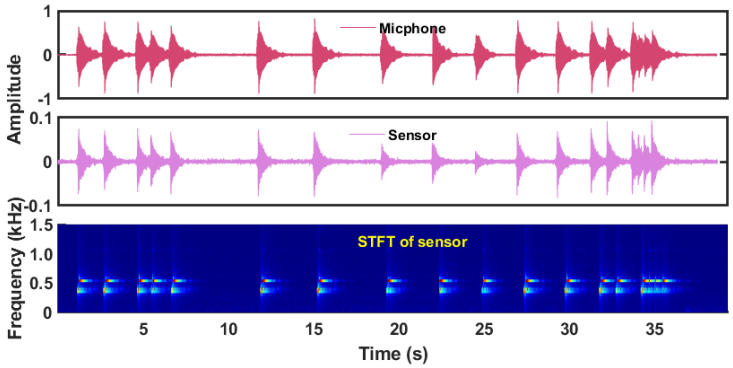

Figure 5.16 Acoustic waveforms recorded by a phone and sensor, and the STFT spectrogram corresponding to the sound waveform acquired by the sensor.

5.7 Sensing Performance of High-frequency

To assess the sensors on the ability of detecting high-frequency mechanical perturbations, sensors with varying weight ratios of graphene to CNCs (labeled GC-10 to GC-80, 20 mm × 10 mm) are printed on a GFRP laminate (200 mm × 200 mm × 1 mm) and tested for the response to tiny perturbations induced by UGWs propagating through the thin GFRP laminate at different frequencies (the experimental set-up in Figure 5.17). A 5-cycle hanning-window-modulated sinusoidal tone burst, generated by a waveform generator, with a central frequency ranging from 50 kHz to 400 kHz is amplified to 200 $V_{p\text{-}p}$ using a power amplifier to stimulate the actuator PZT wafer. The electrical resistance changes of the sensor are converted into a voltage signal, filtered and amplified through a self-developed amplification circuit, and then recorded on an oscilloscope.

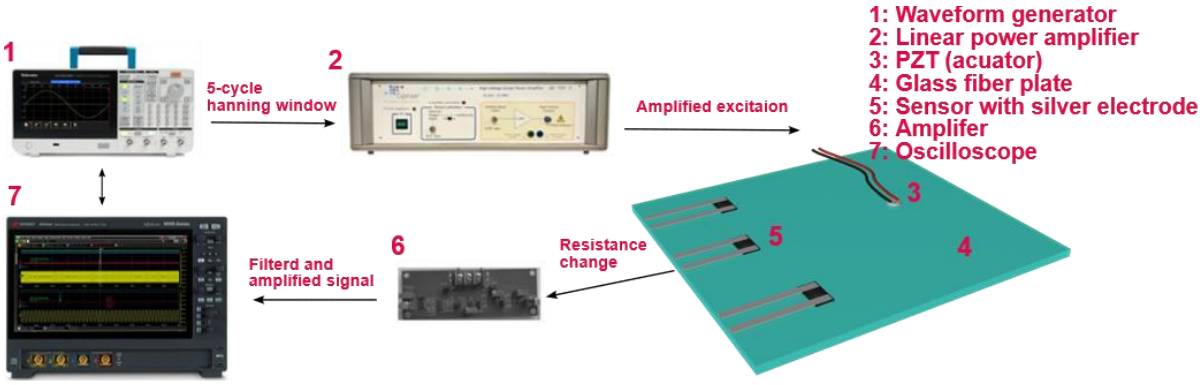

Figure 5.17 Experimental set-up of high-frequency UGWs test.

By analyzing the signal intensity and phase of the first wave component (the zero-order symmetrical Lamb wave denoted by S_0) to evaluating the performance of sensor at high-frequency response, Figure 5.18 shows the response signals of the sensors with varying ratios of graphene to CNC (labeled GC-10 to GC-80) to a representative frequencies of 150 kHz, and the signal of PZT serves as a reference baseline. A comparison of the typical 150 kHz ultrasonic signals collected by sensors and the PZT wafer reveal that the S_0 mode detected by sensors with balanced graphene concentrations (particularly GC-30, GC-40, and GC-50) arrives simultaneously with the PZT signal and without distortion, demonstrating the sensor's ultrafast, distortion-free response with no delay. In contrast, sensors with either lower or higher graphene concentrations (especially GC-10, GC-70 and GC-80) exhibit poor high-frequency response capabilities, a trend observed consistently across the other tested frequencies as well.

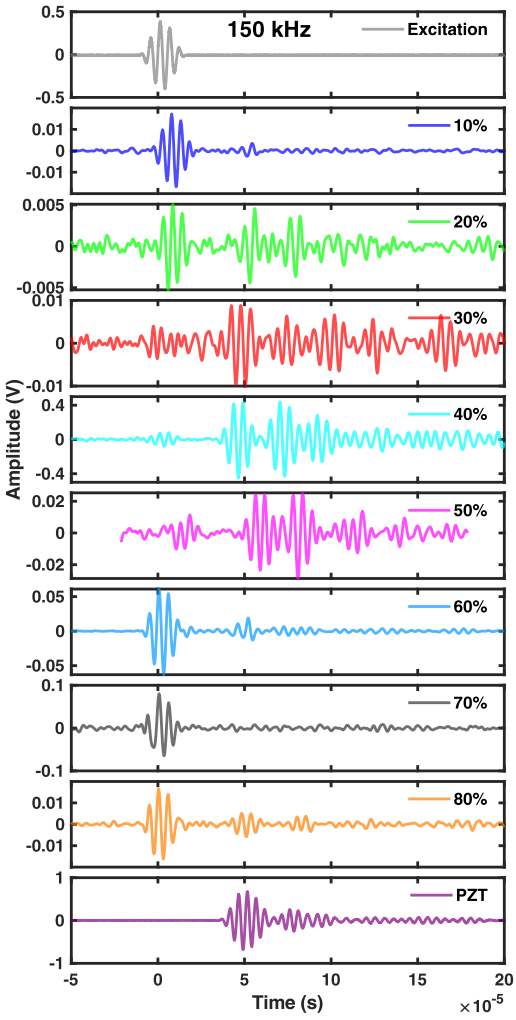

Figure 5.18 UGWs signals acquired sensors with different Graphene/CNCs ratio and surface-mounted PZT wafter under frequency of 150 kHz.

Figure 5.19 compares the amplitudes of the S_0 mode at different frequencies as captured by sensors with varying graphene contents. The amplitude of the S_0 mode of all sensors reaches the highest value at 150 kHz, which corresponds to the resonance frequency of the PZT actuator. The GC-40 exhibits the highest sensing ability at 50 kHz, 100 kHz, 150 kHz, and 200 kHz, with values of 0.048 V, 0.040 V, 0.490 V, and 0.085 V, respectively. Further, the spectra of the root mean square (RMS) values of signal

perceived by the sensors (GC-10 to GC-80) at different frequencies (Figure 5.20) indicates that GC-40 achieves the highest RMS value of 0.07 V at 150 kHz, demonstrating outstanding stability, signal density, and energy retention. These findings suggest that both excessive and insufficient CNCs content disrupt the delicate balance of graphene interlayer spacing required for tunneling current generation, ultimately impairing the sensor's sensitivity to ultrasonic waves.

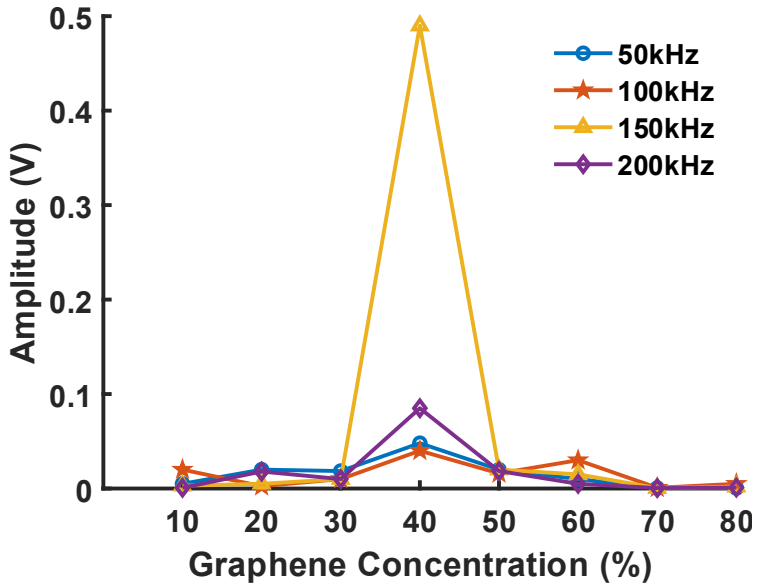

Figure 5.19 Amplitude value of S_0 received by Graphene/CNCs sensors with different graphene concentrations in response to 50 kHz to 200 kHz ultrasound.

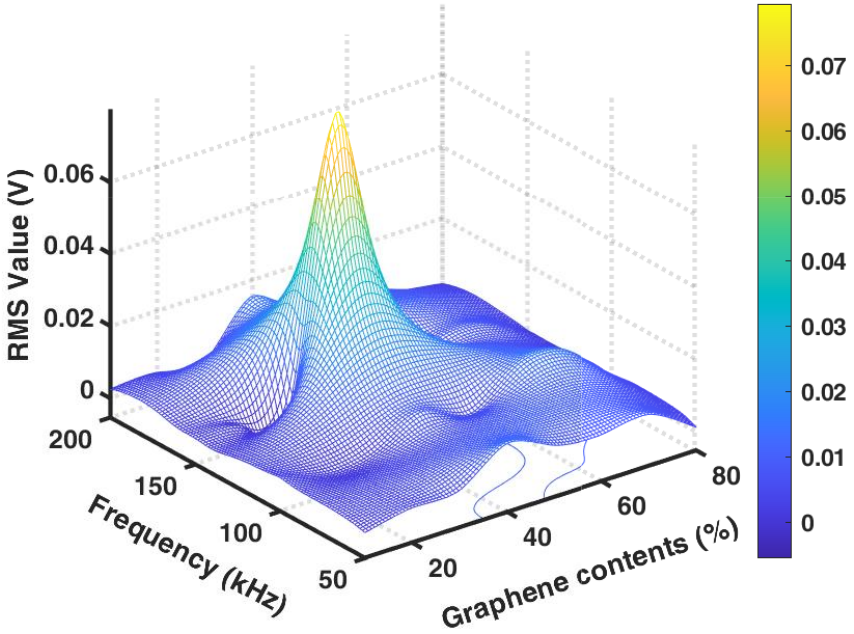

Figure 5.20 RMS values of signals collected by sensors with varying concentration ratios are measured across four distinct frequencies, 50 kHz, 100 kHz, 150 kHz, 200 kHz.

The time-domain signal is converted to the frequency domain using fast Fourier transform (FFT) to analyze the signal components at four representative frequencies—50 kHz, 100 kHz, 150 kHz, and 200 kHz. As shown in Figure 5.21, the spectral bandwidth of sensors aligns well with that of the excitation signal, confirming its ability to accurately capture propagated ultrasonic excitations. Among the tested sensors, GC-40 demonstrates a significantly larger amplitude spectrum, with the most pronounced advantage observed at 150 kHz.

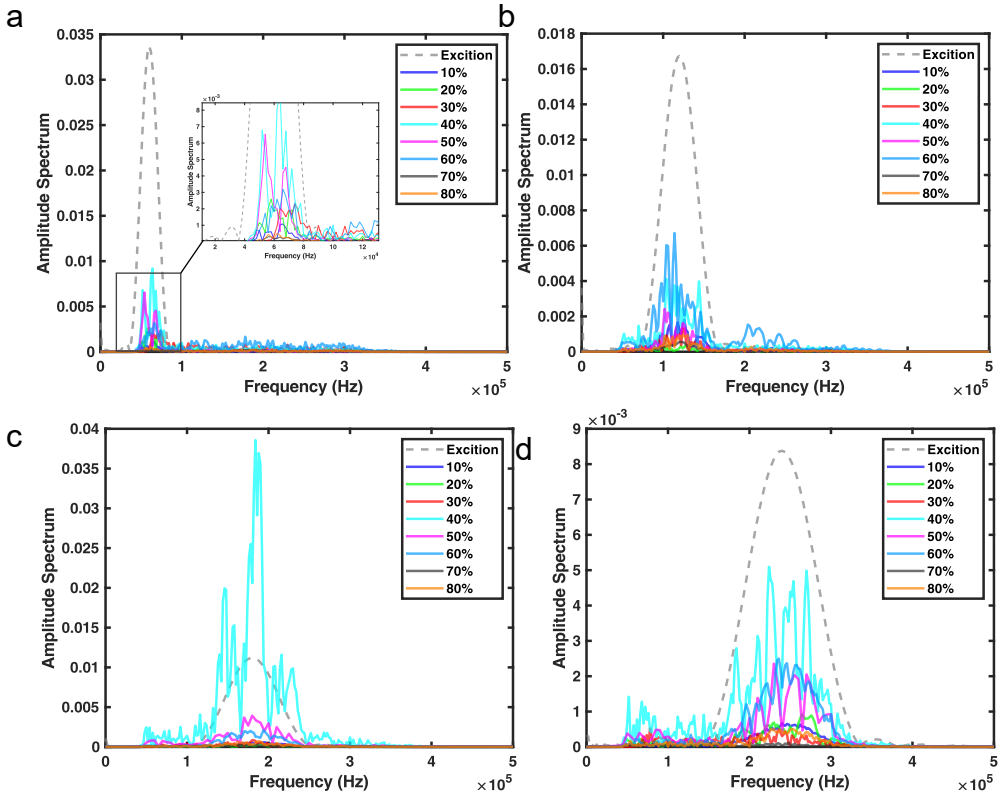

Figure 5.21 The corresponding frequency spectra of the signals in frequency of 50 kHz (a), 100 kHz (b), 150 kHz (c), 200 kHz (d).

GC-40 demonstrates outstanding performance in signal intensity, RMS values and signal-to-noise ratio (SNR) of 20.19 dB. These features have led to the extension of the upper limit response frequency of GC-40 to 400 kHz (Figure 5.22) with a fast response time of just 1.6 μs (Figure 5.23).

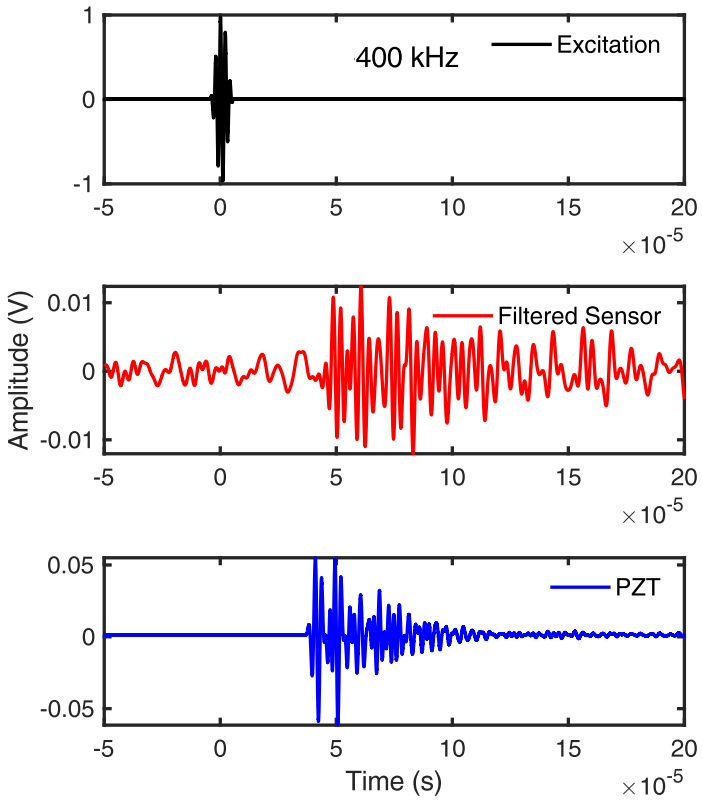

Figure 5.22 The response signal of GC-40 at frequency of 400 kHz.

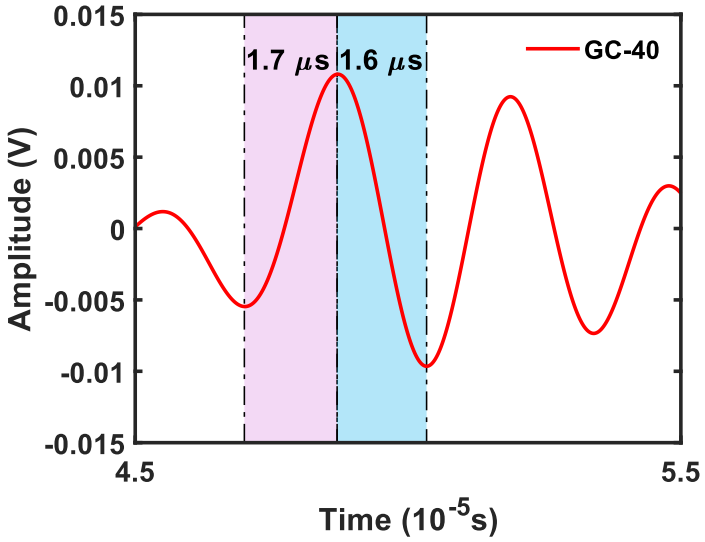

Figure 5.23 The response time of GC-40.

5.8 Summary

In this chapter, AJP is employed to fabricate graphene/cellulose nanocomposite strain sensors under pneumatic printing mode. Optimized parameters—including a sheath flow rate of 600 sccm, an atomizer flow rate of 600 sccm, a platform speed of 10 mm/s, a nozzle diameter of 300 μm, and a substrate temperature of 80°C—are identified to ensure uniform and reliable printing quality. The sensing performance is found to be strongly dependent on graphene concentration. At low strain levels (<0.1%), sensors with 40 wt% graphene exhibit the highest sensitivity, while at moderate strains (0.2–0.4%), 80 wt% sensors achieve gauge factors as high as 10. Leveraging this sensitivity, the sensors demonstrate the capability to detect subtle physiological signals, such as human pulse and throat vibrations. At higher frequencies, the 40 wt% sensors again show superior responsiveness and high SNR, enabling the detection of ultrasonic guided waves up to 400 kHz. These results highlight the broadband sensing potential of AJP-printed nanocomposite devices, spanning from low-frequency physiological monitoring to high-frequency ultrasonic applications. This establishes a foundation for subsequent chapters, where the sensors are extended to wearable acoustic recognition and SHM.

CHAPTER 6

Application of Aerosol Jet-Printed Sensor in Speech Recognition

6.1 Introduction

This chapter presents the development of a new flexible and biocompatible acoustic sensor utilizing graphene/CNCs, specifically engineered for dynamic acoustic sensing and speech recognition applications. The sensor and electrodes are additively manufactured using AJP and encapsulated with inherently adhesive, medical-grade PU film, to form a wearable device. The influence of graphene concentration on the sensitivity of the sensor to sound pressure levels (SPLs) is examined experimentally. The device can be adhered to the throat, to capture subtle vocal characteristics including timbre and rhythm accurately. In conjunction with the use of a machine learning algorithm based on the support vector machine (SVM), the device achieves an accuracy of 95.9% in recognizing digits from 0 to 9, showing potential to assist people with speech difficulties to communicate in a digital manner.

6.2 Preparation of Graphene/CNCs Acoustic Sensor

The sensor ink is prepared according to the procedure described in Section 5.2. The fabrication of the wearable acoustic device involves three main steps, as illustrated schematically in Figure 6.1a: (i) an inherently adhesive, medical-grade PU film (thickness ~40 μm) is tailored to the required size (100 mm×60 mm) and positioned on the printing platform of the aerosol jet printer, serving as the substrate; (ii) the sensor (20 mm×10 mm) and electrodes are printed on the designated areas of the PU substrate using a standard AJP process, employing a pneumatic atomization procedure using a printing nozzle of 300 μm in diameter, a sheath gas flow rate of 600 sccm, a atomizer flow rate of 600 sccm, a platform moving speed of 10 mm/s, and a consistent substrate temperature of 50°C; the sensing layer is printed in four passes, resulting in a total thickness of approximately 2 μm, with an interelectrode spacing of 10 mm; the light-cured electrodes and metal wires are electrically connected with conductive silver glue; (iii) on top of the printed sensor and electrodes an additional PU film is applied as a protective encapsulation. With that, a multi-layered wearable acoustic sensing device is fabricated (in Figure 6.1b,c).

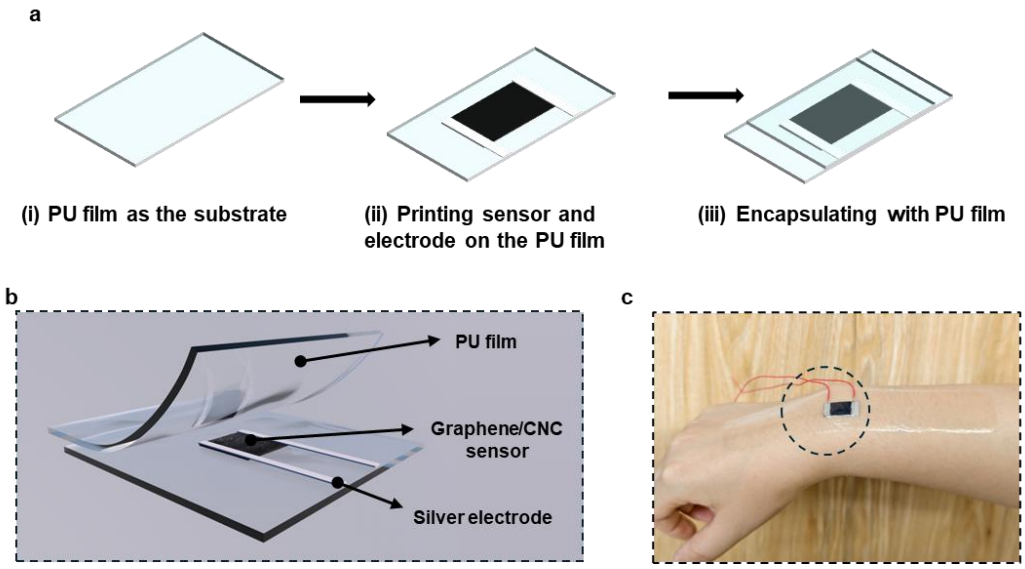

Figure 6.1 a Schematic diagram of the wearable acoustic device preparation process; b schematic of acoustic device; c device worn on the skin.

6.3 Acoustic Response

To evaluate the sensitivity of the sensor to subtle variation of sound field, a computer-controlled loudspeaker (YIJIA® 5757) emits multi-frequency audio signals, and the sensors which are printed on a glass slide and mounted on a custom fixture detect the vibrations induced by the sound field. A multimeter (Keithley® DMM7510) records the electrical resistance of sensor to each audio signal, providing a detailed assessment of its acoustic sensitivity. Figure 6.2a shows the obtained relationship between SPL in dB and captured the relative resistance change by sensors of different graphene concentrations, labeled GC-5 to GC-80. Here, SPL is defined as:

$$SPL = 20\log_{10}(\frac{P}{P_0}) \tag{6.1}$$

where P is the measured sound pressure, and $P_0 = 20\ \mu Pa$ the reference sound

pressure. As the SPL increases from 30 dB to 80 dB, there is a clear trend of increasing relative resistance change across sensors regardless of the graphene concentration, indicating that the sensors exhibit higher resistance changes in response to louder sounds. The sensitivity to sound (S), calibrated in terms of the slope of each curve, varies significantly between different graphene concentrations, defined as [196]:

$$S = \frac{\frac{\Delta R}{R_0}}{\Delta SPL} \tag{6.2}$$

where ΔR is the resistance change, R_0 the pristine resistance under no acoustic pressure, and ΔSPL the change in sound pressure level. Notably, sensors with graphene concentrations of 20% exhibit the highest sensitivity of 9.7×10^{-6} dB^{-1} within the SPL range of 30–80 dB, indicating that this concentration provides response to sound pressure with the highest sensitivity. In the meantime, when the graphene content is too low, as in GC-5, the sensor shows a high resistance (~300 kΩ) and a lower sensitivity of 1.7×10^{-6} dB^{-1}, due to the sparse conductive network where the inter-flake spacing exceeds the effective tunneling distance. Conversely, when the graphene content is too high (e.g., GC-70 and GC-80), the relative resistance change with increasing SPL becomes less pronounced, leading to reduced sensitivity despite higher conductivity. This phenomenon can be attributed to the structural characteristics of the conductive network at different graphene concentrations, which manifests different tunneling probability. The quantum tunneling resistance (R_c) arising from electron transport between adjacent graphene flakes can be described by the Landauer-Büttiker formalism [237, 238]:

$$R_c = \frac{h}{2e^2} \times \frac{1}{M\left[\Gamma + \frac{\pi^2}{6}(k_b T^2)\frac{d^2\Gamma}{dE^2}\Big|_{\mu}\right]} \tag{6.3}$$

where h is Planck's constant, e the charge of electron, M the number of percolation pathways in the polymer nanocomposite, Γ the tunneling probability between adjacent graphene flakes, E the fermi energy level, T the temperature, k_b the Boltzmann constant, and μ the electrochemical potential of graphene networks.

The tunneling probability (Γ) through the distance between adjacent graphene flakes can be quantitatively expressed via the Wentzel-Kramers-Brillouin (WKB) approximation [238-240]:

$$\Gamma = \begin{cases} \exp(-\frac{d_{vdw}}{d_{tunnel}}), & 0 \le d \le d_{vdw} \\ \exp(-\frac{d}{d_{tunnel}}), & d_{vdw} < d \le d_{cutoff} \end{cases} \tag{6.4}$$

where d is the distance of adjacent graphene flakes, d_{vdw} the van der Waals equilibrium separation (0.34 nm of graphene), d_{tunnel} the tunneling distance, and d_{cutoff} the tunneling cutoff distance. The analytical model reveals that the tunneling resistance exhibits distinct behavioral regimes governed by the distance of adjacent graphene flakes (d). When $d < 0$ (physical contact), the direct ohmic conduction dominates due to graphene flakes overlapping, resulting in a negligible contact resistance [212, 240]. When $0 \le d \le d_{vdw}$, the tunneling resistance stabilizes at a constant value as electron wavefunctions maintain coherent overlap through quantum confinement. In the pressure-sensitive operational range ($d_{vdw} < d \le d_{cutoff}$), the tunneling resistance demonstrates an exponential dependence on distance of adjunct

graphene flakes due to quantum tunneling modulation – the fundamental piezoresistive mechanism. Beyond the tunneling cutoff distance ($d_{cutoff} \leq d$), electron transport shifts to classical percolation pathways and no tunneling path can be formed [241, 242].

Figure 6.2b illustrates the tunneling path change of different graphene concentrations under the identical sound pressure. At a lower concentration (e.g., GC-10 or GC-20), the conductive network exhibits a sparse, loosely interconnected structural topology with most graphene flakes being separated by gaps within the tunneling distance ($0 < d \leq d_{cutoff}$), resulting in increased tunneling probability of sensor to external mechanical perturbation. When the sound vibrations propagate to the sensor, the sparse network undergoes significant disruption, leading to changes in the electrical resistance. In contrast, at a higher graphene concentration (e.g., GC-70 or GC-80, $d \leq d_{vdw}$), the denser conductive network results in fewer changes in electrical resistance under small-scale deformation, reducing the sensitivity of sensors. It is because the van der Waals forces between the graphene flakes promote an inert conductive network, limiting its responsiveness to sound pressure.

To further verify the effect of frequency on the sensing performance, the responses of the sensor (GC-20) to varying frequencies are examined under a constant excitation amplitude. The sensor is mounted on a glass-fiber cantilever beam and excited by an electrodynamic shaker (B&K® 4809) driven by a sinusoidal input [243]. The excitation signal is generated by a waveform generator (Tektronix® AFG31252) and amplified

through a power amplifier (B&K® 2718) and applied to the shaker. Figure 6.2c shows the resistance variations of the sensor at the same SPL (80 dB), as a representative, with different frequencies (from 10 Hz to 500 Hz). As observed, the relative resistance increases with frequency, reaching a maximum near ~150 Hz, and then gradually decreases at higher frequencies. This non-monotonic behavior, consistent with previous studies on acoustic sensors [196, 243, 244], arises from resonance effects within the sensor–substrate system. Notably, the peak sensitivity occurs in the low-frequency region that overlaps with dominant components of human speech (80–300 Hz), highlighting the suitability of the proposed sensor for acoustic sensing and speech detection applications.

Figure 6.2d shows the real-time response of the relative resistance change of GC-20 to an increased SPL from 50 dB to 80 dB with a step of 10 dB. As SPL increases, the sensor manifests a rise in relative resistance, with clear stepwise changes in response to the growing SPL. Specifically, the relative resistance increases from approximately 0.008% at 50 dB to about 0.015% at 60 dB, demonstrating the capacity of the fabricated sensor to resolve 10 dB SPL variations. Revealed by the figure, the SPL manifests a linear relationship between the relative resistance change, suggesting that the sensor is suitable for measurement and calibration of dynamic variation of acoustic signals.

The sensor exhibits excellent stability, as further validated by cyclic loading/unloading tests using mixed-frequency audio signals with SPL varied from 40 dB to 90 dB in 10

dB increments. As shown in Figure 6.2e, the impedance response after 100 cycles remains nearly identical to that of the first cycle, with negligible variations attributable to measurement error. This low hysteresis and high reversibility confirm that the sensor reliably preserves its structural and functional integrity under prolonged and fluctuating acoustic fields, which is critical for long-term, precise sound monitoring.

Figure 6.2f shows three waveforms obtained under repeated audio segments at an SPL of 80 dB, including the original signal from the loudspeaker, the waveform recorded by an iPhone microphone, and the waveform captured by the GC-20 sensor. The time-dependent waveform from our sensor closely matches both the original audio and the iPhone recording, demonstrating excellent agreement with a commercial acoustic sensor. Furthermore, repeated measurements under the same audio stimulus also reveal the outstanding repeatability of the sensor, as quantified by the standard deviations of the local maximum and minimum response values (0.035 and 0.0349, respectively), indicating negligible variation across trials. These results confirm that the sensor delivers both high-fidelity acoustic sensing and reliable performance consistency for continuous monitoring applications.

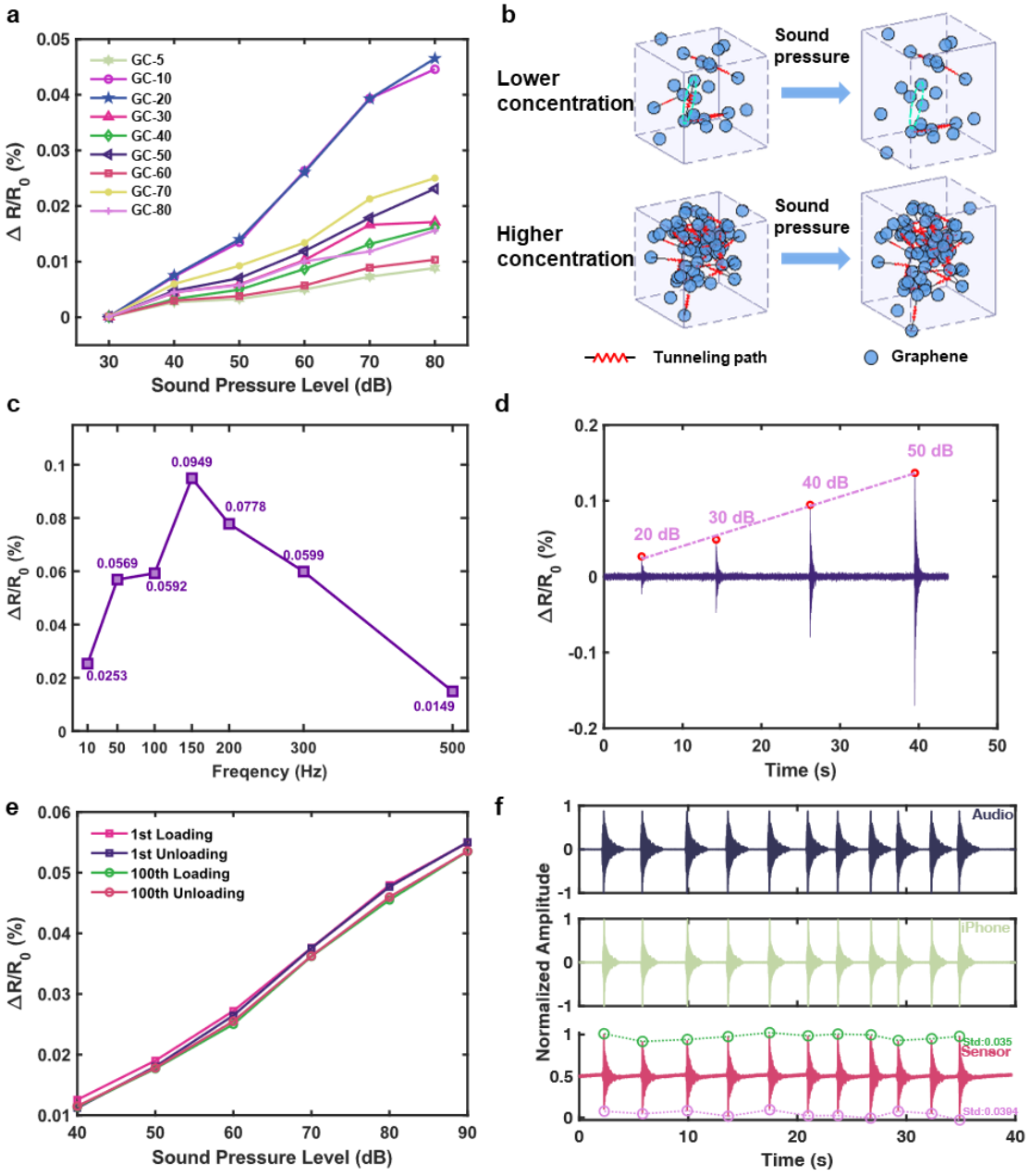

Figure 6.2 Acoustic response of sensor. a Response of sensors at varying sound pressure level; b schematic diagram of the change in tunneling path of sensors with lower and higher graphene concentrations under sound pressure; c frequency response of the GC-20 sensor under a representative SPL of 80 dB with different frequencies (from 10 Hz to 500 Hz);d real-time response signal of the sensor to the signal with gradually increasing sound pressure level; e relative resistance changes with 1st and 100th cyclic sound pressure level; f three acoustic waveforms from repeated playback of the same audio segment at 80 dB SPL: original loudspeaker signal, iPhone recording, and GC-20 sensor output.

6.4 Detection and Recognition of Speech

The integrated wearable acoustic device, fabricated through the AJP and encapsulated with inherently adhesive medical-grade PU film, forms a self-adhering epidermal interface that maintains robust skin conformability during dynamic articulatory movements, as functionally validated by its stable adhesion to the throat of the participant under the phonation tests, in Figure 6.3a.

Figure 6.3b presents the response signals of relative resistance change recorded by the acoustic device attached to the throat when three participants–a female adult, a male adult and a child, respectively pronounces a phrase of "Merry Christmas". The curves demonstrate distinct temporal patterns that reflect both the low-frequency and high-frequency components, corresponding to the movements of the throat and vibration of the vocal cords, respectively. The prominent low-frequency fluctuations observed in all three signals represent relatively strong displacement caused by the movement of the throat during speech production. This displacement is attributable to the shifting position of the larynx as the vocal cords adjust to produce different phonemes. This effect is particularly evident during transitions between words or syllables, where throats move to modulate pitch and airflow. Superimposed on these low-frequency fluctuations are relative weak high-frequency fluctuations, corresponding to the rapid vibrations of the vocal cords during sound production. These finer oscillations are

indicative of the fundamental frequency of the voice of speaker, reflecting their pitch and tonal qualities.

Figure 6.3c, d, e present, the time-domain signals of three English phrases— “The Hong Kong Polytechnic University”, “Hope everything goes well with you”, and “What a nice weather”, respectively, sensed by the acoustic device attached on the throat of a study participant. When the participant articulates each phrase, the acoustic device demonstrates distinct and measurable changes in electrical resistance corresponding to each phrase. Each phrase is recorded for four times, with the resulting signals showing almost identical patterns, highlighting the high stability and the repeatability of the acoustic device. By way of illustration, the response signal of the acoustic device and the audio signal recorded by a microphone in each phrase, are compared in Figure 6.3f, g, h. The waveforms of the acoustic device quantitatively match the upper envelope of microphone signal, demonstrating precise and consistent word-capture for different phrases and high fidelity in reflecting both the temporal and amplitude details. The absence of high-frequency components in the recorded signals of sensor, as illustrated in Figure 6.3h, is attributed to the limited sampling rate of the sensor acquisition system. Despite this limitation, the acoustic device remains high effectiveness in detecting and responding to sound signals, successfully capturing the key acoustic features necessary for speech recognition.

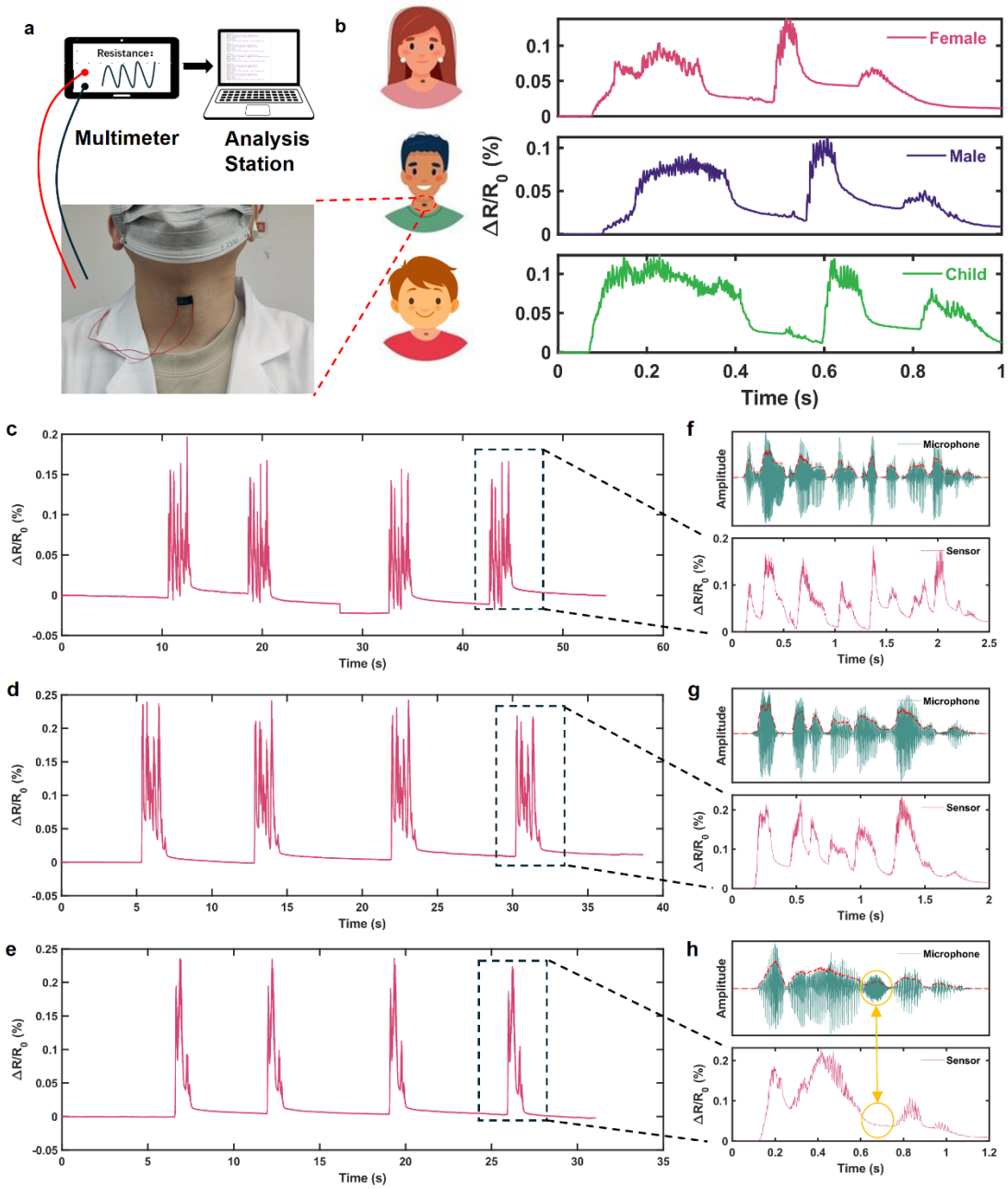

Figure 6.3 Acoustic device for voice detection. a Wearable acoustic device attached on the throat; b relative resistance change of the sensor when three different volunteers say, "Merry Christmas"; c-h relative resistance change of the sensor in response to three different sentences, compared with the microphone signal; c and f is the signal response of "The Hong Kong Polytechnic University"; d and g is the signal response of "Hope everything goes well with you"; e and h is the signal response of "What a nice weather".

The above tests demonstrate the capability of developing a wearable acoustic device in

distinguishing words of different individuals purely based on time-domain signals. This proves the potential of the acoustic sensor for achieving speech recognition, which can transmit communication information by decoding the vibration signals of the vocal parts of individuals with speech disorders, to facilitate communication in a digital manner.

To investigate the potential of the acoustic sensor for non-verbal speech recognition, a task of recognizing the digits is designed, where the acoustic device is mounted on a loudspeaker diaphragm to simulate articulatory movements of speech-impaired individuals. The acoustic device records vibration patterns corresponding to digits 0 to 9, collecting 50 samples per numeral, to establish a dataset containing 500 unique waveforms. Each digit exhibits distinctive time-frequency characteristics forming the basis for pattern matching, as illustrated in Figure 6.4a.

The recognition methodology (see workflow diagram in Figure 6.4b) implements a machine learning approach in conjunction with the use of SVM classification. The Radial basis function (RBF) kernel is selected for implementing the SVM, to effectively model nonlinear relationships within the dataset. The regularization parameter C is set to 10 to balance model complexity against generalization capability. The gamma parameter, determining the influence of the radius of individual samples, is configured in ‘scale’ mode (reciprocal of the product of the number of features and the variance of the input) to enhance robustness against feature scaling. This data-adaptive calculation

intrinsically scales the kernel function to the dimensionality and variance characteristics of the input data, reducing sensitivity to manual parameter tuning while maintaining model stability. Raw signals undergo pre-processing including: 1) Butterworth bandpass filtering for noise reduction, 2) amplitude-based segmentation of individual digits, and 3) categorical labeling. Subsequent feature extraction using Mel-Frequency Cepstral Coefficients (MFCCs) with their first and second derivatives, creating feature vectors that are normalized. The dataset is partitioned into 80% training data for SVM model optimization and 20% testing data for validation. The confusion matrix is shown in Figure 6.4c, which shows that the acoustic device achieves recognition of digits 0 to 9 with a high accuracy of 95.9% over 100 testing data sets. In an actual test - when a loudspeaker presents continuous input simulating the sequence “007”, the system correctly segments and identifies all three digits through this SVM model, as shown in Figure 6.4d. It empowers individuals with vocal impairments to perform vital actions such as calling emergency services or conveying simple messages and improves quality of life by enabling them to express basic needs and intentions effectively.

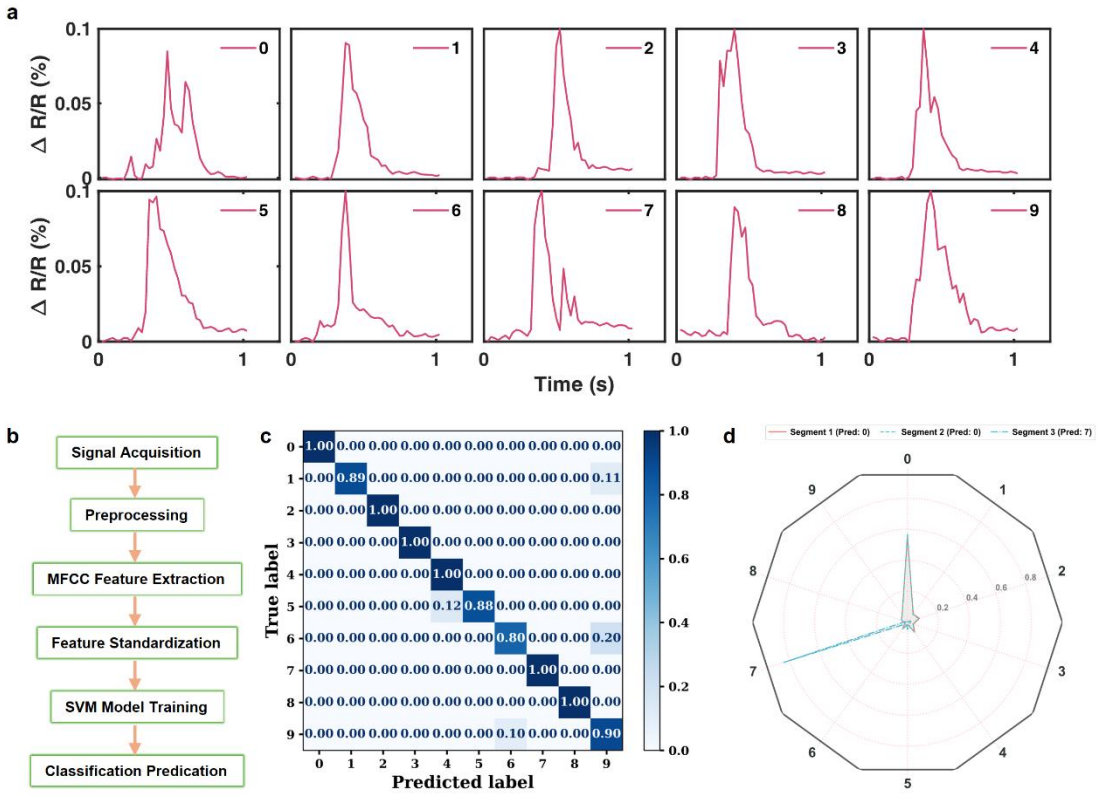

Figure 6.4 Acoustic devices for digits 0-9 recognition. a Signal of digits from 0 to 9 captured by sensor; b schematic flowchart of speech recognition; c classification confusion matrix of digits 0-9 prediction versus the test data set; d recognition of a sequence of digits "007".

6.5 Summary

In this study, a new piezoresistive graphene/CNCs acoustic sensor is successfully fabricated using AJP, with a PU film encapsulation to enhance flexibility and skin conformity. The sensors with 20 wt.% of graphene concentrations (GC-20) exhibited the highest sensitivity of 9.7×10^{-6} dB^{-1} and a minimum resolution for SPL change of 10 dB, thus enabling precise acoustic detection. Additionally, the sensor exhibits low hysteresis and excellent reversibility when subjected to SPLs ranging from 30 dB to

90 dB. It also demonstrates strong reproducibility across repeated measurements: the standard deviations of the local maximum and minimum responses are only 0.035 and 0.0349, respectively. Further, the wearable acoustic device is attached to the throat of a participant and reliably captures vocal cord vibrations, allowing for accurate detection of speech patterns, variations in tone, and distinct audio signals. Moreover, we train the SVM model based on machine learning that can successfully recognize spoken digits from the signal captured by the sensor with the accuracy of 95.9%, demonstrating its ability to interpret the semantic content of speech signals. These results illustrate the capability in detection and recognition of sensors, paving the way for broader adoption in communication technologies for individuals with speech impairments.

Looking ahead, training models on larger and more diverse datasets could enable recognition of more complex speech patterns, extending beyond digits to entire words and phrases, thereby broadening the application scope in human–machine interaction, healthcare, and accessibility technologies.

CHAPTER 7

Application of Aerosol Jet-Printed Sensor in Structural Impact Assessment

7.1 Introduction

Engineering structures subjected to harsh environments are vulnerable to fatigue and impact damage, necessitating reliable SHM. While piezoelectric transducers have long been used for GUW detection, their brittleness and poor conformability limit deployment in complex or corrosive settings. Nanocomposite sensors, formed by dispersing conductive nanofillers into polymers, offer lightweight, flexible, and highly strain-sensitive alternatives, yet conventional mechanisms struggle to capture the ultrahigh frequency and nano strain amplitudes characteristic of GUWs. Recent advances highlight tunneling-dominated conduction as a key mechanism, whereby resistance changes exponentially with nanometer-scale filler separation, enabling unprecedented sensitivity and broadband detection. Since Section 5.7 evaluations have demonstrated that the GC-40 formulation exhibits superior high-frequency dynamic performance and high sensitivity to ultrasonic guided waves, this composition is selected for the present study. In this chapter, these sensors are manufactured via AJP technologies onto flexible circuits and subsequently embedded within composite

structures, thereby enabling seamless integration and real-time monitoring of external impacts. Leveraging these advances, nanocomposite sensors have demonstrated gauge factors far exceeding traditional strain gauge, positioning them as promising candidates for impact localization and next-generation SHM.

7.2 Preparation of Graphene/CNCs Sensor Units

The sensor ink is prepared according to the procedure described in Section 5.2. Flexible circuit substrates are designed to integrate the nanocomposite sensor (GC-40), with the circuit dimensions and patterns shown in the corresponding Figure 7.1. The deposition of the sensing material is carried out via aerosol jet printing, employing a pneumatic atomization procedure with a 300 μm diameter nozzle. The printing parameters are set as follows: sheath gas flow rate of 600 sccm, atomizer flow rate of 600 sccm, and a platform moving speed of 10 mm/s. To ensure stable deposition, the substrate was maintained at a constant temperature of 50°C during the printing process.

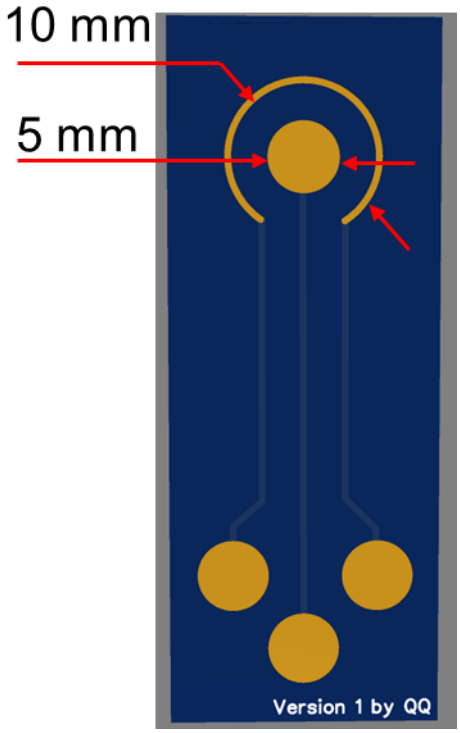

Figure 7.1 Schematic diagram of flexible electrodes.

The sensing layer is printed in four consecutive passes, yielding a total film thickness of approximately 2 μm. Following deposition, the substrate is heated to 50°C to promote curing and enhance adhesion between the sensing layer and the flexible circuit. The final structure consisted of circular sensing units with a diameter of 10 mm, precisely aligned with the predefined areas of the flexible circuits (Figure 7.2).

Figure 7.2 Photographic diagram of the printed sensor unit.

7.3 Fabrication of Composite with Sensor Networks

To evaluate the performance of the prepared sensors, sensors are embedded into GFRP laminates for impact localization testing. Glass fiber prepregs (Easycomposites® XA120-GPL-150) are first cut into sheets with dimensions of 250 × 250 mm using a precision cutting machine (AOL® AOL-1313). The laminates are then fabricated via a lay-up process, consisting of a total of eight prepreg layers, as shown in Figure 7.3. Four sensing units are embedded within the laminate by positioning them on the surface of the fourth layer, forming a predefined sensor network as illustrated in Figure 7.4. The coordinate information of four sensors is listed in Table 7.1. The remaining prepreg layers are subsequently stacked on top to encapsulate the sensing units.

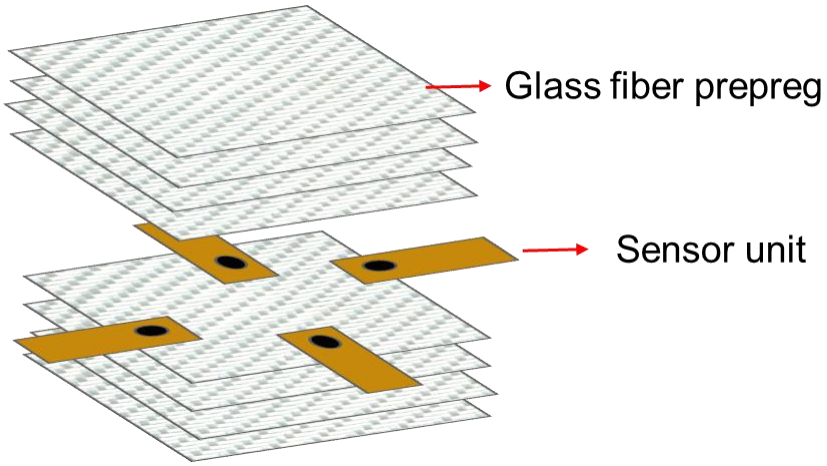

Figure 7.3 The schematic of GFRP with embedded four sensor units.

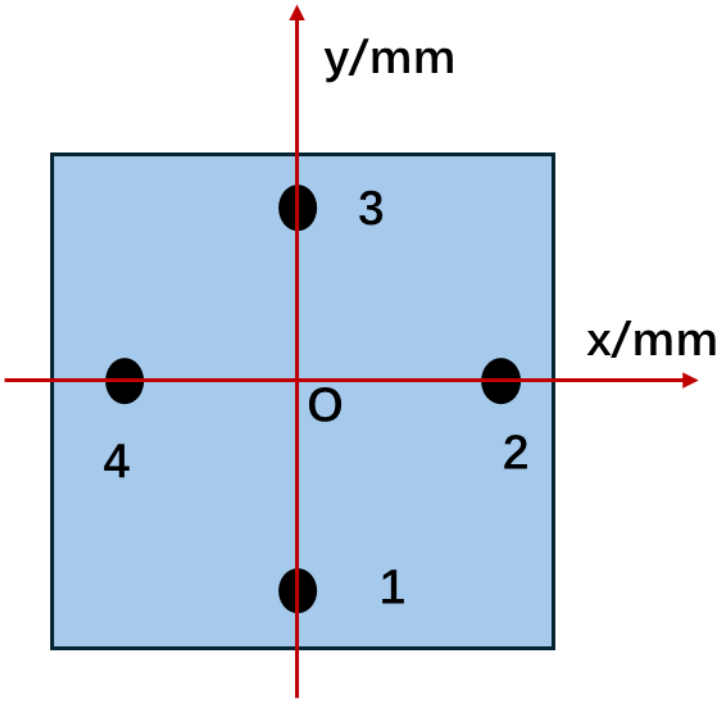

Figure 7.4 Schematic of GFRP with sensor network.

Table 7.1 Coordinates of the sensor networks.

Sensor NO.	x/mm	y/mm

1	0	-105
2	105	0
3	0	105
4	-105	0

The lay-up assembly is enclosed within a vacuum bag and evacuated to a pressure of −30 inHg to ensure uniform consolidation. The structure is then cured in an oven at 120°C for 100 minutes according to the manufacturer's specifications. This process yields a consolidated composite laminate with integrated sensing units, enabling in situ monitoring and localization of impact events. To provide a suspended configuration for subsequent testing, the cured composite plate is mounted onto an aluminum frame using sealing adhesive, leaving a gap of approximately 1 cm between the laminate and the supporting aluminum plate, as illustrated in Figure 7.5.

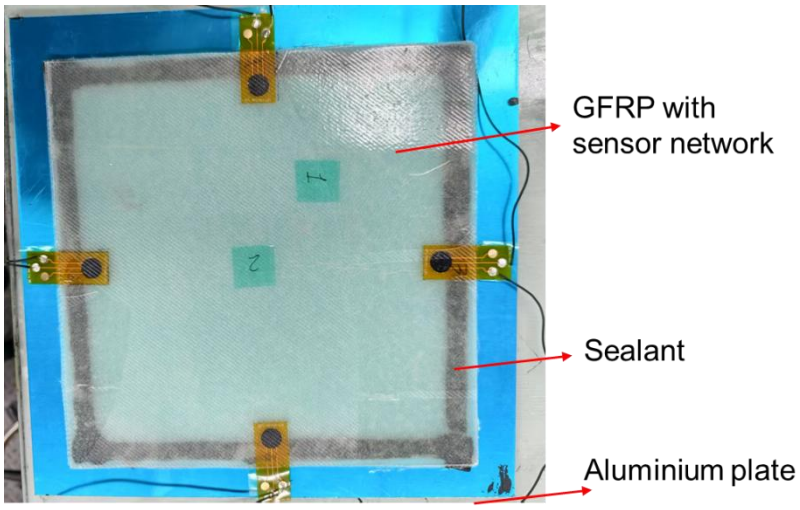

Figure 7.5 Photographic diagram of GFRP with sensor network.

7.4 Evaluation of Sensors under Impact

A wide frequency response range is crucial for accurately capturing and reproducing complex signals. However, most piezoresistive sensors examined in previous studies [145, 245] fail to meet the stringent requirements for high-frequency signal monitoring in the aviation industry. Aircraft wings, in particular, are highly susceptible to damage from accidental impacts, which pose significant risks to flight safety [246, 247]. The high-frequency sensitive sensors developed in this study provide new ideas for solving the above problem.

To validate the capability of the embedded sensors to capture impact events, an initial experiment is conducted in which a 32 g steel ball is dropped from a height of 10 cm at the GFRP. A PZT sensor is mounted adjacent to the embedded piezoresistive sensor to provide a reference signal. The output from the embedded sensor is amplified using a signal conditioner before being acquired by an oscilloscope, while the PZT signal is directly recorded using the same oscilloscope.

The acquired signals show clearly that the impact-induced elastic waves are successfully detected by both sensors. As shown in Figure 7.6, the arrival times of the waveforms obtained from the embedded sensor and the PZT sensor are highly consistent, demonstrating the rapid response and high temporal resolution of the flexible embedded sensing system. The experiment is repeated multiple times, and no

degradation in performance is observed, confirming the robustness and durability of the sensor—highlighting a significant advantage over conventional brittle sensing elements.

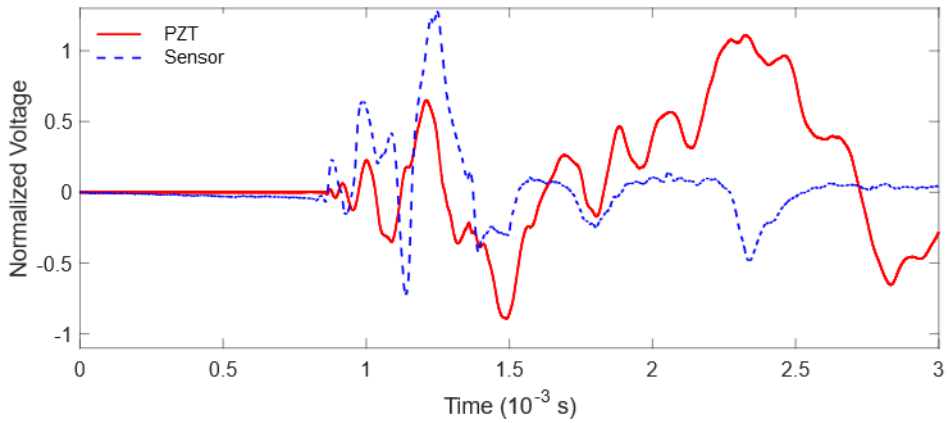

Figure 7.6 Comparison of the impact response of the sensor and PZT.

Following this initial validation, an experiment is carried out to evaluate the capability of the distributed sensor network in localizing impact events. The perturbations generated by the impact are sequentially captured by sensors at different locations (Figure 7.4), with arrival times corresponding to their respective distances from the impact point. Differences in waveform characteristics among the sensors are attributed to sensor positions and wave scattering from structural boundaries, as shown in Figure 7.7.

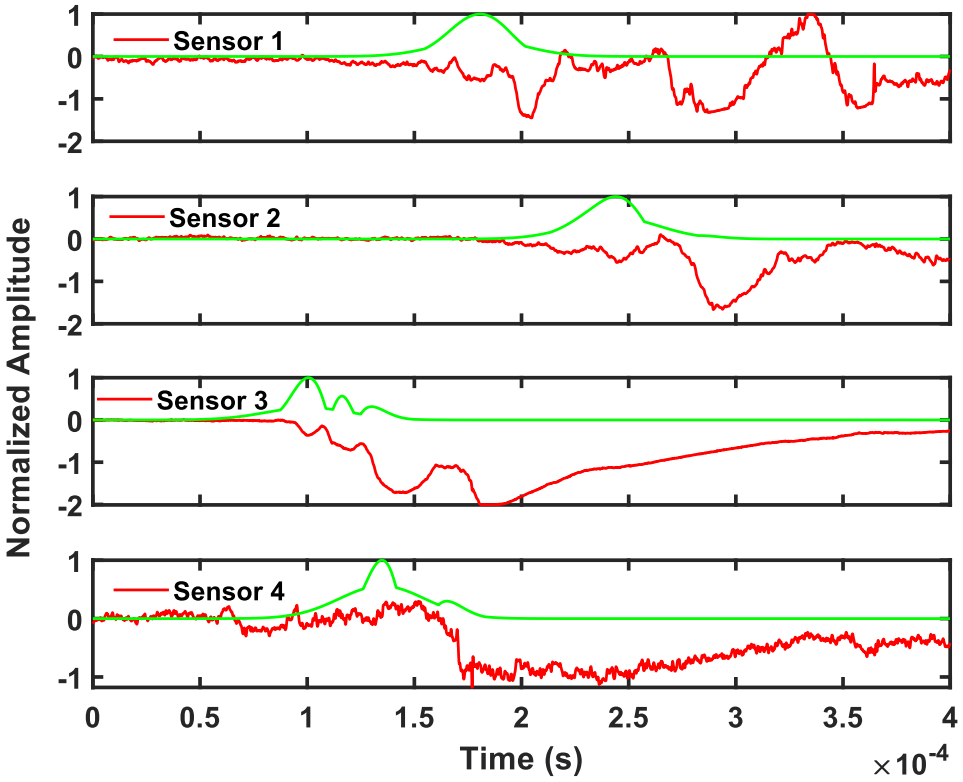

Figure 7.7 Impact signals acquired by four sensors.

The Time-Delay-of-Arrival (TDOA) algorithm is a widely used method for localizing impact events by measuring the arrival time differences of wave signals at multiple spatially distributed sensors. The key idea is that when an impact occurs, it generates elastic waves that propagate outward. These waves reach sensors at different times depending on the distance between the impact location and each sensor. By calculating the differences in arrival times between pairs of sensors, one can determine hyperbolic loci of possible impact positions. Each time difference corresponds to a hyperbola, where the two sensors act as foci. The true impact point lies at the intersection of all such hyperbolas formed from all sensor pairs. This method does not require knowledge of the exact time the impact occurred—only relative differences in wave arrival times

matter. When enough sensors are used, these intersecting hyperbolas converge on a single point, allowing accurate localization of the impact.

Assume the impact event occurs at an unknown position (x, y), and that N sensors P_1, P_2, ..., P_N are deployed at known positions (x_i, y_i), where $i = 1, 2, ..., N$. The wave travels at a (possibly direction-dependent) speed v_i from the assumed impact point to each sensor P_i.

For any two sensors P_i and P_j, the measured time delay Δt_{ij} is:

$$\Delta t_{ij} = t_i - t_j = \frac{d_i}{v_i} - \frac{d_j}{v_j} = \frac{\sqrt{(x-x_i)^2 + (y-y_i)^2}}{v_i} - \frac{\sqrt{(x-x_j)^2 + (y-y_j)^2}}{v_j} \quad (7.1)$$

where t_i and t_j are the arrival times of the impact wave at sensor P_i and P_j, v_i and v_j are the wave propagation velocities from assumed impact point to sensor P_i and P_j. Each value of Δt_{ij} defines a hyperbola with foci at P_i and P_j, and the actual impact point must lie somewhere along this hyperbola.

An enhanced TDOA algorithm, developed based on this principle and accounting for the anisotropy of wave velocity, can map the sandwich structure into a 2D pixel-valued image. The pixel value reflects the probability of the impact point being at that location. By analogy, two sensors form a sensor pair and are mapped into a 2D pixel-valued image. In this process, the signals representing the 2D pixel-valued images have been normalized to achieve amplitude correction in different propagation directions.

Ultimately, the images obtained from each two sensors in the sensor network are multiplied to create a synthesized image, whose pixel value I(x, y) is expressed as

$$I(x,y)=\prod_{i=1}^{N-1}\prod_{j=i+1}^{N}\left[E_{t_i(x,y)+\Delta t_j(x,y)}+E_{t_j(x,y)+\Delta t_i(x,y)}-1\right] \tag{7.2}$$

where E_t is the normalized signal envelope at time t, $\Delta t_i(x,y)$ is the theoretical propagation delay from (x,y) to sensor P_i. The pixel value $I(x,y)$ represents the likelihood of the impact originating from that position. Multiplying all sensor pair contributions highlights regions where time-delay predictions align consistently.

By applying the TDOA, the impact location and energy are quantitatively identified with good accuracy. It can be observed in Figure 7.8 that the location and severity of impact damage are precisely localized and evaluated with acceptable errors using a spare sensor network with only four sensors. Meanwhile, a higher pixel value can indicate a higher probability of the location of impact.

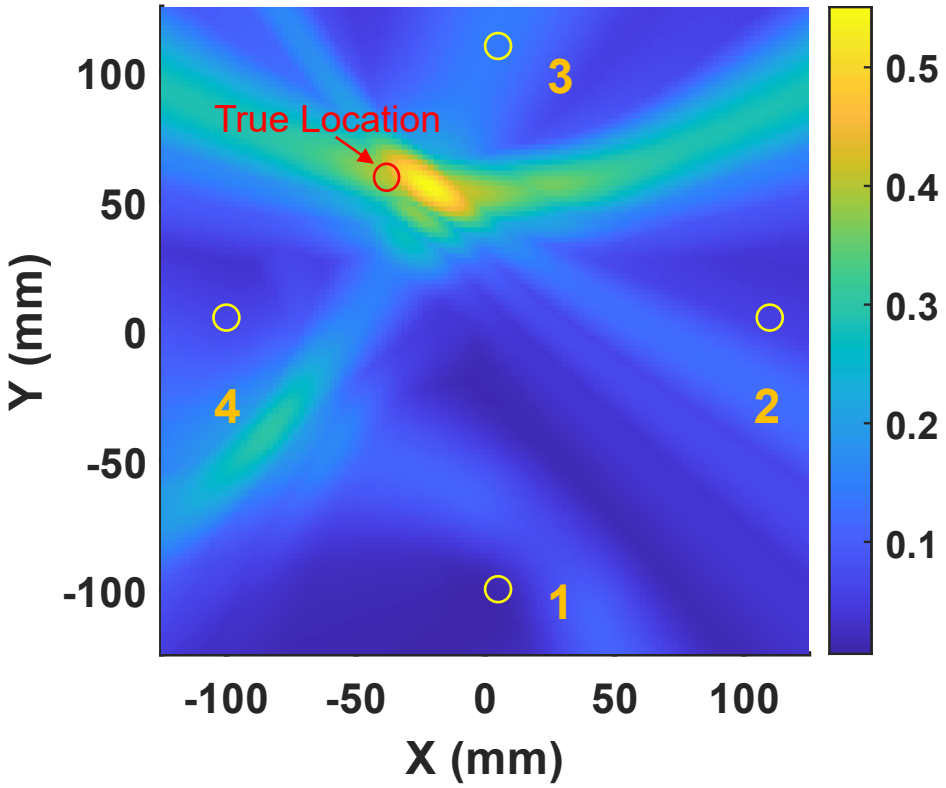

Figure 7.8 Comparison between the identified and real point of impact using signals captured by the printed sensors.

7.5 Summary

In this chapter, a graphene/CNCs nanocomposite sensor network was designed, fabricated, and embedded into GFRP laminates to enable real-time structural impact monitoring. The sensors were manufactured via AJP onto flexible circuits, forming uniform sensing units with stable conductivity and sensitivity. By embedding these units into the mid-plane of composite laminates, a distributed sensing network was established without compromising structural integrity. Impact experiments confirmed that the embedded sensors could not only capture high-frequency elastic waves with

accuracy comparable to conventional PZT transducers but also withstand repeated loading without degradation. Furthermore, the integration of a TDOA-based algorithm allowed the network to localize impact positions with good precision, demonstrating the feasibility of nanocomposite sensors as lightweight, flexible, and durable alternatives for next-generation SHM applications.

While embedding printed nanocomposite sensors into GFRP laminates demonstrates the feasibility of lightweight, flexible, and durable impact monitoring, the approach still relies on conventional composite manufacturing processes that involve complex lay-up sequences, mold customization, and co-curing steps. Such procedures limit scalability and design flexibility for multifunctional systems. To overcome these constraints, the next chapter advances the concept of "totally-additive-manufacturing," in which both the structural framework and the sensing network are fabricated in a fully integrated manner through multi-material 3D printing. This strategy eliminates the need for traditional molds and assembly, paving the way for multifunctional composites with seamless structural and sensing integration.

CHAPTER 8

“Totally-additive-manufacturing” - functionalized CFRP Composites

8.1 Introduction

This chapter presents the development of a novel manufacturing framework based on the concept of “totally-additive-manufacturing”. From printing the CFRP composite structure using FDM to the fabrication of sensing networks using AJP, the entire manufacturing process is completed with hybrid printing, without interference from the operators. Micromorphological analysis and interlaminar shear strength test have confirmed that the “totally-additive-manufacturing” warrants adequate interfacial bonding among different components of the AM-fabricated composites. By regulating the printing parameters, the AJP-made sensing network can be optimized, whereby to maximize its sensitivity to dynamic strains in a broad frequency regime from quasi-static to up to 200 kHz.

8.2 Material Preparation

The materials used for developing the “totally-additive-manufacturing”-functionalized CFRP composites include (i) FDM-printed continuous carbon fibers, (ii) nylon-based

matrix and electrical insulation layers, and (iii) an ultrathin, AJP-fabricated piezoresistive sensing network made with a specifically formulated graphene/CNC nanocomposite ink, as well as the silver ink-based electric circuits.

8.2.1 Filaments (for CFRP Composites)

The FDM-printed CFRP composites consist of nylon filaments and continuous carbon fiber filaments. The nylon filament (Markforged® Onyx™), which is infused with short carbon fibers and 1.75 mm in diameter, serves as the matrix of the composites and also the insulation medium between the conductive carbon fibers and the sensing network. The continuous carbon fiber filament (Markforged® Carbon Fiber FR), as the reinforcement of the composites, is formed with carbon fiber bundles infused with a sizing agent, with ~1,000 carbon fibers in each bundle. The diameters of each carbon fiber bundle and individual fibers are 0.35 mm and 0.008 mm, respectively, as observed using SEM [51]. Both the nylon and continuous carbon fiber filaments are stored in a sealed dry box to prevent moisture absorption.

8.2.2 Nanocomposite Ink (for Sensing Unit)

A nanocomposite ink is formulated for fabricating the sensing units of the network with AJP, based on the authors' previous work [248, 249]. The ink is formulated by mixing 0.1 g graphene (TIME NAN® TNERGO-50) (50 μm in diameter, < 3 layers, and > 95% purity) with 0.1 g CNC (ScienceK® CNCs) (~10 nm wide and ~200 nm long) in the 30 ml solvent of hybridizing DI water and ethyl alcohol with a weight ratio of 1.5:1. Such a ratio ensures smooth jetting of ink without causing gas line blockages. The mixture is

then mechanically stirred at 500 rpm for 20 hours at room temperature (25℃), followed by 1-hour of sonication in an ultrasonic bath to ensure uniform dispersion of graphene/CNC ink. The graphene/CNC ink manufacturing process is illustrated schematically in Figure 8.1. Thus-tailor-made ink can trigger the quantum tunnel effect when the distance between the two neighboring graphene sheets is smaller than the critical threshold (typically several nanometers), enabling the sensing unit to capture dynamic strains induced by cyclic loads or elastic perturbation applied on the sensing unit. The viscosity of the ink measures 3.218 cP (RheoSense® microVISO), which is suitable for AJP.

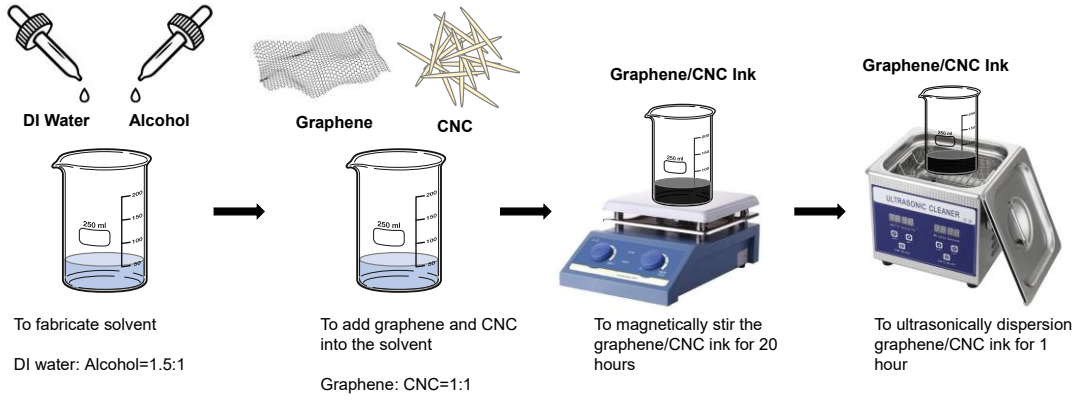

Figure 8.1 The flowchart of fabricating graphene/CNC ink.

8.2.3 Conductive Silver Ink (for Electric Circuits)

A commercial silver nanoparticle ink (NOVACENTRIX® JS-A221AE) is acquired for printing electric circuits of the sensing network via AJP. This water-based ink, containing 50 wt.% silver, is specifically formulated to have a viscosity of 10-20 cP and an average particle size of 35 nm via ultrasonic atomization, conducive to AJP. The ink can be cured using either heating- or light-based methods, and in this study, the latter is adopted to avoid potential damage to the nylon-based substrate caused by a

heating process. Upon completion of the curing, the silver circuits exhibit a volume resistivity of 9.1×10^{-6} Ω^{-cm}.

8.3 "Totally-additive-manufacturing"-driven Fabrication

With the materials prepared in the above, the fabrication process of the "totally-additive-manufacturing"-functionalized CFRP composites primarily involves i) the printing of CFRP composites using FDM, and ii) the printing of the sensing network (including sensing units and silver circuits) using AJP at designated interlayers of the CFRP laminate.

8.3.1 Making CFRP Composites Using FDM

The CFRP composites are continuously printed on a 3D printing platform (Markforged® Mark Two) with a motion range of 320 mm×132 mm×154 mm, at a room temperature (25°C). The printing process is divided into two steps: extruding matrix (nylon) and extruding continuous carbon fiber, each through a separate printing head, as illustrated in Figure 8.2a. The carbon fiber layering and orientation are configured using the commercial software Eiger™. The height of both the carbon fiber layer and the nylon layers remains at 0.125 mm, ensuring good consistency at the interfaces between the two layers. The printer bed is pre-treated with a layer of adhesive to immobilize the initial layer.

8.3.2 Making Sensing Network Using AJP

The sensing units and silver conductive circuits are printed on an aerosol jet 3D printing platform (Optomec® AJP300). To preserve the layered structure of graphene in the nanocomposite ink, pneumatic atomization is selected to atomize the prepared nanocomposite ink, while ultrasonic atomization is used to atomize the silver ink. Because the use of two different atomization modes avoids cleaning the pathways during the printing process, facilitating the "totally-additive-manufacturing"-driven process. To avoid graphene aggregation, the nanocomposite ink is continuously stirred with a magnetic stirrer at 500 rotations per minute throughout the printing process. The build platform is kept at 80°C to rapidly evaporate the solvent composed of DI water and ethyl alcohol in the ink. A pulsed light system (XENON® Model X-1100) is used for curing of the silver ink, rather than thermal curing to avoid possible damage to the CFRP composites due to the use of a high temperature (>200°C). The printing parameters that may affect the geometry and quality of sensing unit include the atomizer flow rate, sheath flow rate, and stage speed. These parameters are investigated and discussed in Section 5.4. To avoid nozzle clogging, the sheath gas is injected into the nozzle via a sheath channel, which accelerates the atomizer flow rate in the channel and minimizes the possibility of ink amalgamation at the nozzle, as illustrated in Figure 8.2b. With this, the atomized ink, enveloped and accelerated by the sheath gas stream, is deposited on the designated interlayer of the CFRP laminate in a desired pattern.

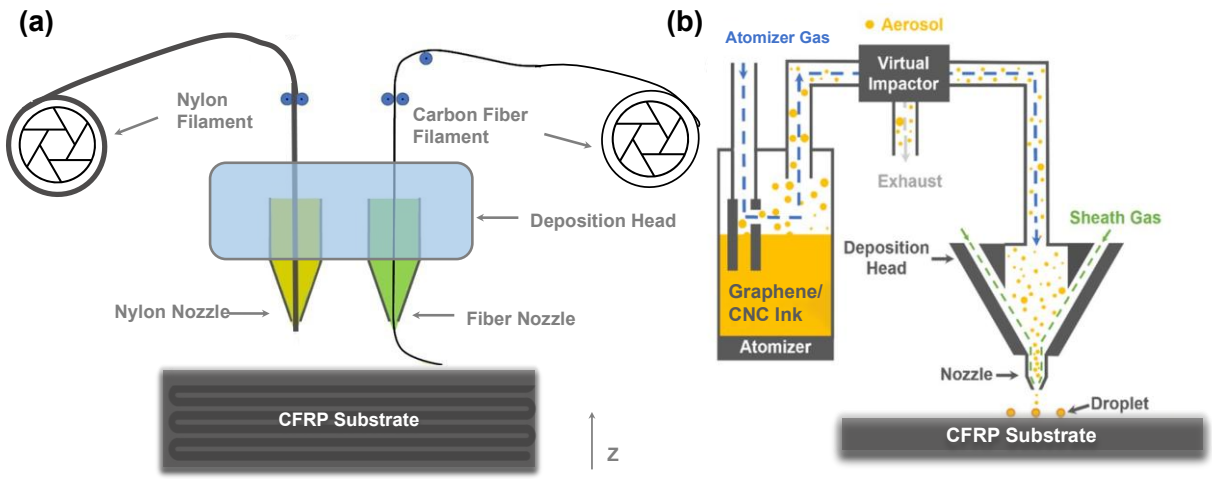

Figure 8.2 Schematic diagram of two AM methods: (a) FDM for continuous fiber printing; (b) AJP for sensing network printing.

8.3.3 "Totally-additive-manufacturing"-functionalized CFRP Composites

To recap, the fabrication of functionalized CFRP composites using the concept of "totally-additive-manufacturing" includes four key steps, as elaborated in Figure 8.3a using the manufacturing of a 4-layer cross-ply CFRP laminate ($[90/0]_S$) as an example:

1. To print continuous carbon fiber and nylon filaments using FDM: nylon filaments are deposited onto the build platform to form the nylon matrix with a thickness of 0.5 mm, followed by layering the continuous carbon fiber filaments along the 90 and 0 degree (the first and second carbon fiber layers, see Figure 8.3b) on the nylon matrix. To electrically insulate the graphene/CNC sensing units from the conductive carbon fiber layers, an additional nylon layer is printed on the top of the carbon fiber layer, serving as an insulating layer, as highlighted as the "lower nylon insulation layer" in Figure 8.3b.
2. To deposit nanocomposite ink using AJP for making sensing units: the above FDM printing process is paused, and then the nanocomposite ink is jetted onto

specific locations on the lower nylon insulation layer precisely (in Figure 8.3b), forming individual sensing units of the sensing network.

3. To deposit the silver ink using AJP for making circuits: the silver ink is deposited on the lower nylon insulation layer in the desired pattern, to network individual sensing units and form a sensing network. The deposited silver ink undergoes light curing by exposing it to a 5-minute of illumination at a frequency of 1 Hz with a pulse intensity of 836 J.
4. To resume nylon and carbon fiber filament printing: the first step resumes, and an additional nylon layer is printed (indicated as "upper nylon insulation layer" in Figure 8.3b) to encapsulate the AJP-made sensing network, together with the lower nylon insulation layer. Subsequently, the continuous carbon fibers are printed along the 0 and 90 degree (the third and fourth carbon fiber layers as seen in Figure 8.3b), followed by the printing of the final nylon layer.

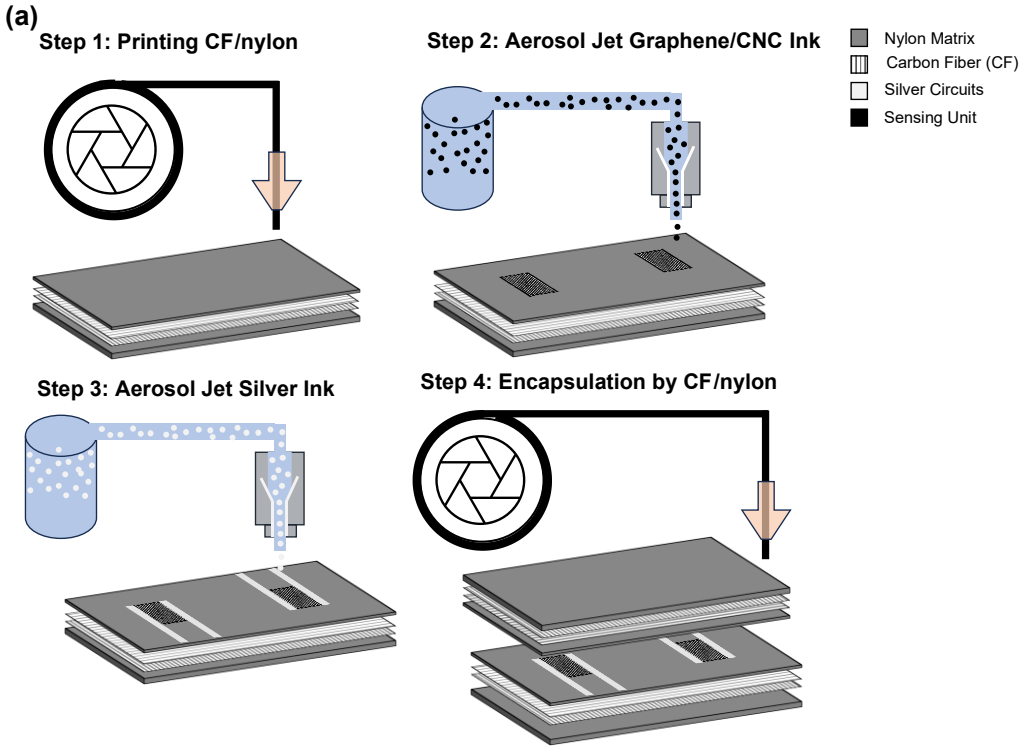

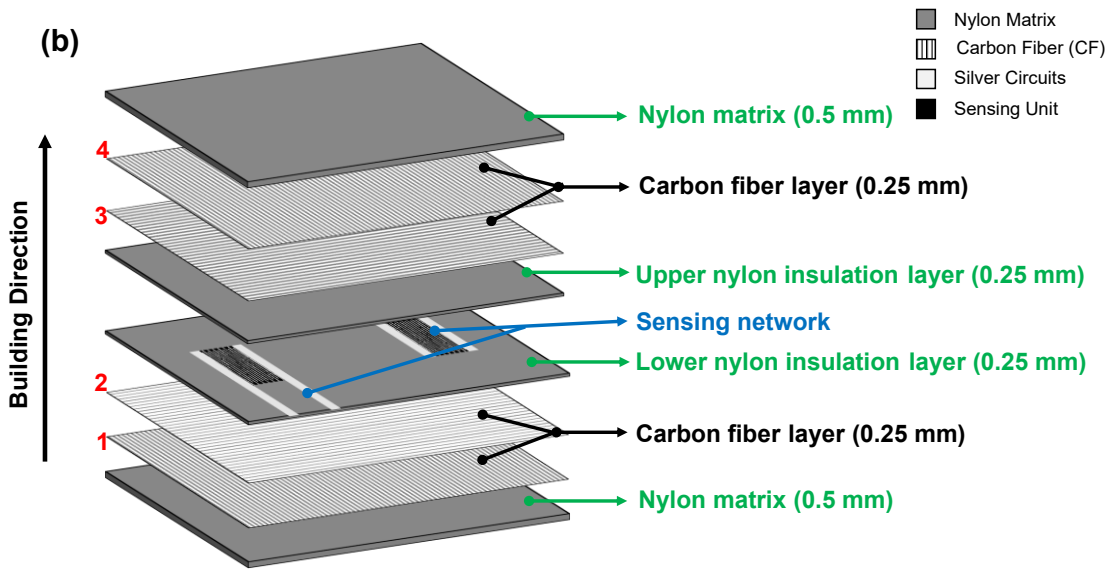

Figure 8.3 Schematic of the concept of "totally-additive-manufacturing"-functionalized CFRP composites: (a) the printing process; (b) exploded illustration of the printed functionalized CFRP composites, including the thickness and sequence of each layer.

8.4 Morphological and Performance Characterization of Sensing Units

8.4.1 Morphology

The microscale morphology of the printed sensing units is scrutinized using SEM (TESCAN® Vega 3) Figure 8.4a, to observe a uniform and well-dispersed distribution of graphene/CNC without observable agglomeration. This homogeneous dispersion is crucial to establishing a stable and sensitive conductive percolating network within the nanocomposite ink. At a smaller scale, in Figure 8.4b, CNCs are observed to uniformly disperse in graphene sheets with a stable microstructure, benefiting the formation of a densely packed electrically conductive network in the sensing units and triggering the tunneling effect.

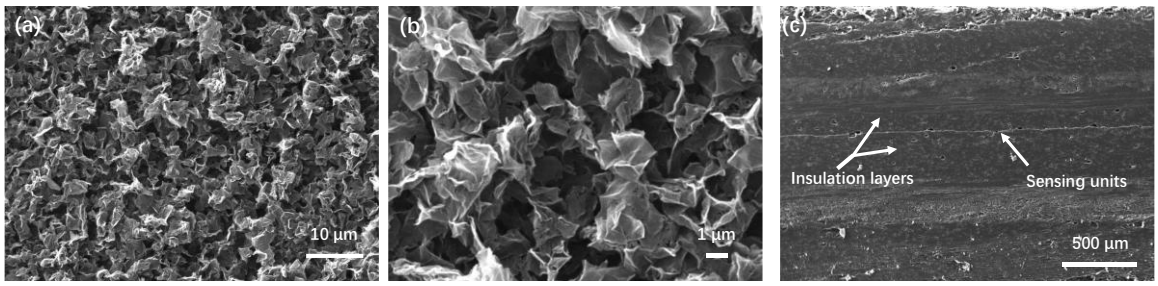

Figure 8.4 Morphological characterization by SEM images: (a) and (b) the graphene/CNC sensing unit at two different scales; (c) cross-sectional view of the functionalized CFRP composites with embedded sensing unit.

8.4.2 Electrical Properties

To ascertain the correlation between the number of printed passes (the number of times to repeat the same printing path) and the electrical properties, graphene/CNC samples of different printed passes from 1 to 6, are printed on a glass slide, each measuring 2 mm × 10 mm. Each sample is electrified with a pair of silver electrodes. An optical profiler (KLA® ZetaTM-20) is employed to measure the thickness of each sample, and the electrical resistance is gauged using a dynamic digital multimeter (Keithley® DMM 7510) with a two-probe method.

The average thickness and resistance of the printed graphene/CNC sensing units of different numbers of printed passes are shown in Figure 8.5. As noted, the average thickness increases nonlinearly against the number of printed passes, because the surface topography becomes rougher with the increase of printed passes, affects the ink deposition on the surface. In contrast, the resistance decreases with the increase in the number of printed passes. The resistance drops rapidly till the pass number reaches 4 and saturates afterward. This can be attributed to the fact that the graphene/CNC ink

printed in four passes features a uniform and stable conductive network in the microstructure of the sensing unit, as evidenced by the reduced deviation in resistance change (error bar shown in Figure 8.5).

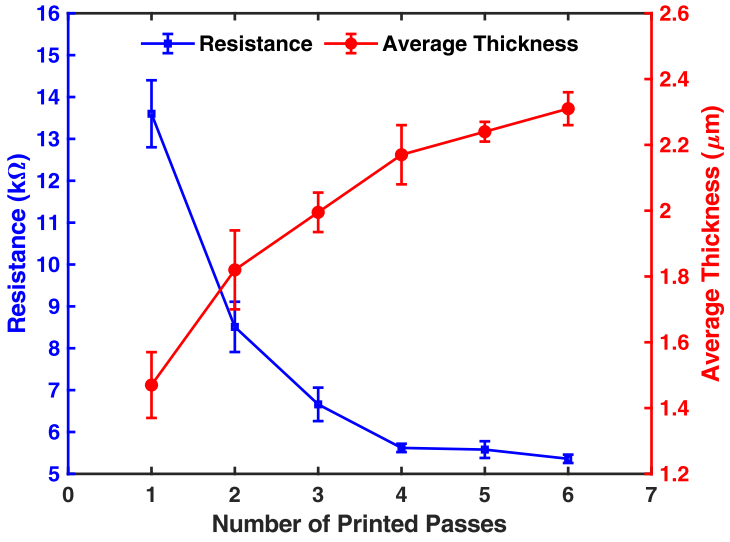

Figure 8.5 Average thickness (red) and electrical resistance (blue) of the printed graphene/CNC sensing unit against the number of printed passes.

8.5 Interfacial Properties

It is important to evaluate the potential degradation to the integrity of the "totally-additive-manufacturing"-functionalized CFRP composites, due to the embedment of the sensing network.

8.5.1 Morphology Analysis

The cross-sectional image of the CFRP composites is obtained via SEM (TESCAN® Vega 3), in Figure 8.4c, showing the interface between a sensing unit (printed with four passes) and the insulation layers. The image reveals an explicit, intact boundary

between the sensing unit and the upper and lower nylon insulation layers, without any delamination phenomenon.

8.5.2 Interlaminar Shear Strength (ILSS) Evaluation

Two groups of CFRP samples, five for each, fabricated respectively with and without the AJP-fabricated sensing network, are prepared using "totally-additive-manufacturing" approach. ILSS is calibrated for each sample in both groups, in accordance with the ASTM D2344 standard on a three-point bending testbed (MTS® Alliance RT/50). Here, ILSS, F_{SBS} (MPa), is calculated as

$$F_{SBS} = \frac{0.75P_m}{bh} \tag{8.1}$$

where P_m (N) is the maximum load during the test b (mm) the measured specimen width, and h the measured thickness of the specimen. The test results are compared in Figure 8.6 for two groups of samples, to note that the ILSS for CFRP composites without an AJP-made sensing unit falls in a range from 12.42 to 15.81 MPa, while the "totally-additive-manufacturing"-functionalized CFRP composites show an averaged ILSS between 13.43 and 14.35 MPa. The average ILSS of the CFRP samples without sensing units and the functionalized CFRP samples with sensing units are 13.916 MPa and 14.004 MPa, respectively, representing a slight difference of 0.63% between these two sample groups. Such discrepancies can be attributed to the inherent errors produced from the printing and testing process. It implies that the embedded sensing unit commits an ignorable effect on the interfacial integrity of CFRP composites.

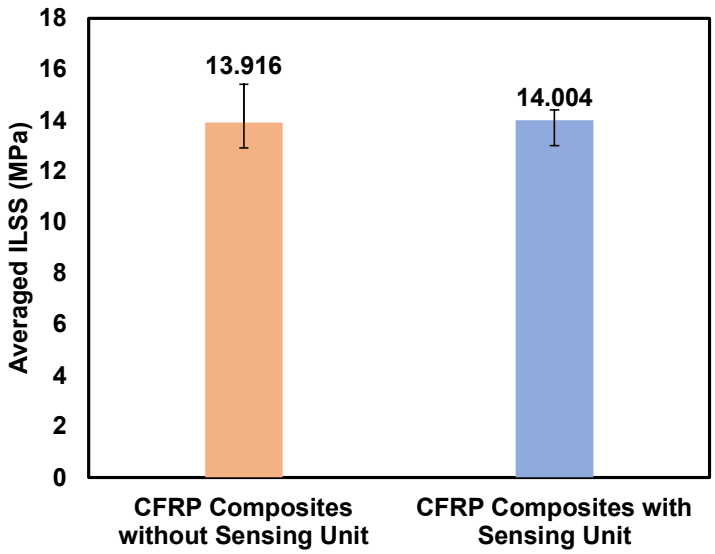

Figure 8.6 Averaged ILSS of two groups of CFRP samples prepared with and without sensing network.

8.6 Sensing Performance

The self-sensing performance of the "totally-additive-manufacturing"-functionalized CFRP composites is examined, through measuring quasi-static strains of the CFRP composites, and acquiring high-frequency GUWs propagating in the composites.

8.6.1 Quasi-static Strains

Low-frequency dynamic tests are conducted on the CFRP composites at varying magnitudes and frequencies. The functionalized CFRP composites, with a dimension of 175 mm×25 mm×2 mm, are fabricated following the procedure as outlined in Section 8.3. A sensing unit, measuring 20 mm×10 mm×1.2 μm, with silver electrical electrodes is printed at the center of the lower nylon insulation layer, as shown in the exploded sketch and prototypes in Figure 8.7a and b. To ensure a secure and stable connection

between the printed silver electrodes on the sample and the multimeter, the screw electrical connection is adopted, in the insert of Figure 8.7a and c. The measurement set-up, pictured in Figure 8.7c, includes a universal testing system (INSTRON® 5982) equipped with a 1 kN load cell for applying tensile load on the sample, a digital multimeter (Keithley® DMM7510) for recording the relative resistance changes of the sensing unit through the two-point method, and a computer for recording and analyzing data.

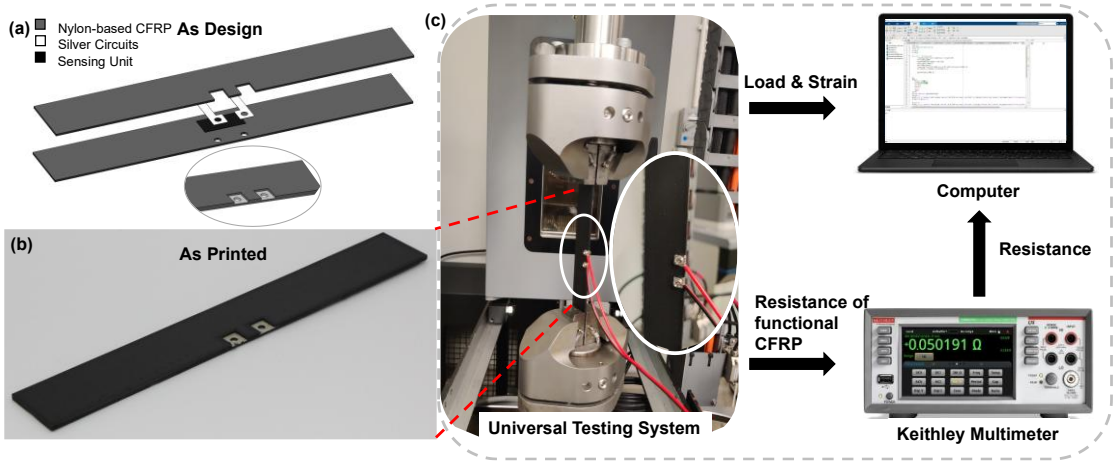

Figure 8.7 The low-frequency dynamic tests: (a) exploded illustration of the sample; (b) prototype; (c) pictured experimental set-up.

The relative resistance change of the functionalized CFRP composites subjected to applied tensile strains is shown in Figure 8.8, manifesting a proportional relationship between the tensile strain and relative resistance change over a strain range from 0 to 0.32%. The gauge factor (K) of the sensing unit, which defines its measurement sensitivity, is calculated as Formula 3.1. The gauge factor of the sensing unit is measured to be ~2.1 and ~6.8, respectively when the strain is in the range of 0 to 0.12% and in the range of 0.12% to 0.32%.

The strain of the sample under the low-frequency dynamic tests with the sinusoidal tensile strain of 0.15%, at varying frequencies from 0.2 to 0.8 Hz, is shown in Figure 8.9, demonstrating a consistent strain-acquisition performance. The relative resistance of the sample responds quickly and accurately replicates applied strain within this frequency range. A secondary peak appears in the unloading stage of each cycle, as observed in Figure 8.9. This is due to the existence of interlayer gaps of the printed CFRP composites and the sensing unit [250], which results in an uneven force transmission during unloading.

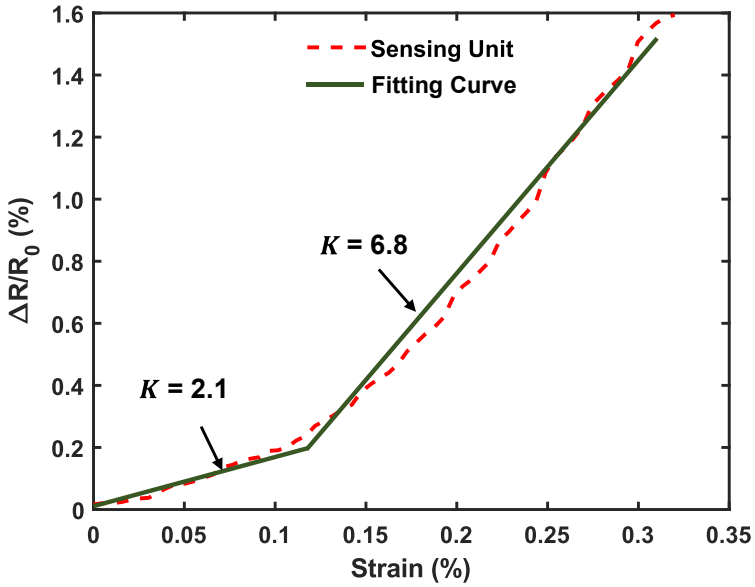

Figure 8.8 Relative resistance changes under quasi-static strain range from 0 to 0.32%.

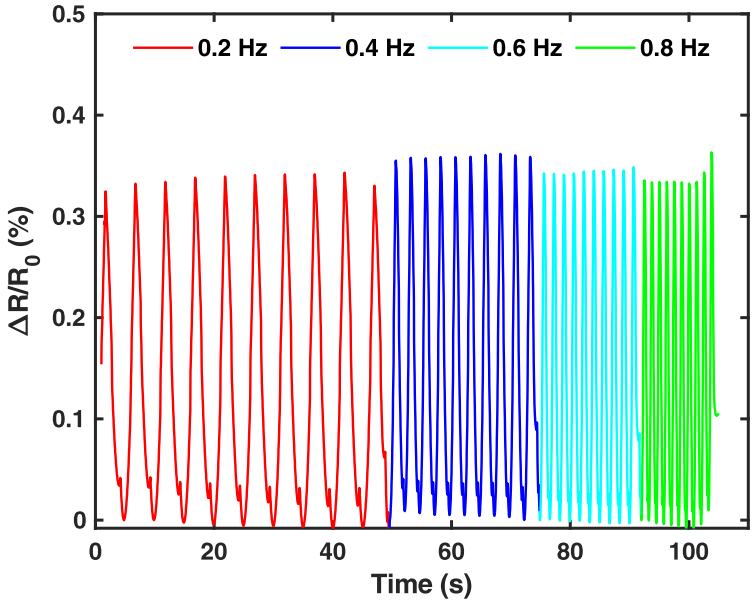

Figure 8.9 relative resistance changes under different testing frequencies at a constant strain of 0.15%.

8.6.2 High-frequency GUWs

The above quasi-static dynamic tests are further expanded to an ultrasonic frequency domain up to 200 kHz. The functionalized CFRP composite sample with a sensing network consisting of four sensing units, measuring 200 mm×120 mm×2 mm and produced following the steps detailed in Section 8.3, is shown in Figure 8.10a-c. To generate GUWs into the sample, a PZT wafer (Φ: 10 mm; thickness: 1 mm) is surface-mounted on the sample, with its position highlighted in Figure 8.10d. For signal calibration, another PZT wafer (Φ: 10 mm; thickness: 1 mm) is also glued on the surface of the sample, in Figure 8.10d, to be used as the GUWs sensor.

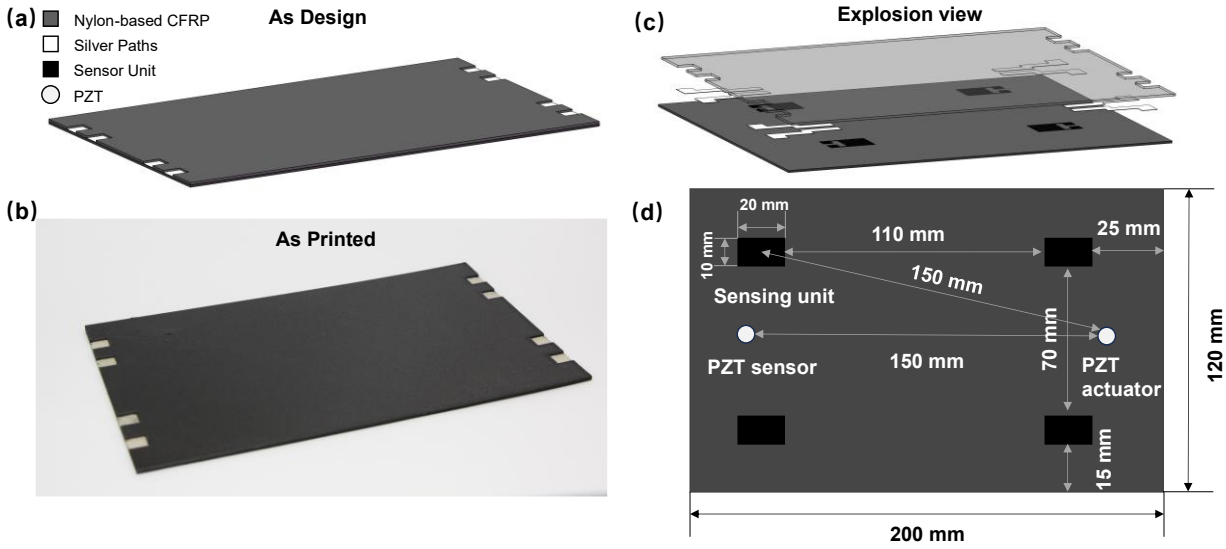

Figure 8.10 Illustration of the functionalized CFRP laminate of high-frequency GUWs tests: (a) design; (b) prototype; (c) exploded illustration of the sample; (d) the position of sensing units (embedded), and two PZT wafers (respectively as the actuator and sensor, surface-mounted).

An ultrasonic testing system is configured, as illustrated in Figure 8.11a. In the system, different circuits are designed for PZT wafers and the sensing units, respectively, which are isolated from each other, to avoid possible interference. Shielded cables are used to minimize electromagnetic coupling, to minimize cross talk during signal acquisition. A 5-cycle Hanning-window-modulated sinusoidal tone burst, generated by a waveform generator (Tektronix® AFG31252) with a central frequency ranging from 50 kHz to 200 kHz in 50 kHz increments, is amplified to 200 $V_{p\text{-}p}$ using a power amplifier (Ciprian® US-TXP-3), to stimulate the PZT wafer (as the actuator). The GUWs-induced electrical resistance changes that are measured by the sensing network are converted into voltage signals, filtered and amplified through a self-developed amplifier, and then registered with an oscilloscope (Keysight® EXR104A). The oscilloscope also captures the GUWs response from the PZT wafer (as the sensor) and

compares it with the GUWs signal captured by the embedded sensing network.

By way of illustration, the GUWs signals under the excitation of 150 kHz that are self-sensed by the functionalized CFRP composites and by the PZT wafer (as the sensor), are compared in Figure 8.11b, to observe good agreement in the time-of-flight of the first arrival zeroth-order symmetric Lamb wave (denoted by S_0) and its waveform. The cross talk observed in signals captured by the functionalized CFRP composites at the excitation moment is caused by amplifiers, which does not affect the signal processing and interpretation. The discrepancy in signal magnitude between the two types of sensors can be attributed to their different sensing mechanisms: the PZT wafer gauges changes in piezoelectricity, while the graphene/CNC sensing unit detects changes in piezoresistivity based on the tunneling effect.

The amplitude and arrival time of the S_0 wave for the functionalized CFRP composites and the PZT receiver are analyzed at four frequencies. As illustrated in Figure 8.11c, the amplitude of the S_0 wave reaches its highest value at 150 kHz, corresponding to the resonance frequency of the PZT actuator. Additionally, as indicated in Figure 8.11d, the arrival time of the S_0 wave shows a consistent time difference between the CFRP composites and PZT receiver. This discrepancy is attributed to a small positioning error of approximately 1-2 mm when the PZT wafers are surface-mounted. The results affirm that the graphene/CNC sensing units exhibit a sensing capability equivalent to that of a commercial PZT wafer, underscoring the ability of the functionalized CFRP

composites of responding GUWs of the order of a few micrometers. The results affirm that the graphene/CNC sensing units exhibit a sensing capability equivalent to that of a commercial PZT wafer, underscoring the ability of the functionalized CFRP composites of responding GUWs of the order of a few micrometers.

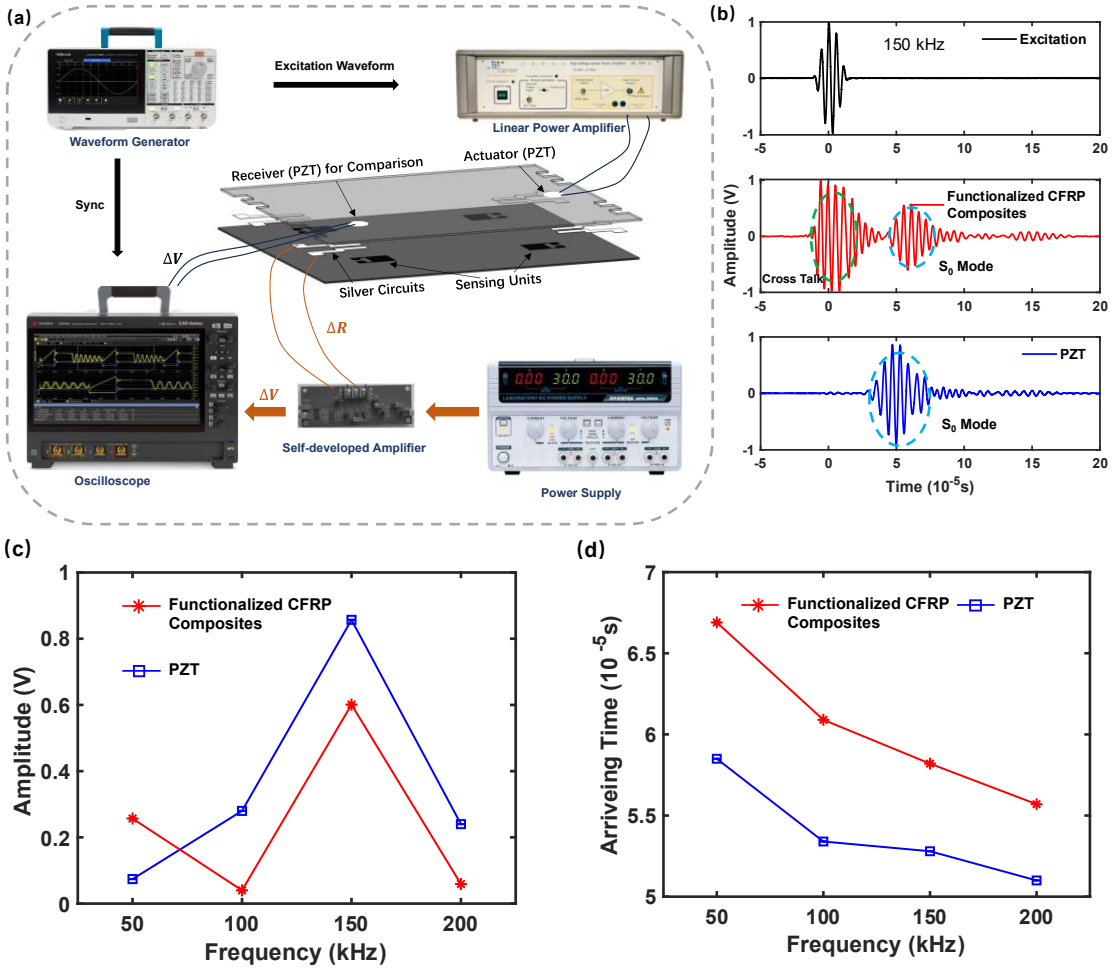

Figure 8.11 Experimental set-up and result of high-frequency GUWs test: (a) experimental set-up; (b) GUWs acquired with functionalized CFRP composites and surface-mounted PZT wafter at 150 kHz; the amplitude (c) and arriving time (d) of the S_0 wave at four frequencies, 50 kHz, 100 kHz, 150 kHz, and 200 kHz.

8.7 Summary

A new manufacturing framework based on the concept of "totally-additive-manufacturing" is developed. The "totally-additive-manufacturing"-functionalized CFRP composites are fabricated using a multi-material hybrid printing method, combining FDM-made composite structures and AJP-fabricated sensing network, through a seamless, operator-free process. The printing parameters for the graphene/CNC ink are optimized, revealing that a sheath flow rate of 600 sccm, an atomizer flow rate of 600 sccm, and a stage speed of 10 mm/s are conducive to functionalizing CFRP composites with the capacity of *in situ*, real-time integrity monitoring. The uniform and dense microstructures of the sensing units thus fabricated with the optimized printing parameters facilitate easy triggering of the tunneling effect among neighboring graphene sheets. The "totally-additive-manufacturing"-functionalized CFRP composites demonstrate the self-sensing capacity to quasi-static strains induced by cyclic loads and elastic perturbation with an ultralow amplitude (of the order of a few micrometers) and in an ultrasonic frequency range up to 200 kHz. This new manufacturing framework opens up new opportunities to customize and functionalize CFRP composites with the ability of self-monitoring structural integrity.

CHAPTER 9

Conclusions and Recommendations for Future Study

9.1 Conclusions

Electrochemical energy systems, FRP composites, wearable devices, and multifunctional intelligent structures are increasingly required to deliver both high performance and *in situ* monitoring in demanding engineering and biomedical environments. However, prevailing sensing technologies often fall short due to their rigidity, weight penalties, or incompatibility with host structures. Recent progress in nanotechnology and AM opens new avenues for embedding lightweight, flexible, and highly sensitive nanocomposite-based sensors directly into functional systems. This thesis explores such opportunities across multiple domains, from structural batteries to intelligent composites, through a unified additive manufacturing–driven strategy.

In the first stage, a graphene/polyvinyl alcohol-based flexible fiber sensor is fabricated via dip-coating for implantable battery monitoring. By leveraging percolation-driven conductive networks, the sensor achieves ultra-high sensitivity with minimum

detectable tensile and flexural strain of 0.009% and 0.028%, while maintaining 98.5% sensitivity retention over 2,000 mechanical cycles. Embedded within GFRP-encapsulated lithium-ion pouch cells, the sensor captures internal strains during charge–discharge cycles and transient perturbations from external impacts—signals inaccessible to conventional voltage-based BMS. Such capabilities provide early warning indicators against both electrochemical degradation and mechanically induced failure.

A nonintrusive graphene/epoxy nanocomposite sensor is then embedded into FRP laminates through co-curing. Owing to the identical epoxy chemistry between the sensor and host prepreg, intrusion into the composite is minimized, preserving mechanical integrity while achieving gauge factors up to 26. The embedded sensor demonstrates stable responses to quasi-static tensile loading, vibration, and GUWs up to 600 kHz. Structural tests confirm negligible compromise in stiffness and strength, validating the feasibility of embedding nanocomposite sensors into FRPs for simultaneous structural performance and in situ health monitoring.

Building upon this, an aerosol-jet-printed graphene/CNC acoustic sensor encapsulated in polyurethane film is developed for wearable applications. The sensor exhibits remarkable acoustic sensitivity, low hysteresis, and high reproducibility, enabling the detection of subtle speech signals and vocal cord vibrations. Integrated with a machine-learning algorithm (SVM), the device achieves digit recognition with an accuracy of

95.9%, underscoring its potential for healthcare, human–machine interaction, and assistive communication technologies.

To extend monitoring capabilities into structural composites, a graphene/CNC nanocomposite sensor network is printed and embedded into FRP laminates, forming distributed sensing units without sacrificing structural integrity. The network captures high-frequency elastic waves with accuracy comparable to piezoelectric sensors, while an integrated TDOA algorithm enables reliable localization of impact events. This lightweight and flexible sensing network demonstrates the feasibility of scalable, embedded SHM solutions for real-time monitoring of impact-induced damages.

Finally, a new paradigm of totally-additive-manufacturing is proposed and demonstrated by seamlessly integrating FDM-printed CFRP structures with aerosol-jet-printed sensing networks. The fabricated multifunctional CFRPs exhibit robust self-sensing capabilities for both quasi-static strain and high-frequency ultrasonic perturbations up to 200 kHz, facilitated by optimized microstructures that enhance tunneling effects among graphene sheets. This totally-additive-manufacturing framework introduces a scalable, operator-free route to manufacture intelligent composites that inherently combine structural integrity with real-time monitoring, opening new opportunities for next-generation smart structures.

In short, the merits and contributions of the AM-enabled nanocomposite sensors

developed in this PhD study can be summarized as follows:

- High-sensitivity implantable fiber sensors are developed for structural batteries, capable of detecting ultra-low strains during charge–discharge cycles and capturing transient impact-induced perturbations beyond the reach of conventional voltage-based monitoring.

- Nonintrusive nanocomposite sensors are embedded into FRP composites via co-curing, achieving broadband responsivity to quasi-static loads, vibrations, and guided ultrasonic waves (up to 600 kHz) while preserving the mechanical integrity of host structures.

- Wearable acoustic sensors are fabricated using AJP and polymer encapsulation, exhibiting excellent acoustic sensitivity, reversibility, and biocompatibility. Integrated with machine learning, they enable accurate speech recognition and open pathways toward healthcare and human–machine interaction.

- Distributed sensor networks based on printed nanocomposite units are integrated into FRP laminates, demonstrating robust capability in real-time acquisition of high-frequency elastic waves and accurate localization of impact events via TDOA algorithms.

- A totally-additive-manufacturing framework is proposed and validated, where FDM-printed CFRP structures are seamlessly integrated with printed nanocomposite sensing networks. The resulting multifunctional composites achieve simultaneous monitoring of quasi-static strains and ultrasonic perturbations, presenting a scalable route to intelligent structural materials.

9.2 Recommendations for Future Study

Although AM-driven nanocomposite sensors developed in this PhD study are of numerous merits, there are still several recommendations for extending research in the future.

First, the acquisition of high-frequency weak signals remains a critical limitation for piezoresistive sensing systems. Due to the gain–bandwidth trade-off, conventional amplifiers struggle to simultaneously provide high gain and high-frequency fidelity, restricting current sensors to a working range from quasi-static to ~1.2 MHz. By contrast, piezoelectric materials excel in the multi-megahertz regime but are insensitive to low-frequency or quasi-static strain. This complementary nature highlights a clear opportunity for hybrid additive manufacturing approaches that integrate both material systems. Such multimodal sensors would merge the broadband low-frequency sensitivity of piezoresistive nanocomposites with the high-frequency fidelity of piezoelectrics, thereby extending the operational spectrum and unlocking broader

applications in SHM.

Second, the rapid advances in motion control, vision, and auditory systems have enabled humanoid robots to operate across diverse terrains and application scenarios, from structured environments to unstructured outdoor conditions. Nevertheless, tactile sensing remains the final and indispensable step for executing precise and dexterous tasks. In particular, robotic hands require tactile sensors that are not only highly sensitive and stable but also capable of detecting multi-axial forces in order to replicate human-like manipulation. Nanocomposite-based sensors developed in this study provide a promising pathway toward such tactile sensing solutions. Their intrinsic flexibility, tunable sensitivity, and compatibility with additive manufacturing facilitate the design of conformal, lightweight, and robust tactile interfaces. By integrating these sensors onto flexible substrates and scaling them into arrays, it becomes possible to emulate the distributed mechanoreceptors of human skin, enabling robots to perceive pressure, strain, and vibration with spatial resolution. When coupled with advanced signal processing and machine learning algorithms, such nanocomposite tactile arrays hold the potential to furnish humanoid robots with refined haptic feedback, thus bridging the gap between robotic perception and execution.

References

[1] S. Das, T. Yokozeki, A brief review of modified conductive carbon/glass fibre reinforced composites for structural applications: Lightning strike protection, electromagnetic shielding, and strain sensing, Composites Part C: Open Access 5 (2021) 100162.
[2] N. Forintos, T. Czigany, Multifunctional application of carbon fiber reinforced polymer composites: Electrical properties of the reinforcing carbon fibers - A short review, Composites Part B-Engineering 162 (2019) 331-343.
[3] M.A. Karatas, H. Gokkaya, A review on machinability of carbon fiber reinforced polymer (CFRP) and glass fiber reinforced polymer (GFRP) composite materials, Defence Technology 14(4) (2018) 318-326.
[4] T.P. Sathishkumar, S. Satheeshkumar, J. Naveen, Glass fiber-reinforced polymer composites - a review, Journal of Reinforced Plastics and Composites 33(13) (2014) 1258-1275.
[5] X.Y. Zhang, H. Liu, X.Y. Ma, Z.C. Wang, G.P. Li, L. Han, K. Sun, Q.S. Yang, S.R. Ji, D.L. Yu, Y.T. Li, T.L. Ren, Deep Learning Enabled High-Performance Speech Command Recognition on Graphene Flexible Microphones, Acs Appl Electron Ma 4(5) (2022) 2306-2312.
[6] H. Tian, X.S. Li, Y.H. Wei, S.R. Ji, Q.S. Yang, G.Y. Gou, X.F. Wang, F. Wu, J.M. Jian, H. Guo, Y.C. Qiao, Y. Wang, W. Gu, Y.Z. Guo, Y. Yang, T.L. Ren, Bioinspired dual-channel speech recognition using graphene-based electromyographic and mechanical sensors, Cell Rep Phys Sci 3(10) (2022).
[7] D. Ravenscroft, I. Prattis, T. Kandukuri, Y.A. Samad, G. Mallia, L.G. Occhipinti, Machine Learning Methods for Automatic Silent Speech Recognition Using a Wearable Graphene Strain Gauge Sensor, Sensors-Basel 22(1) (2022).
[8] Z.C. Cai, H. Kim, Recent advances in MXene gas sensors: synthesis, composites, and mechanisms, Npj 2d Mater Appl 9(1) (2025).
[9] Y.H. Li, K. Wang, Z.Q. Su, Dispersed Sensing Networks in Nano-Engineered Polymer Composites: From Static Strain Measurement to Ultrasonic Wave Acquisition, Sensors 18(5) (2018).
[10] D. Kong, H. Lv, P. Ping, G. Wang, A review of early warning methods of thermal runaway of lithium ion batteries, Journal of Energy Storage 64 (2023) 107073.
[11] M.-K. Tran, A. Mevawalla, A. Aziz, S. Panchal, Y. Xie, M. Fowler, A review of lithium-ion battery thermal runaway modeling and diagnosis approaches, Processes 10(6) (2022) 1192.
[12] Q. Wang, P. Ping, X. Zhao, G. Chu, J. Sun, C. Chen, Thermal runaway caused fire and explosion of lithium ion battery, Journal of power sources 208 (2012) 210-224.
[13] M. Broussely, P. Biensan, F. Bonhomme, P. Blanchard, S. Herreyre, K. Nechev, R. Staniewicz, Main aging mechanisms in Li ion batteries, Journal of power sources 146(1-2) (2005) 90-96.
[14] D. Deng, Li-ion batteries: basics, progress, and challenges, Energy Science &

Engineering 3(5) (2015) 385-418.
[15] H. Li, Z. Wang, L. Chen, X. Huang, Research on advanced materials for Li-ion batteries, Advanced materials 21(45) (2009) 4593-4607.
[16] X. Guo, S. Guo, C. Wu, J. Li, C. Liu, W. Chen, Intelligent monitoring for safety-enhanced lithium-ion/sodium-ion batteries, Advanced Energy Materials 13(10) (2023) 2203903.
[17] Y. Shen, S. Wang, H. Li, K. Wang, K. Jiang, An overview on in situ/operando battery sensing methodology through thermal and stress measurements, Journal of Energy Storage 64 (2023) 107164.
[18] J. Jiang, X. Liu, X. Li, R. Yang, Mapping internal deformation in 4695 batteries through a combination of X-ray computer tomography and machine learning, Journal of Power Sources 621 (2024) 235130.
[19] J. Zhu, X. Zhang, H. Luo, E. Sahraei, Investigation of the deformation mechanisms of lithium-ion battery components using in-situ micro tests, Applied energy 224 (2018) 251-266.
[20] J.B. Siegel, A.G. Stefanopoulou, P. Hagans, Y. Ding, D. Gorsich, Expansion of lithium ion pouch cell batteries: observations from neutron imaging, Journal of the Electrochemical Society 160(8) (2013) A1031.
[21] S. Kocsis Szürke, M. Szabó, S. Szalai, S. Fischer, Deformation analysis of different lithium battery designs using the DIC technique, Energies 17(2) (2024) 323.
[22] A. Su, S. Mao, L. Lu, X. Han, M. Ouyang, Implanted potential sensing separator enables smart battery internal state monitor and safety alert, Etransportation 21 (2024) 100339.
[23] P. Nazari, R. Bäuerle, J. Zimmermann, C. Melzer, C. Schwab, A. Smith, W. Kowalsky, J. Aghassi-Hagmann, G. Hernandez-Sosa, U. Lemmer, Piezoresistive Free-standing Microfiber Strain Sensor for High-resolution Battery Thickness Monitoring, Advanced Materials 35(21) (2023) 2212189.
[24] L. Albero Blanquer, F. Marchini, J.R. Seitz, N. Daher, F. Bétermier, J. Huang, C. Gervillié, J.-M. Tarascon, Optical sensors for operando stress monitoring in lithium-based batteries containing solid-state or liquid electrolytes, Nature communications 13(1) (2022) 1153.
[25] Y. Li, Y. Zhang, Z. Li, Z. Yan, X. Xiao, X. Liu, J. Chen, Y. Shen, Q. Sun, Y. Huang, Operando decoding of surface strain in anode-free lithium metal batteries via optical fiber sensor, Advanced Science 9(26) (2022) 2203247.
[26] Z. Miao, Y. Li, X. Xiao, Q. Sun, B. He, X. Chen, Y. Liao, Y. Zhang, L. Yuan, Z. Yan, Direct optical fiber monitor on stress evolution of the sulfur-based cathodes for lithium–sulfur batteries, Energy & Environmental Science 15(5) (2022) 2029-2038.
[27] J. Peng, X. Zhou, S. Jia, Y. Jin, S. Xu, J. Chen, High precision strain monitoring for lithium ion batteries based on fiber Bragg grating sensors, Journal of Power Sources 433 (2019) 226692.
[28] J. Xi, J. Li, H. Sun, T. Ma, L. Deng, N. Liu, X. Huang, J. Zhang, In-situ monitoring of internal temperature and strain of solid-state battery based on optical fiber sensors, Sensors and Actuators A: Physical 347 (2022) 113888.
[29] Y. Yu, E. Vergori, F. Maddar, Y. Guo, D. Greenwood, J. Marco, Real-time

monitoring of internal structural deformation and thermal events in lithium-ion cell via embedded distributed optical fibre, Journal of Power Sources 521 (2022) 230957.
[30] Y. Zhang, X. Xiao, W. Chen, Z. Zhang, W. Li, X. Ge, Y. Li, J. Xiang, Q. Sun, Z. Yan, In operando monitoring the stress evolution of silicon anode electrodes during battery operation via optical fiber sensors, Small 20(29) (2024) 2311299.
[31] J. Bang, B. Chun, M. Kim, J. Lim, Y. Han, H. So, Rapid thermal runaway detection of lithium-ion battery via swelling-based state-of-charge monitoring using piezoresistive sponge sensor, eTransportation 24 (2025) 100404.
[32] H. Li, Q. Guo, W. Yu, W. Yuan, J. Wu, C. Meng, S. Guo, Piezoresistive-piezocapacitive hybrid pressure sensor based on synergetic MXene porous conducting and ion trapping effects for operando battery state-of-charge monitoring, Chemical Engineering Journal 497 (2024) 154929.
[33] A.A. Badr, A.K. Abdul-Hassan, A review on voice-based interface for human-robot interaction, Iraqi Journal for Electrical and Electronic Engineering 16(2) (2020) 1-12.
[34] H. Medicherla, A. Sekmen, Human–robot interaction via voice-controllable intelligent user interface, Robotica 25(5) (2007) 521-527.
[35] J. Suo, X. Yang, Y.-o. Leung, J. Wang, M. Chen, Y. Liu, H. Sun, Z. Wang, X. Qiao, W.J. Li, Enabling Natural Human-Computer Interaction Through AI-Powered Nanocomposite IoT Throat Vibration Sensor, IEEE Internet of Things Journal (2024).
[36] M.S. Hossain, G. Muhammad, A. Alamri, Smart healthcare monitoring: a voice pathology detection paradigm for smart cities, Multimedia Systems 25(5) (2019) 565-575.
[37] J. Wang, J. Suo, D. Liu, Y. Zhao, Y. Tian, P. Bryanston-Cross, W.J. Li, Z. Wang, A Nanoparticle-Based Artificial Ear for Personalized Classification of Emotions in the Human Voice Using Deep Learning, ACS Applied Materials & Interfaces 16(38) (2024) 51274-51282.
[38] H.J. Choi, J. Ahn, B.K. Jung, Y.K. Choi, T. Park, J. Bang, J. Park, Y. Yang, G. Son, S.J. Oh, Highly Conductive and Sensitive Wearable Strain Sensors with Metal/Nanoparticle Double Layer for Noninterference Voice Detection, ACS Applied Materials & Interfaces 15(36) (2023) 42836-42844.
[39] B. Ozlu, B.S. Shim, Flexible and wearable PEDOT-paper pressure sensor for detecting human voice, 2021 IEEE International Conference on Big Data and Smart Computing (BigComp), IEEE, 2021, pp. 317-320.
[40] Y. Shen, F. Yang, W. Lu, W. Chen, S. Huang, N. Li, A highly stretchable and breathable polyurethane fibrous membrane sensor for human motion monitoring and voice signal recognition, Sensors and Actuators A: Physical 331 (2021) 112974.
[41] Y. Su, K. Ma, X. Zhang, M. Liu, Neural network-enabled flexible pressure and temperature sensor with honeycomb-like architecture for voice recognition, Sensors 22(3) (2022) 759.
[42] J. Xie, Y. Zhao, D. Zhu, J. Yan, J. Li, M. Qiao, G. He, S. Deng, A machine learning-combined flexible sensor for tactile detection and voice recognition, ACS Applied Materials & Interfaces 15(9) (2023) 12551-12559.
[43] X. Zhao, Y. Zhou, A. Li, J. Xu, S. Karjagi, E. Hahm, L. Rulloda, J. Li, J. Hollister,

P. Kavehpour, A self-filtering liquid acoustic sensor for voice recognition, Nature Electronics (2024) 1-9.
[44] X.L.P. Qing, S.J. Beard, A. Kumar, H.L. Chan, R. Ikegami, Advances in the development of built-in diagnostic system for filament wound composite structures, Composites Science and Technology 66(11-12) (2006) 1694-1702.
[45] J.S. Chilies, A.F. Koutsomitopoulou, A.J. Croxford, I.P. Bond, Monitoring cure and detecting damage in composites with inductively coupled embedded sensors, Composites Science and Technology 134 (2016) 81-88.
[46] S. Masmoudi, A. El Mahi, S. Turki, Fatigue behaviour and structural health monitoring by acoustic emission of E-glass/epoxy laminates with piezoelectric implant, Applied Acoustics 108 (2016) 50-58.
[47] Y.H. Li, Y.Z. Liao, Z.Q. Su, Graphene-functionalized polymer composites for self-sensing of ultrasonic waves: An initiative towards "sensor-free" structural health monitoring, Composites Science and Technology 168 (2018) 203-213.
[48] Y.Z. Liao, F. Duan, H.T. Zhang, Y. Lu, Z.H. Zeng, M.L. Liu, H. Xu, C. Gao, L.M. Zhou, H. Jin, Z. Zhang, Z.Q. Su, Ultrafast response of spray-on nanocomposite piezoresistive sensors to broadband ultrasound, Carbon 143 (2019) 743-751.
[49] P. Zhou, Y. Liao, Y. Li, D. Pan, W. Cao, X. Yang, F. Zou, L.-m. Zhou, Z. Zhang, Z. Su, An inkjet-printed, flexible, ultra-broadband nanocomposite film sensor for in-situ acquisition of high-frequency dynamic strains, Composites Part A: Applied Science and Manufacturing 125 (2019) 105554.
[50] Y.Y. Su, J.W. Yang, Y.Z. Liao, P.Y. Zhou, L. Xu, L.M. Zhou, Z.Q. Su, An implantable, compatible and networkable nanocomposite piezoresistive sensor for in situ acquisition of dynamic responses of CFRPs, Composites Science and Technology 208 (2021).
[51] A.N. Dickson, J.N. Barry, K.A. McDonnell, D.P. Dowling, Fabrication of continuous carbon, glass and Kevlar fibre reinforced polymer composites using additive manufacturing, Addit Manuf 16 (2017) 146-152.
[52] A.N. Dickson, K.A. Ross, D.P. Dowling, Additive manufacturing of woven carbon fibre polymer composites, Compos Struct 206 (2018) 637-643.
[53] M. Saeidi-Javash, Y.P. Du, M.X. Zeng, B.C. Wyatt, B.W. Zhang, N. Kempf, B. Anasori, Y.L. Zhang, All-Printed MXene-Graphene Nanosheet-Based Bimodal Sensors for Simultaneous Strain and Temperature Sensing, Acs Appl Electron Ma 3(5) (2021) 2341-2348.
[54] T. Fapanni, E. Sardini, M. Serpelloni, S. Tonello, Nano-Functionalized Electrochemical Sensors by Aerosol Jet Printing, Ieee Sens J 22(22) (2022) 21498-21507.
[55] Y.C. Zhu, L.K. Yu, D.Z. Wu, W.L. Lv, L.Y. Wang, A high-sensitivity graphene ammonia sensor via aerosol jet printing, Sensor Actuat a-Phys 318 (2021).
[56] M.T. Rahman, R. Moser, H.M. Zbib, C.V. Ramana, R. Panat, 3D printed high performance strain sensors for high temperature applications, J Appl Phys 123(2) (2018).
[57] H. Jeong, Y. Cui, M.M. Tentzeris, S. Lim, Hybrid (3D and inkjet) printed electromagnetic pressure sensor using metamaterial absorber, Addit Manuf 35 (2020)

101405.
[58] S. Swaminathan, K.B. Ozutemiz, C. Majidi, S.E. Hudson, FiberWire: Embedding Electronic Function into 3D Printed Mechanically Strong, Lightweight Carbon Fiber Composite Objects, Chi 2019: Proceedings of the 2019 Chi Conference on Human Factors in Computing Systems (2019).
[59] Y.D. Chen, V. Nagarajan, D.W. Rosen, W.W. Yu, S.Y. Huang, Aerosol jet printing on paper substrate with conductive silver nano material, J Manuf Process 58 (2020) 55-66.
[60] M. Smith, Y.S. Choi, C. Boughey, S. Kar-Narayan, Controlling and assessing the quality of aerosol jet printed features for large area and flexible electronics, Flexible and Printed Electronics 2(1) (2017) 015004.
[61] K. Wang, Y.H. Chang, C. Zhang, B. Wang, Conductive-on-demand: Tailorable polyimide/carbon nanotube nanocomposite thin film by dual-material aerosol jet printing, Carbon 98 (2016) 397-403.
[62] E. Jabari, E. Toyserkani, Micro-scale aerosol-jet printing of graphene interconnects, Carbon 91 (2015) 321-329.
[63] P. Zhuo, S.G. Li, I.A. Ashcroft, A.I. Jones, Material extrusion additive manufacturing of continuous fibre reinforced polymer matrix composites: A review and outlook, Compos Part B-Eng 224 (2021).
[64] S.S. Dasari, A.J. Wright, J.M. Carroll, A. Sarmah, D.G. Carey, N. Nagabandi, T.Q. Tran, M.J. Green, Freeform additive manufacturing of carbon fiber reinforced composites using dielectric barrier discharge-assisted Joule heating, Composites Part A: Applied Science and Manufacturing 179 (2024) 108047.
[65] B.M. Gackowski, M. Sharma, X.Q. Koh, D.H.L. Seng, D. Verma, V. Raveenkumar, S. Idapalapati, Surface engineering of carbon nanotube-carbon fiber networks for enhanced strength in additive manufacturing of nylon composites, Composites Part A: Applied Science and Manufacturing (2024) 108383.
[66] A. Fernández, N. Blanco, D. Trias, N. Gascons, Assessment of damage sequence in additive manufactured composite laminates under quasi-static out-of-plane loading, Composites Part A: Applied Science and Manufacturing 184 (2024) 108263.
[67] M.Y. Khalid, R. Umer, Y.H. Zweiri, J.-K. Kim, Rise of graphene in novel piezoresistive sensing applications: A review on recent development and prospect, Materials Science and Engineering: R: Reports 163 (2025) 100891.
[68] Y. Liu, M. Yi, T. Chen, X. Mu, Q. Sun, J. Zhou, Advances in graphene-based flexible wearable piezoresistive strain sensors, Journal of Materials Science: Materials in Electronics 36(20) (2025) 1-26.
[69] S. Vinodhini, J.R. Xavier, Recent progress in graphene-based nanocomposites for enhanced energy storage and corrosion protection, Journal of Materials Science (2025) 1-43.
[70] H. Asgharian, V. Kammarchedu, S.J. Gu, A. Ebrahimi, WoundMx: Multiplexed Detection of Wound Infection Biomarkers with a Multimodal Sensor System based on Laser-Induced Graphene, Res Sq (2025).
[71] Z. Chen, D. Xie, K. Kojima, C. Gao, J. Shi, J. Xing, H. Morikawa, C. Zhu, Fibrous Pressure Sensor with Unique Resistance Increase under Partial Compression: Coaxial

Wet-Spun TiO(2)/Graphene/Thermoplastic Polyurethane Multi-Wall Multifunctional Fiber, Adv Mater (2025) e2509631.
[72] A.C.P. Fernandes, N.C. Vicentini, M.S. Couto, G.R. Carvalho, B. Fragneaud, C. Legnani, I.O. Maciel, R.L.F. Filho, J.V.C. Nascimento, J.P.E. Ferreira, F. Barino, D. Coelho, A.B. Dos Santos, W.G. Quirino, High-Sensitivity CO(2) Sensor Based on a Graphene Oxide Coated Long-Period Fiber Grating, ACS Omega 10(22) (2025) 22874-22883.
[73] X. Lei, H. Fan, Y. Zhao, M. Zhong, Z. Wu, L. Li, S. Li, X. Xing, J. Liu, Y. Sun, Y. Jiang, G. Ren, MXene-Enhanced Laser-Induced Graphene Flexible Sensor with Rapid Response for Monitoring Pilots' Body Motion, Micromachines (Basel) 16(5) (2025).
[74] L. Li, Y. Han, Y. Zhang, W. Wu, W. Du, G. Wen, S. Cheng, Laser-Induced Graphene Decorated with MOF-Derived NiCo-LDH for Highly Sensitive Non-Enzymatic Glucose Sensor, Molecules 29(23) (2024).
[75] J. Villalba-Diez, A. Gonzalez-Marcos, Quantum-classical deep learning hybrid architecture with graphene-printed low-cost capacitive sensor for essential tremor detection, Sci Rep 15(1) (2025) 20204.
[76] Y. Wang, H. Yao, L. Liang, X. Yan, Z. Wang, X. Hu, Z. Li, Y. Li, Y. Lv, Q.L. Yang, Graphene-assisted electromagnetically induced transparency-like terahertz bio-sensor for ultrasensitive detection using optics-enhanced sensing, Opt Express 33(3) (2025) 4817-4831.
[77] Y. Zhao, Q. Wen, B. Hu, X. Yu, X. Wan, Z. Han, P. Wang, Z. Lin, X. Zhu, X. Ruan, F. Wu, W. Hong, Q. Hong, X. Guo, Fast-Response and Broad-Detection-Range Flexible Capacitive Pressure Sensor Based on Origami-Structured Barium Titanate Nanoparticles/Graphene/Silicone Rubber Nanocomposites, ACS Appl Mater Interfaces 17(30) (2025) 43716-43729.
[78] F. Abedheydari, S. Sadeghzadeh, M. Saadatbakhsh, A. Heydariyan, E. Khakpour, Silver-decorated laser-induced graphene for a linear, sensitive, and almost hysteresis-free piezoresistive strain sensor, Sci Rep-Uk 14(1) (2024).
[79] B.D. Chen, H.Q. Li, S.F. Zhang, X.J. Lai, X.R. Zeng, X.R. Wu, X.T. Cheng, H. Liu, High-performance and superhydrophobic piezoresistive pressure sensor based on mountain ridge-like microstructure by silver nanoparticles and reduced graphene oxide, Compos Part a-Appl S 162 (2022).
[80] X. Chen, K.W. Gan, S.H. Pu, M. Jalalvand, A.R. Hamilton, Piezoresistive laser-induced graphene as a low-cost strain sensor for composite structures, Sensor Actuat a-Phys 393 (2025).
[81] H.N. Cheng, B. Wang, K. Yang, Y.Q. Yang, C.X. Wang, A high-performance piezoresistive sensor based on poly (styrene-co-methacrylic acid)@polypyrrole microspheres/ graphene-decorated TPU electrospun membrane for human motion detection, Chem Eng J 426 (2021).
[82] S.W. Kim, J.-H. Lee, H.J. Ko, S. Lee, G.Y. Bae, D. Kim, G. Lee, S.G. Lee, K. Cho, Mechanically robust and linearly sensitive soft piezoresistive pressure sensor for a wearable human–robot interaction system, ACS nano 18(4) (2024) 3151-3160.
[83] H. Puozzo, S. Saiev, L. Bonnaud, D. Beljonne, R. Lazzaroni, Integrating

Benzoxazine-PDMS 3D Networks with Carbon Nanotubes for flexible Pressure Sensors, Chemistry–A European Journal 30(2) (2024) e202301791.
[84] D.K. Saha, H. Godaba, Integrated force and displacement sensing in an untethered dielectric elastomer actuator with a piezoresistive element, Sensors and Actuators A: Physical 365 (2024) 114889.
[85] X. Su, W. Yang, Z. Zhang, L. Deng, K. Li, H. Xie, Y. Wu, X. Zhang, W. Wu, Conductive cross-linkable PDMS-MXene nanosheet networks on polyurethane sponges as robust superhydrophobic sensors for human motion detection, ACS Applied Nano Materials 7(2) (2024) 2164-2175.
[86] M. Xie, G. Qian, Y. Yu, C. Chen, H. Li, D. Li, High-performance flexible reduced graphene oxide/polyimide nanocomposite aerogels fabricated by double crosslinking strategy for piezoresistive sensor application, Chem Eng J 480 (2024) 148203.
[87] A. Januszko, K. Górski, K.A. Bogdanowicz, K. Drabczyk, M. Zdrojek, K. Zeranska, W. Pellowski, J. Miedziak, A. Iwan, Graphene Flakes and Ethylene-Vinyl Acetate-Based Sensor for Detecting Mechanical Damage in Photovoltaic Panels on Sound-Absorbing Screens: An Engineering Approach for Civil and Military Applications, Energies 18(7) (2025).
[88] Y. Wang, T.T. Yang, J.C. Lao, R.J. Zhang, Y.Y. Zhang, M. Zhu, X. Li, X.B. Zang, K.L. Wang, W.J. Yu, H. Jin, L. Wang, H.W. Zhu, Ultra-sensitive graphene strain sensor for sound signal acquisition and recognition, Nano Res 8(5) (2015) 1627-1636.
[89] D.H. Ho, Y.Y. Choi, S.B. Jo, J.M. Myoung, J.H. Cho, Sensing with MXenes: progress and prospects, Advanced materials 33(47) (2021) 2005846.
[90] Y. Wang, Y. Yue, F. Cheng, Y. Cheng, B. Ge, Ti3C2Tx MXene-based flexible piezoresistive physical sensors. ACS Nano 16, 1734–1758 (2022).
[91] J. Cheng, F. Xie, S. Jiang, X.T. Cai, D.Y. Lou, Q.L. Li, Q. Tao, D. Liu, Flexible capacitive pressure sensor based on one-step laser-reduced graphene oxide electrodes and polyurethane/MXene dielectric, J Reinf Plast Comp (2025).
[92] Y.F. Cheng, M.J. Wang, N. Ma, R.H. Zhang, Z.Z. Cai, M.Y. Liu, Z.Y. Liu, S.W. Yan, J.S. Zhang, Y. Yue, J.B. Wang, W.J. Liu, L.Y. Li, Nanoscale Interlayer Engineering Enhances MXene-Based Flexible Pressure Sensor, Nano Lett 25(31) (2025) 11782-11789.
[93] J. Fu, J.J. Du, Y. Huang, Y.B. Wu, Q.S. Shi, High performance strain sensor based on TPU/PAN with MXene/ILs dual conductive network for human health monitoring and handwriting recognition, Diam Relat Mater 157 (2025).
[94] F.Y. Dong, Q.H. Peng, G.A. Yu, H.X. Du, W.L. Sha, P.S. Li, Y.L. Liu, H. Cai, T.L. Du, M.Y. Xu, MXene and PAN-Based Carbon Fiber Enhanced Bimodal Triboelectric Sensor for Robotic Arm Perception and Control, Small (2025).
[95] Y. Gu, Y.X. Cao, D.B. Wang, A Novel Bilayer MXene/GO Pressure Sensor Array for Multimode and High-Precision Frequency Regulation, Ieee Sens J 25(15) (2025) 28184-28191.
[96] M.Z. Hasan, C.H. Xu, L. Luo, K.Z.M.A. Motaleb, M.F. Ahmed, S.R. Tan, M.M. Bashar, J. Januteniene, C.F. Yue, H. Tu, S. Sha, G.M. Cai, R.Q. Zhang, Facile fabrication of robust, recyclable, and multifunctional composite hydrogel sensor with MXene and cellulose microcrystals, Ind Crop Prod 231 (2025).

[97] Z.C. He, L. Chang, C.Y. Hu, M.D.F.R. Forhad, Y.F. Zhou, S.J. Chen, L. Jiang, Highly Flexible and Stretchable Strain Sensor Based on Elastic Melt-Blown Nonwovens Fabric Deposited With MXene/MWCNTs, Polym Eng Sci (2025).
[98] B.X. Huang, S. Wu, J.J. Liu, J. Liu, B.Y. Peng, Z.H. Zhou, Aerosol jet printing of polyelectrolyte-modified MXene ink for a multifunctional humidity and temperature flexible sensor, Chem Eng J 519 (2025).
[99] Q.S. Ji, Y.X. Li, Z.H. Wang, X.S. Tan, L. Sun, S. Li, C.C. Wang, R.Q. Chen, F.X. Chu, J.Y. Nan, C.P. Wang, A Highly Tough and Strain-Sensitive MXene Hydrogel Sensor Enabling Integrated Wearable Electronics with Body Conformability and Real-Time Visualization, Small 21(31) (2025).
[100] Q. Ge, Z. Li, Z. Wang, K. Kowsari, W. Zhang, X. He, J. Zhou, N.X. Fang, Projection micro stereolithography based 3D printing and its applications, International Journal of Extreme Manufacturing 2(2) (2020) 022004.
[101] P.F. Flowers, C. Reyes, S. Ye, M.J. Kim, B.J. Wiley, 3D printing electronic components and circuits with conductive thermoplastic filament, Additive Manufacturing 18 (2017) 156-163.
[102] M.H. Omar, K.A. Razak, M.N. Ab Wahab, H.H. Hamzah, Recent progress of conductive 3D-printed electrodes based upon polymers/carbon nanomaterials using a fused deposition modelling (FDM) method as emerging electrochemical sensing devices, RSC advances 11(27) (2021) 16557-16571.
[103] D.C. Carvalho Fernandes, D. Lynch, V. Berry, 3D-printed graphene/polymer structures for electron-tunneling based devices, Sci Rep-Uk 10(1) (2020) 11373.
[104] A.M.L. Marzo, C.C. Mayorga-Martinez, M. Pumera, 3D-printed graphene direct electron transfer enzyme biosensors, Biosensors and Bioelectronics 151 (2020) 111980.
[105] W.J. Scheideler, J. Im, Recent advances in 3D printed electrodes–bridging the nano to mesoscale, Advanced Science 12(9) (2025) 2411951.
[106] A. Maguire, N. Pottackal, M. Saadi, M.M. Rahman, P.M. Ajayan, Additive manufacturing of polymer-based structures by extrusion technologies, Oxford Open Materials Science 1(1) (2021) itaa004.
[107] P. Jiang, Z. Ji, X. Zhang, Z. Liu, X. Wang, Recent advances in direct ink writing of electronic components and functional devices, Progress in Additive Manufacturing 3(1) (2018) 65-86.
[108] H. Liu, H. Zhang, W. Han, H. Lin, R. Li, J. Zhu, W. Huang, 3D printed flexible strain sensors: from printing to devices and signals, Advanced Materials 33(8) (2021) 2004782.
[109] H. Woods, A. Boddorff, E. Ewaldz, Z. Adams, M. Ketcham, D.J. Jang, E. Sinner, N. Thadhani, B. Brettmann, Rheological considerations for binder development in direct ink writing of energetic materials, Propellants, Explosives, Pyrotechnics 45(1) (2020) 26-35.
[110] Y. Zhang, G. Shi, J. Qin, S.E. Lowe, S. Zhang, H. Zhao, Y.L. Zhong, Recent progress of direct ink writing of electronic components for advanced wearable devices, Acs Appl Electron Ma 1(9) (2019) 1718-1734.
[111] D.A. Porter, A.L. Cohen, P.S. Krueger, D.Y. Son, Additive manufacturing with ultraviolet curable silicones containing carbon black, 3D Printing and Additive

Manufacturing 5(1) (2018) 73-86.
[112] Z. Lin, X. Qiu, Z. Cai, J. Li, Y. Zhao, X. Lin, J. Zhang, X. Hu, H. Bai, High internal phase emulsions gel ink for direct-ink-writing 3D printing of liquid metal, Nature Communications 15(1) (2024) 4806.
[113] B.Y. Ahn, D. Shoji, C.J. Hansen, E. Hong, D.C. Dunand, J.A. Lewis, Printed origami structures, Advanced Materials 22(20) (2010) 2251-2254.
[114] M. Calvo, A.E. Jakus, R.N. Shah, R. Spolenak, D.C. Dunand, Microstructure and processing of 3D printed tungsten microlattices and infiltrated W–Cu composites, Advanced Engineering Materials 20(9) (2018) 1800354.
[115] H. Yuk, B. Lu, S. Lin, K. Qu, J. Xu, J. Luo, X. Zhao, 3D printing of conducting polymers, Nature communications 11(1) (2020) 1604.
[116] Y. He, F. Yang, H. Zhao, Q. Gao, B. Xia, J. Fu, Research on the printability of hydrogels in 3D bioprinting, Sci Rep-Uk 6(1) (2016) 29977.
[117] M.S. Onses, E. Sutanto, P.M. Ferreira, A.G. Alleyne, J.A. Rogers, Mechanisms, capabilities, and applications of high-resolution electrohydrodynamic jet printing, Small 11(34) (2015) 4237-4266.
[118] M. Kuang, L. Wang, Y. Song, Controllable printing droplets for high-resolution patterns, Advanced materials 26(40) (2014) 6950-6958.
[119] J. Im, G.F. Trindade, T.T. Quach, A. Sohaib, F. Wang, J. Austin, L. Turyanska, C.J. Roberts, R. Wildman, R. Hague, Functionalized gold nanoparticles with a cohesion enhancer for robust flexible electrodes, ACS Applied Nano Materials 5(5) (2022) 6708-6716.
[120] F. Wang, J.H. Gosling, G.F. Trindade, G.A. Rance, O. Makarovsky, N.D. Cottam, Z. Kudrynskyi, A.G. Balanov, M.T. Greenaway, R.D. Wildman, Inter-flake quantum transport of electrons and holes in inkjet-printed graphene devices, Advanced Functional Materials 31(5) (2021) 2007478.
[121] S.K. Eshkalak, A. Chinnappan, W. Jayathilaka, M. Khatibzadeh, E. Kowsari, S. Ramakrishna, A review on inkjet printing of CNT composites for smart applications, Applied Materials Today 9 (2017) 372-386.
[122] U. Kraft, F. Molina-Lopez, D. Son, Z. Bao, B. Murmann, Ink development and printing of conducting polymers for intrinsically stretchable interconnects and circuits, Advanced Electronic Materials 6(1) (2020) 1900681.
[123] M.A. Ali, C. Hu, E.A. Yttri, R. Panat, Recent advances in 3D printing of biomedical sensing devices, Advanced functional materials 32(9) (2022) 2107671.
[124] Y. Li, Y. Liu, S.R.A. Bhuiyan, Y. Zhu, S. Yao, Printed strain sensors for on-skin electronics, Small Structures 3(2) (2022) 2100131.
[125] C. Cao, J.B. Andrews, A.D. Franklin, Completely printed, flexible, stable, and hysteresis-free carbon nanotube thin-film transistors via aerosol jet printing, Advanced Electronic Materials 3(5) (2017) 1700057.
[126] J.M. Hoey, A. Lutfurakhmanov, D.L. Schulz, I.S. Akhatov, A review on aerosol-based direct-write and its applications for microelectronics, Journal of Nanotechnology 2012(1) (2012) 324380.
[127] A. Mahajan, C.D. Frisbie, L.F. Francis, Optimization of aerosol jet printing for high-resolution, high-aspect ratio silver lines, ACS applied materials & interfaces 5(11)

(2013) 4856-4864.
[128] P.V. Arsenov, A.A. Efimov, V.V. Ivanov, Effect of methods of changing in focusing ratio on line geometry in aerosol jet printing, Key Engineering Materials 779 (2018) 159-164.
[129] T. Ma, Y. Li, H. Cheng, Y. Niu, Z. Xiong, A. Li, X. Jiang, D. Park, K. Zhang, C. Yi, Enhanced aerosol-jet printing using annular acoustic field for high resolution and minimal overspray, Nature Communications 15(1) (2024) 6317.
[130] Y. Niu, Y. Han, H. Cheng, Z. Xiong, B. Luo, T. Ma, L. Li, S. Liu, X. Chen, C. Yi, Synthesized silver nanoparticles decorated reduced graphene oxide/silver ink for aerosol jet printed conformal temperature sensor with a wide sensing range and excellent stability, Journal of Materials Research and Technology 25 (2023) 873-886.
[131] Y. Niu, Z. Wang, Y. Li, B. Huang, T. Ma, X. Jiang, H. Cheng, K. Zhang, C. Yi, Ultrathin MXene/Ag-Ag nanocomposite films for 3D-conformal electromagnetic shielding via aerosol jet printing, Chem Eng J 506 (2025) 160122.
[132] Z. Xiong, C. Yi, Y. Li, Y. Niu, T. Ma, A. Li, H. Cheng, K. Zhang, Accurate at-line measurement of deposition rate for aerosol jet printing for the fabrication of 3D patterns and resistors with high precision, Journal of Manufacturing Processes 141 (2025) 1151-1160.
[133] N. McKibben, B. Ryel, J. Manzi, F. Muramutsa, J. Daw, H. Subbaraman, D. Estrada, Z. Deng, Aerosol jet printing of piezoelectric surface acoustic wave thermometer, Microsystems & nanoengineering 9(1) (2023) 51.
[134] R. Wang, L. Sun, X. Zhu, W. Ge, H. Li, Z. Li, H. Zhang, Y. Huang, Z. Li, Y.F. Zhang, Carbon nanotube-based strain sensors: Structures, fabrication, and applications, Advanced Materials Technologies 8(1) (2023) 2200855.
[135] Y.-R. Ding, C.-H. Xue, X.-J. Guo, X. Wang, S.-T. Jia, Q.-F. An, Fabrication of TPE/CNTs film at air/water interface for flexible and superhydrophobic wearable sensors, Chem Eng J 409 (2021) 128199.
[136] Y. Shang, B. Zhang, J. Liu, C. Xia, X. Yang, D. Yan, J. Sun, Facile and economical fabrication of superhydrophobic flexible resistive strain sensors for human motion detection, Nanomanufacturing and Metrology 6(1) (2023) 2.
[137] S. Seyedin, P. Zhang, M. Naebe, S. Qin, J. Chen, X. Wang, J.M. Razal, Textile strain sensors: a review of the fabrication technologies, performance evaluation and applications, Materials Horizons 6(2) (2019) 219-249.
[138] Z. Wang, Q. Zhang, Y. Yue, J. Xu, W. Xu, X. Sun, Y. Chen, J. Jiang, Y. Liu, 3D printed graphene/polydimethylsiloxane composite for stretchable strain sensor with tunable sensitivity, Nanotechnology 30(34) (2019) 345501.
[139] C. Yan, J. Wang, W. Kang, M. Cui, X. Wang, C.Y. Foo, K.J. Chee, P.S. Lee, Highly stretchable piezoresistive graphene–nanocellulose nanopaper for strain sensors, Advanced materials 26(13) (2014) 2022-2027.
[140] D. Marinković, G. Rama, M. Zehn, Abaqus implementation of a corotational piezoelectric 3-node shell element with drilling degree of freedom, Facta Universitatis, Series: Mechanical Engineering 17(2) (2019) 269-283.
[141] D. Marinkovic, Z. Marinkovic, On FEM modeling of piezoelectric actuators and sensors for thin-walled structures, Smart Structures and Systems 9(5) (2012) 411-426.

[142] J. Cao, Q. Wang, H. Dai, Electromechanical properties of metallic, quasimetallic, and semiconducting carbon nanotubes under stretching, Physical review letters 90(15) (2003) 157601.
[143] J. Zhao, C. He, R. Yang, Z. Shi, M. Cheng, W. Yang, G. Xie, D. Wang, D. Shi, G. Zhang, Ultra-sensitive strain sensors based on piezoresistive nanographene films, Applied Physics Letters 101(6) (2012).
[144] S. Luo, T. Liu, Structure–property–processing relationships of single-wall carbon nanotube thin film piezoresistive sensors, Carbon 59 (2013) 315-324.
[145] L. Lu, N. Zhao, J. Liu, B. Yang, Coupling piezoelectric and piezoresistive effects in flexible pressure sensors for human motion detection from zero to high frequency, Journal of Materials Chemistry C 9(29) (2021) 9309-9318.
[146] Q. Zheng, J.-h. Lee, X. Shen, X. Chen, J.-K. Kim, Graphene-based wearable piezoresistive physical sensors, Materials Today 36 (2020) 158-179.
[147] F. He, X. You, H. Gong, Y. Yang, T. Bai, W. Wang, W. Guo, X. Liu, M. Ye, Stretchable, biocompatible, and multifunctional silk fibroin-based hydrogels toward wearable strain/pressure sensors and triboelectric nanogenerators, ACS applied materials & interfaces 12(5) (2020) 6442-6450.
[148] S. Wu, S. Peng, Y. Yu, C.H. Wang, Strategies for designing stretchable strain sensors and conductors, Advanced Materials Technologies 5(2) (2020) 1900908.
[149] H. Souri, D. Bhattacharyya, Highly sensitive, stretchable and wearable strain sensors using fragmented conductive cotton fabric, Journal of Materials Chemistry C 6(39) (2018) 10524-10531.
[150] A. Desai, M.A. Haque, Mechanics of the interface for carbon nanotube–polymer composites, Thin-walled structures 43(11) (2005) 1787-1803.
[151] M. Amjadi, M. Turan, C.P. Clementson, M. Sitti, Parallel microcracks-based ultrasensitive and highly stretchable strain sensors, ACS applied materials & interfaces 8(8) (2016) 5618-5626.
[152] G. Hassan, J. Bae, A. Hassan, S. Ali, C.H. Lee, Y. Choi, Ink-jet printed stretchable strain sensor based on graphene/ZnO composite on micro-random ridged PDMS substrate, Composites Part A: Applied Science and Manufacturing 107 (2018) 519-528.
[153] P. Yang, Z. Liu, J. Luo, R. Li, Y. Lu, X. Huang, Q. Zhang, Z. Zhou, Highly sensitive and dynamically stable strain sensors based on porous-designed Fe nanowires/multi-walled carbon nanotubes with stable bi-conducting networks, Science China Technological Sciences 65(12) (2022) 2990-2999.
[154] Y. Gao, X. Fang, J. Tan, T. Lu, L. Pan, F. Xuan, Highly sensitive strain sensors based on fragmentized carbon nanotube/polydimethylsiloxane composites, Nanotechnology 29(23) (2018) 235501.
[155] Y. Lu, M.C. Biswas, Z. Guo, J.-W. Jeon, E.K. Wujcik, Recent developments in bio-monitoring via advanced polymer nanocomposite-based wearable strain sensors, Biosensors and bioelectronics 123 (2019) 167-177.
[156] J. Lee, S. Pyo, D.S. Kwon, E. Jo, W. Kim, J. Kim, Ultrasensitive strain sensor based on separation of overlapped carbon nanotubes, Small 15(12) (2019) 1805120.
[157] A.B. Oskouyi, U. Sundararaj, P. Mertiny, Tunneling conductivity and

piezoresistivity of composites containing randomly dispersed conductive nano-platelets, Materials 7(4) (2014) 2501-2521.
[158] C. Li, E.T. Thostenson, T.-W. Chou, Dominant role of tunneling resistance in the electrical conductivity of carbon nanotube–based composites, Applied Physics Letters 91(22) (2007).
[159] D. Lee, H. Lee, Y. Jeong, Y. Ahn, G. Nam, Y. Lee, Highly Sensitive, Transparent, and Durable Pressure Sensors Based on Sea-Urchin Shaped Metal Nanoparticles, Advanced Materials (Deerfield Beach, Fla.) 28(42) (2016) 9364-9369.
[160] S. Xu, Z. Fan, C. Li, P. Wang, K.A. Sammed, L. Pan, Investigation of strain sensing mechanisms on ultra-thin carbon nanotube networks with different densities, Carbon 155 (2019) 421-431.
[161] W. Obitayo, T. Liu, A review: Carbon nanotube-based piezoresistive strain sensors, Journal of Sensors 2012(1) (2012) 652438.
[162] A. Duongthipthewa, H. Zhou, Q. Wang, L. Zhou, Non-additive polymer matrix coated rGO/MXene inks for embedding sensors in prepreg enhancing smart FRP composites, Composites Part B: Engineering 270 (2024) 111108.
[163] Q. Wang, M. Ma, A. Duongthipthewa, W. Zhang, Y. Lang, G. Luo, Y. Su, M. Liu, L. Zhou, Z. Su, "Totally-additive-manufacturing"-functionalized carbon fiber-reinforced polymer composites with an ultrasensitive self-sensing network, Composites Part A: Applied Science and Manufacturing 189 (2025) 108596.
[164] Q. Wang, Y. Tian, A. Duongthipthewa, J. Zhang, M. Liu, Z. Su, L. Zhou, An embedded non-intrusive graphene/epoxy broadband nanocomposite sensor co-cured with GFRP for in situ structural health monitoring, Composites Science and Technology 236 (2023) 109995.
[165] Y. Liao, F. Duan, H. Zhang, Y. Lu, Z. Zeng, M. Liu, H. Xu, C. Gao, L.-m. Zhou, H. Jin, Ultrafast response of spray-on nanocomposite piezoresistive sensors to broadband ultrasound, Carbon 143 (2019) 743-751.
[166] Y. Li, S. Guo, Z. Su, K. Ding, X.J. Loh, Lightweight and conformal acousto-ultrasonic sensing network for multi-scale structural health monitoring: A review, FlexMat 2(1) (2025) 4-29.
[167] Alamusi, N. Hu, H. Fukunaga, S. Atobe, Y. Liu, J. Li, Piezoresistive strain sensors made from carbon nanotubes based polymer nanocomposites, Sensors-Basel 11(11) (2011) 10691-10723.
[168] W. Xu, M.G. Allen, Deformable strain sensors based on patterned MWCNTs/polydimethylsiloxane composites, Journal of Polymer Science Part B: Polymer Physics 51(20) (2013) 1505-1512.
[169] J. Huang, S.-C. Her, X. Yang, M. Zhi, Synthesis and characterization of multi-walled carbon nanotube/graphene nanoplatelet hybrid film for flexible strain sensors, Nanomaterials 8(10) (2018) 786.
[170] N. Hu, Y. Karube, C. Yan, Z. Masuda, H. Fukunaga, Tunneling effect in a polymer/carbon nanotube nanocomposite strain sensor, Acta materialia 56(13) (2008) 2929-2936.
[171] P. Zhou, W. Cao, Y. Liao, K. Wang, X. Yang, J. Yang, Y. Su, L. Xu, L.-m. Zhou, Z. Zhang, Temperature effect on all-inkjet-printed nanocomposite piezoresistive

sensors for ultrasonics-based health monitoring, Composites science and technology 197 (2020) 108273.
[172] P. Zhou, Y. Liao, X. Yang, Y. Su, J. Yang, L. Xu, K. Wang, Z. Zeng, L.-m. Zhou, Z. Zhang, Thermally stable, adhesively strong graphene/polyimide films for inkjet printing ultrasound sensors, Carbon 184 (2021) 64-71.
[173] X. Li, T. Yang, Y. Yang, J. Zhu, L. Li, F.E. Alam, X. Li, K. Wang, H. Cheng, C.T. Lin, Large-area ultrathin graphene films by single-step marangoni self-assembly for highly sensitive strain sensing application, Advanced Functional Materials 26(9) (2016) 1322-1329.
[174] J. Chen, G. Zhu, F. Wang, Y. Xu, C. Wang, Y. Zhu, W. Jiang, Design of flexible strain sensor with both ultralow detection limit and wide sensing range via the multiple sensing mechanisms, Composites Science and Technology 213 (2021) 108932.
[175] B. Liang, Z. Lin, W. Chen, Z. He, J. Zhong, H. Zhu, Z. Tang, X. Gui, Ultra-stretchable and highly sensitive strain sensor based on gradient structure carbon nanotubes, Nanoscale 10(28) (2018) 13599-13606.
[176] Z. Zeng, M. Liu, H. Xu, Y. Liao, F. Duan, L.-m. Zhou, H. Jin, Z. Zhang, Z. Su, Ultra-broadband frequency responsive sensor based on lightweight and flexible carbon nanostructured polymeric nanocomposites, Carbon 121 (2017) 490-501.
[177] M. Dotoli, R. Rocca, M. Giuliano, G. Nicol, F. Parussa, M. Baricco, A.M. Ferrari, C. Nervi, M.F. Sgroi, A review of mechanical and chemical sensors for automotive Li-ion battery systems, Sensors-Basel 22(5) (2022) 1763.
[178] H. Popp, M. Koller, M. Jahn, A. Bergmann, Mechanical methods for state determination of Lithium-Ion secondary batteries: A review, Journal of Energy Storage 32 (2020) 101859.
[179] W. Wang, Y. Zhang, B. Xie, L. Huang, S. Dong, G. Xu, G. Cui, Deciphering advanced sensors for life and safety monitoring of lithium batteries, Advanced Energy Materials 14(24) (2024) 2304173.
[180] X. Cheng, M. Pecht, In situ stress measurement techniques on li-ion battery electrodes: A review, Energies 10(5) (2017) 591.
[181] A.S. Mussa, M. Klett, G. Lindbergh, R.W. Lindström, Effects of external pressure on the performance and ageing of single-layer lithium-ion pouch cells, Journal of Power Sources 385 (2018) 18-26.
[182] V. Müller, R.-G. Scurtu, M. Memm, M.A. Danzer, M. Wohlfahrt-Mehrens, Study of the influence of mechanical pressure on the performance and aging of Lithium-ion battery cells, Journal of Power Sources 440 (2019) 227148.
[183] W. Choi, Y. Seo, K. Yoo, T.J. Ko, J. Choi, Carbon nanotube-based strain sensor for excessive swelling detection of lithium-ion battery, 2019 20th international conference on solid-state sensors, actuators and microsystems & eurosensors XXXIII (TRANSDUCERS & EUROSENSORS XXXIII), IEEE, 2019, pp. 2356-2359.
[184] N. Sun, Q. Rong, J. Wu, L. Huang, S. Passerini, H. Li, H. Wang, J. Chen, Y. Huang, Z. Liu, Fully printable integrated multifunctional sensor arrays for intelligent lithium-ion batteries, Nature Communications 16(1) (2025) 7361.
[185] X. Zhao, Y. Zhou, A. Li, J. Xu, S. Karjagi, E. Hahm, L. Rulloda, J. Li, J. Hollister, P. Kavehpour, A self-filtering liquid acoustic sensor for voice recognition, Nature

Electronics 7(10) (2024) 924-932.
[186] X. Gao, L. Yuan, C. Xue, X. Zhang, X. Meng, X. Li, Bubbles-induced porous structure-based flexible piezoresistive sensors for speech recognition, ACS Applied Materials & Interfaces 16(7) (2024) 9532-9543.
[187] T.-S. Dinh Le, J. An, Y. Huang, Q. Vo, J. Boonruangkan, T. Tran, S.-W. Kim, G. Sun, Y.-J. Kim, Ultrasensitive anti-interference voice recognition by bio-inspired skin-attachable self-cleaning acoustic sensors, ACS nano 13(11) (2019) 13293-13303.
[188] Y. Dai, Y. Li, S. Xuan, Y. Dai, T. Xu, H. Yu, Triboelectric Nanogenerator-Based Flexible Acoustic Sensor for Speech Recognition, ACS Applied Materials & Interfaces 17(7) (2025) 11117-11125.
[189] X. Chen, D. Zhang, H. Luan, C. Yang, W. Yan, W. Liu, Flexible pressure sensors based on molybdenum disulfide/hydroxyethyl cellulose/polyurethane sponge for motion detection and speech recognition using machine learning, ACS Applied Materials & Interfaces 15(1) (2022) 2043-2053.
[190] J. Suo, X. Yang, Y.-O. Leung, J. Wang, M. Chen, Y. Liu, H. Sun, Z. Wang, X. Qiao, W.J. Li, Enabling natural human–computer interaction through ai-powered nanocomposite IoT throat vibration sensor, IEEE Internet of Things Journal 11(14) (2024) 24761-24774.
[191] S. Zhou, X. Gao, G. Park, X. Yang, B. Qi, M. Lin, H. Huang, Y. Bian, H. Hu, X. Chen, Transcranial volumetric imaging using a conformal ultrasound patch, Nature 629(8013) (2024) 810-818.
[192] Z. Lin, S. Duan, M. Liu, C. Dang, S. Qian, L. Zhang, H. Wang, W. Yan, M. Zhu, Insights into materials, physics, and applications in flexible and wearable acoustic sensing technology, Advanced Materials 36(9) (2024) 2306880.
[193] S.H. Lee, Y.-S. Kim, M.-K. Yeo, M. Mahmood, N. Zavanelli, C. Chung, J.Y. Heo, Y. Kim, S.-S. Jung, W.-H. Yeo, Fully portable continuous real-time auscultation with a soft wearable stethoscope designed for automated disease diagnosis, Science advances 8(21) (2022) eabo5867.
[194] H. Hu, X. Zhu, C. Wang, L. Zhang, X. Li, S. Lee, Z. Huang, R. Chen, Z. Chen, C. Wang, Stretchable ultrasonic transducer arrays for three-dimensional imaging on complex surfaces, Science advances 4(3) (2018) eaar3979.
[195] H. Hu, Y. Ma, X. Gao, D. Song, M. Li, H. Huang, X. Qian, R. Wu, K. Shi, H. Ding, Stretchable ultrasonic arrays for the three-dimensional mapping of the modulus of deep tissue, Nature Biomedical Engineering 7(10) (2023) 1321-1334.
[196] G.-Y. Gou, X.-S. Li, J.-M. Jian, H. Tian, F. Wu, J. Ren, X.-S. Geng, J.-D. Xu, Y.-C. Qiao, Z.-Y. Yan, Two-stage amplification of an ultrasensitive MXene-based intelligent artificial eardrum, Science advances 8(13) (2022) eabn2156.
[197] B.E. Richardson, R.W. Bastian, Clinical evaluation of vocal fold paralysis, Otolaryngologic Clinics of North America 37(1) (2004) 45-58.
[198] L.C. Wijesekera, P. Nigel Leigh, Amyotrophic lateral sclerosis, Orphanet journal of rare diseases 4(1) (2009) 3.
[199] Y. Wang, T. Yang, J. Lao, R. Zhang, Y. Zhang, M. Zhu, X. Li, X. Zang, K. Wang, W. Yu, Ultra-sensitive graphene strain sensor for sound signal acquisition and recognition, Nano Res 8(5) (2015) 1627-1636.

[200] L.-Q. Tao, H. Tian, Y. Liu, Z.-Y. Ju, Y. Pang, Y.-Q. Chen, D.-Y. Wang, X.-G. Tian, J.-C. Yan, N.-Q. Deng, An intelligent artificial throat with sound-sensing ability based on laser induced graphene, Nature communications 8(1) (2017) 14579.
[201] Y. Liu, C. Li, L. Yu, Z. Wu, S. Fan, R. Lv, Ultra-high sensitivity fiber optic microphone with corrugated graphene-oxide diaphragm for voice recognition, Nano Res 17(8) (2024) 7593-7602.
[202] Y.-Z. Zhang, K.H. Lee, D.H. Anjum, R. Sougrat, Q. Jiang, H. Kim, H.N. Alshareef, MXenes stretch hydrogel sensor performance to new limits, Science advances 4(6) (2018) eaat0098.
[203] Y. Ma, Y. Yue, H. Zhang, F. Cheng, W. Zhao, J. Rao, S. Luo, J. Wang, X. Jiang, Z. Liu, 3D synergistical MXene/reduced graphene oxide aerogel for a piezoresistive sensor, ACS nano 12(4) (2018) 3209-3216.
[204] Y. Cai, J. Shen, G. Ge, Y. Zhang, W. Jin, W. Huang, J. Shao, J. Yang, X. Dong, Stretchable Ti3C2T x MXene/carbon nanotube composite based strain sensor with ultrahigh sensitivity and tunable sensing range, ACS nano 12(1) (2018) 56-62.
[205] N. Shome, R.H. Laskar, D. Das, Reference free speech quality estimation for diverse data condition, International Journal of Speech Technology 22(3) (2019) 585-599.
[206] W. Ostachowicz, A. Güemes, New trends in structural health monitoring, Springer Science & Business Media2013.
[207] S. Alokita, V. Rahul, K. Jayakrishna, V. Kar, M. Rajesh, S. Thirumalini, M. Manikandan, Recent advances and trends in structural health monitoring, Structural health monitoring of biocomposites, fibre-reinforced composites and hybrid composites (2019) 53-73.
[208] N. Hu, Z. Masuda, C. Yan, G. Yamamoto, H. Fukunaga, T. Hashida, The electrical properties of polymer nanocomposites with carbon nanotube fillers, Nanotechnology 19(21) (2008) 215701.
[209] N. Hu, Y. Karube, M. Arai, T. Watanabe, C. Yan, Y. Li, Y. Liu, H. Fukunaga, Investigation on sensitivity of a polymer/carbon nanotube composite strain sensor, Carbon 48(3) (2010) 680-687.
[210] I. Kang, M.J. Schulz, J.H. Kim, V. Shanov, D. Shi, A carbon nanotube strain sensor for structural health monitoring, Smart materials and structures 15(3) (2006) 737.
[211] R. Guan, F. Zou, D. Li, W. Liu, C. Wu, Understanding the sensitivity of thin-film graphene/polymer nanocomposite strain sensors to ultrasonic waves: Analytical and experimental analysis, Composites Science and Technology 216 (2021) 109079.
[212] Y. Li, Y. Liao, Z. Su, Graphene-functionalized polymer composites for self-sensing of ultrasonic waves: An initiative towards “sensor-free” structural health monitoring, Composites Science and Technology 168 (2018) 203-213.
[213] Y. Zhao, X. Zheng, F. Qin, D. Estevez, Y. Luo, H. Wang, H. Peng, A self-sensing microwire/epoxy composite optimized by dual interfaces and periodical structural integrity, Composites Part B: Engineering 182 (2020) 107606.
[214] A. Mehmood, N. Mubarak, M. Khalid, P. Jagadish, R. Walvekar, E. Abdullah, Graphene/PVA buckypaper for strain sensing application, Scientific Reports 10(1) (2020) 20106.

[215] J. Koyanagi, S. Ogihara, H. Nakatani, T. Okabe, S. Yoneyama, Mechanical properties of fiber/matrix interface in polymer matrix composites, Advanced Composite Materials 23(5-6) (2014) 551-570.
[216] S. Ogihara, J. Koyanagi, Investigation of combined stress state failure criterion for glass fiber/epoxy interface by the cruciform specimen method, Composites Science and Technology 70(1) (2010) 143-150.
[217] Q. Wang, S. Chen, S. Zeng, P. Chen, Y. Xu, W. Nie, Y. Zhou, Tunable mechanical properties of glass fiber/epoxy composites by incorporating bioinspired montmorillonite–carbon nanotube/epoxy interface layer around the fiber, Composites Part B: Engineering 242 (2022) 110092.
[218] S. Zhandarov, E. Mäder, Characterization of fiber/matrix interface strength: applicability of different tests, approaches and parameters, Composites Science and Technology 65(1) (2005) 149-160.
[219] P.K. Datta, S. Biswas, Research advances on tension buckling behaviour of aerospace structures: a review, International Journal of Aeronautical and Space Sciences 12(1) (2011) 1-15.
[220] M.S. Kumar, K. Raghavendra, M.A. Venkataswamy, H.V. Ramachandra, Fractographic analysis of tensile failures of aerospace grade composites, Materials Research 15 (2012) 990-997.
[221] A. Kalhor, J. Dykas, K. Rodak, A. Grajcar, Materials and constructional design for electric vehicles: A review, Advances in Science and Technology. Research Journal 19(1) (2025) 178-196.
[222] J. Liu, Y. Kang, Research on Multi-Material Lightweight of Electric Vehicle Battery Box, SAE International Journal of Sustainable Transportation, Energy, Environment, & Policy 6(13-06-02-0013) (2025).
[223] A. Aufschläger, S. Kücher, L. Kraft, F. Spingler, P. Niehoff, A. Jossen, High precision measurement of reversible swelling and electrochemical performance of flexibly compressed 5 Ah NMC622/graphite lithium-ion pouch cells, Journal of Energy Storage 59 (2023) 106483.
[224] Y. Li, C. Wei, Y. Sheng, F. Jiao, K. Wu, Swelling force in lithium-ion power batteries, Industrial & Engineering Chemistry Research 59(27) (2020) 12313-12318.
[225] X. Feng, M. Ouyang, X. Liu, L. Lu, Y. Xia, X. He, Thermal runaway mechanism of lithium ion battery for electric vehicles: A review, Energy storage materials 10 (2018) 246-267.
[226] P. Mohtat, S. Lee, J.B. Siegel, A.G. Stefanopoulou, Reversible and irreversible expansion of lithium-ion batteries under a wide range of stress factors, Journal of The Electrochemical Society 168(10) (2021) 100520.
[227] W. Huang, Y. Ye, H. Chen, R.A. Vilá, A. Xiang, H. Wang, F. Liu, Z. Yu, J. Xu, Z. Zhang, Onboard early detection and mitigation of lithium plating in fast-charging batteries, Nature communications 13(1) (2022) 7091.
[228] A. Louli, L. Ellis, J. Dahn, Operando pressure measurements reveal solid electrolyte interphase growth to rank Li-ion cell performance, Joule 3(3) (2019) 745-761.
[229] S. Saxena, Y. Xing, D. Kwon, M. Pecht, Accelerated degradation model for C-

rate loading of lithium-ion batteries, International journal of electrical power & energy systems 107 (2019) 438-445.
[230] S. Nag-Chowdhury, H. Bellegou, I. Pillin, M. Castro, P. Longrais, J.F. Feller, Non-intrusive health monitoring of infused composites with embedded carbon quantum piezo-resistive sensors, Composites Science and Technology 123 (2016) 286-294.
[231] R. Moriche, M. Sanchez, A. Jimenez-Suarez, S.G. Prolongo, A. Urena, Strain monitoring mechanisms of sensors based on the addition of graphene nanoplatelets into an epoxy matrix, Composites Science and Technology 123 (2016) 65-70.
[232] C.S. Boland, Quantifying the Contributing Factors toward Signal Fatigue in Nanocomposite Strain Sensors, ACS Applied Polymer Materials 2(8) (2020) 3474-3480.
[233] R. Moriche, M. Sanchez, S.G. Prolongo, A. Jimenez-Suarez, A. Urena, Reversible phenomena and failure localization in self-monitoring GNP/epoxy nanocomposites, Composite Structures 136 (2016) 101-105.
[234] G.L. Goh, S. Agarwala, W.Y. Yeong, Aerosol-jet-printed preferentially aligned carbon nanotube twin-lines for printed electronics, Acs Appl Mater Inter 11(46) (2019) 43719-43730.
[235] S. Ramesh, C. Mahajan, S. Gerdes, A. Gaikwad, P. Rao, D.R. Cormier, I.V. Rivero, Numerical and experimental investigation of aerosol jet printing, Addit Manuf 59 (2022) 103090.
[236] G. Chen, Y. Gu, H. Tsang, D.R. Hines, S. Das, The Effect of Droplet Sizes on Overspray in Aerosol-Jet Printing, Adv Eng Mater 20(8) (2018).
[237] W. Bao, S. Meguid, Z. Zhu, G. Weng, Tunneling resistance and its effect on the electrical conductivity of carbon nanotube nanocomposites, Journal of Applied Physics 111(9) (2012).
[238] J.G. Simmons, Generalized formula for the electric tunnel effect between similar electrodes separated by a thin insulating film, Journal of applied physics 34(6) (1963) 1793-1803.
[239] D. Bohm, Quantum theory, Courier Corporation1989.
[240] J. Ji, P. Xia, X. Zhu, P. Liu, C. Wu, J. Tao, J. Yan, X. Liu, A simulation for the electrical conductivity of nanocomposites filled with carbon black based on the three-dimensional Monte Carlo method, Polymer Science, Series A 63 (2021) 196-207.
[241] G. Ambrosetti, C. Grimaldi, I. Balberg, T. Maeder, A. Danani, P. Ryser, Solution of the tunneling-percolation problem in the nanocomposite regime, Physical Review B—Condensed Matter and Materials Physics 81(15) (2010) 155434.
[242] R. Tamura, M. Tsukada, Electronic transport in carbon nanotube junctions, Solid state communications 101(8) (1997) 601-605.
[243] K. Tong, Q. Zhang, J. Chen, H. Wang, T. Wang, Research on throat speech signal detection based on a flexible graphene piezoresistive sensor, ACS Applied Electronic Materials 4(7) (2022) 3549-3559.
[244] H. Sun, X. Gao, L.Y. Guo, L.Q. Tao, Z.H. Guo, Y. Shao, T. Cui, Y. Yang, X. Pu, T.L. Ren, Graphene-based dual-function acoustic transducers for machine learning-assisted human–robot interfaces, InfoMat 5(2) (2023) e12385.
[245] Y. Okamoto, T.-V. Nguyen, H. Takahashi, Y. Takei, H. Okada, M. Ichiki, Highly

sensitive low-frequency-detectable acoustic sensor using a piezoresistive cantilever for health monitoring applications, Scientific reports 13(1) (2023) 6503.
[246] S. Lu, P. Zhang, Q. Yu, Q. Wu, Z. Gong, M. Liu, Insight into wave propagation in polyimide films and resistive grid sandwich structures towards a hybrid monitoring of hypervelocity impact, Ultrasonics (2024) 107471.
[247] Y. Yan, M. Wang, Y. Zhang, D. Wu, Y. Wang, X. Qing, Y. Wang, A low-velocity impact localization method for composite stiffened plate based on AIC and WPT, IEEE Sensors Journal (2024).
[248] Q.Q. Wang, Y. Tian, A. Duongthipthewa, J.Z. Zhang, M.L. Liu, Z.Q. Su, L.M. Zhou, An embedded non-intrusive graphene/epoxy broadband nanocomposite sensor co-cured with GFRP for in situ structural health monitoring, Compos Sci Technol 236 (2023).
[249] A. Duongthipthewa, H. Zhou, Q. Wang, L. Zhou, Non-additive polymer matrix coated rGO/MXene inks for embedding sensors in prepreg enhancing smart FRP composites, Composites Part B: Engineering (2023) 111108.
[250] D. Zhao, T. Liu, M. Zhang, R. Liang, B. Wang, Fabrication and characterization of aerosol-jet printed strain sensors for multifunctional composite structures, Smart materials and structures 21(11) (2012) 115008.